國立臺灣大學理學院物理學研究所

博士論文

Department of Physics

College of Science

National Taiwan University

Doctoral Dissertation

以太魯閣-4 電波天線陣列探尋極高能宇宙射線

Searching for Ultra High Energy Cosmic Ray Signal with Radio Antenna Array TAROGE-4

陳耀程

Yaocheng Chen

指導教授: 陳丕燊博士、南智祐 博士

Advisor: Pisin Chen, Ph.D., Jiwoo Nam, Ph.D.

中華民國 114 年 1 月

January, 2025

doi:10.6342/NTU202500216

國立臺灣大學博士學位論文

口試委員會審定書

PhD DISSERTATION ACCEPTANCE CERTIFICATE
NATIONAL TAIWAN UNIVERSITY

以太魯閣-4 電波天線陣列探尋極高能宇宙射線

Searching for Ultra High Energy Cosmic Ray Signal with

Radio Antenna Array TAROGE-4

本論文係 陳耀程 (姓名) D06222010（學號）在國立臺灣大學 物理學系 (系/所/學位學程)完成之博士學位論文，於民國 103 年 12 月 18 日承下列考試委員審查通過及口試及格，特此證明。

The undersigned, appointed by the Department / Institute of Physics

on 18 (date) December (month) 2024 (year) have examined a PhD dissertation entitled above presented by Chen Yaocheng (name) D06222010 (student ID) candidate and hereby certify that it is worthy of acceptance.

口試委員 Oral examination committee:

陳玉樂	莊智祚	黃明輝
（指導教授 Advisor）		
王子敬	劉宇哲	林宏輝

doi:10.6342/NTU202500216

Acknowledgements

First and foremost, I would like to express my deepest gratitude to my parents and my dearest wife, Yanan Wang, for their unconditional support and encouragement, which allowed me to fully dedicate myself to my research without any worries. I am also grateful to my sister, Peilin Chen, for her constant support and understanding, which have been a source of strength for me during challenging times.

I am profoundly grateful to my advisor, Prof. Pisin Chen, whose guidance has been invaluable throughout my academic journey. From him, I learned the importance of rigorous scholarship, the need to continuously challenge oneself, and the critical mindset required to refine both academic work and personal growth.

Thanks to Prof. Jiwoo Nam for his insightful guidance and thorough demonstration of how to conduct an experimental project in all aspects and details. His ability to transform ideas into actions promptly, while maintaining high standards of quality and fostering effective communication, has greatly influenced my approach to research and life.

I would also like to thank our lab members Prof. Tsung-Che, Dr. Shih-Hao, Dr. Jian-Jung, Dr. Shih-Ying, Yu-Hsin, Chung-Yun, Alex Leung, Alex Chen and Jacky, whose thoughtful feedback, advice, and encouragement during discussions have been invaluable over the past years. Their companionship made this journey not only more productive but

doi:10.6342/NTU202500216

also enjoyable. I am deeply grateful to everyone in the lab who has contributed to the TAROGE experiment, helping it grow from a nascent idea into a mature project. Your collaboration and dedication have been fundamental to its success.

Finally, I extend my heartfelt thanks to all the friends, collaborators, and mentors who have supported me throughout this journey. Your presence has made my doctoral research a rewarding and unforgettable experience.

doi:10.6342/NTU202500216

摘要

能量超過 10^{18} eV 的超高能宇宙射線的研究是當前物理學中的一個活躍研究領域，物理學家希望揭示這些高能粒子的來源及其加速機制。該領域的主要挑戰在於超高能宇宙射線的稀有性——每平方公里每年僅有約一次事件發生。因此，實現大規模探測面積和長時間觀測變得尤為重要。一種有效的超高能宇宙射線觀測方法是探測由其引發的廣延大氣簇射所發射的無線電脈衝。無線電輻射的主要機制是地磁效應。當廣延大氣簇射的帶電粒子在地球磁場中傳播時，洛倫茲力會使其偏轉，從而產生橫向電流。這個隨時間變化的橫向電流會發射出地磁輻射，其偏振方向與洛倫茲力方向一致。這種地磁輻射在幾兆赫到幾百兆赫的頻率範圍內具有相干性，以相對論性前向束射的形式在廣延大氣簇射前進方向發出，形成可以被探測到的短暫脈衝（持續時間為數納秒）。

除了超高能宇宙射線，廣延大氣簇射還可以由超高能微中子在地球表面以下通過帶電流相互作用產生的濤輕子衰變引發。超高能微中子可能通過宇宙射線與宇宙微波背景輻射的相互作用（即 GZK 效應）產生。已觀測到在 $4 \cdot 10^{17}$ eV 以上的超高能宇宙射線通量抑制，這支持了 GZK 效應的存在。與會被星際磁場偏轉的超高能宇宙射線不同，宇宙對超高能微中子幾乎是透明的，因此探測超高能微中子是間接發現超高能宇宙射線源的一個有效策略。

臺灣天文粒子地磁同步輻射電波觀測站（簡稱太魯閣，TAROGE）是一個位

doi:10.6342/NTU202500216

於臺灣東部沿海高山上的天線陣列，面向海洋，專為探測超高能宇宙射線引發的近地平線廣延大氣簇射和地表掠過的超高能濤微中子而設計。TAROGE 具有高有效觀測時間、低單位成本和良好擴展性等優點。從 2014 年到 2019 年，已有四個 TAROGE 站點在臺灣部署，每個站點的儀器都有所改進，以提高探測效率。最新部署的站點 TAROGE-4 配備了一種基於表面聲波濾波器的多頻帶觸發系統。該新型觸發系統能夠有效區分地磁同步輻射脈衝信號與郊區人類活動背景噪聲。

本文首先總結了 TAROGE-4 站點的概念和儀器設計。接著描述了用於校準接收系統響應以實現精確時間測量的分析步驟和差分響應反卷積方法。在降噪和響應反卷積的基礎上，本文實現了對廣延大氣簇射方向和入射電場的可靠重建。基於地磁輻射特性和環境噪聲，本文提出了事件選擇標準。包括觸發模擬以獲取探測效率。此外，還提出了蒙特卡羅探測模擬以驗證觸發和分析效率。最終目標是表徵探測事件的初級粒子並測量其通量。

關鍵字：微中子、宇宙射線、大氣簇射、天線陣列

doi:10.6342/NTU202500216

Abstract

The study of Ultra-High Energy Cosmic Rays (UHECRs) with energies greater than $10^{18}\ eV$ is an active research area where physicists hope to find the sources and the acceleration mechanisms of such high energy particles. The primary challenge in this field is their rarity, approximately one event per square kilometer annually, it becomes essential to implement expansive detection area and lengthy observational periods. One effective way to observe UHECRs is by detecting radio pulses emitted from Extensive Air Shower (EAS) induced by them. The main mechanism of radio emission is geomagnetic effect. When charged particles of EAS propagating in the earth's magnetic field, the Lorentz force will deflect them and thus induces a transverse current. The time-varying transverse current will emit geomagnetic radiation which polarization is aligning with the Lorentz force. This geomagnetic radiation is coherent at frequencies of a few to hundreds of MHz, generating short transient pulses (a few nanoseconds) relativistically beamed in the EAS forward direction at a detectable level.

doi:10.6342/NTU202500216

In addition to UHECRs, EAS can also be induced by the decay of tau leptons created through charged-current interaction of UHE (Ultra High Energy) neutrinos under the Earth's surface. UHE neutrinos could be produced through the interactions between cosmic rays and cosmic microwave background radiation (CMB), which is the so-called GZK effect. The suppression of the UHECR flux above $4 \cdot 10^{17}$ eV has been observed, which supports the existence of the GZK effect. Unlike UHECRs will be deflected by intergalactic magnetic fields, the universe is almost transparent to UHE neutrinos, thus detecting UHE neutrinos is a good indirect strategy to discover UHECR sources.

Taiwan Astroparticle Radiowave Observatory for Geosynchrotron Emissions (TAROGE) is an antenna array atop the high mountains on the eastern coast of Taiwan, pointing to the ocean. It is designed for the detection of near-horizon EAS induced by UHECRs and Earth-skimming UHE tau neutrinos with advantages in high effective live time, low unit cost and scalability. Four TAROGE stations in Taiwan have been deployed from 2014-2019, each station has improvements in instruments to increase detection efficiency. The latest deployed station TAROGE-4 has been equipped with a new trigger system by using Surface Acoustic Wave (SAW) filters based multi-bands coincidence technique. This new trigger system provides an effective discriminating power for impulsive geo-synchrotron signals against suburban anthropogenic backgrounds.

doi:10.6342/NTU202500216

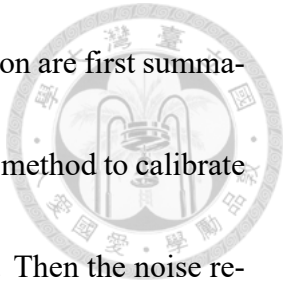

In this paper, The concept and the instrument of TAROGE-4 station are first summarized. Then the analysis steps and differnetial response deconvolution method to calibrate receiver response to get precise measurement of timing are described. Then the noise reduction and the deconvolution of the response are applied to obtain reliable reconstruction of EAS direction and incident electric field. Event selection criteria are proposed, based on the characteristics of geomagnetic emission and environmental noise. Trigger simulated are included to obtain the detedction efficiency. Monte-Carlo detection simulation are also proposed to verify trigger and analysis efficiency. The final goal is to characterize primary particles of detected events and measure their fluxes.

Keywords: neutrino, cosmic ray, air shower, antenna array

doi:10.6342/NTU202500216

doi:10.6342/NTU202500216

Contents

Page

Verification Letter from the Oral Examination Committee i

Acknowledgements iii

摘要 v

Abstract vii

Contents xi

List of Figures xvii

List of Tables xxix

Denotation xxxi

Chapter 1 ULTRA HIGH ENERGY PARTICLES AND THEIR DETECTIONS 1

1.1 Introduction 1

1.2 The Standard Model 3

1.2.1 The Components of The Standard Model 3

1.2.2 The Relevance of The Standard Model to UHE Particles 4

1.3 Cosmic Ray Overview 5

1.3.1 Cosmic Ray Acceleration 6

1.3.1.1 Fermi Acceleration 6

1.3.1.2 Magnetic Reconnection 7

doi:10.6342/NTU202500216

1.3.2 Cosmic Ray Spectrum 7
1.3.3 Cosmic Ray Composition 8
1.3.4 Potential Sources 11
1.3.5 UHECRs Detection 14
1.4 Neutrino Overview 16
1.4.1 The Need for the Neutrino 18
1.4.2 Neutrino Oscillation 20
1.4.3 Neutrino Interactions 21
1.4.4 Astrophysical Neutrinos 24
1.4.5 GZK Effect and Cosmogenic Neutrinos 25
1.4.6 Messengers of the UHE Universe 26
1.5 Radio Detection of Ultra High Energy Cosmic Particles 27
1.5.1 Particle Cascades 29
1.5.2 Electromagnetic Radiation from Moving Particles 32
1.5.2.1 Cherenkov Radiation 33
1.5.2.2 Askaryan Effect 34
1.5.2.3 Geomagnetic Emission 34
1.5.3 Radio Antenna Array on High Altitude 35
1.5.3.1 ANITA Anomalous Events 35
1.5.3.2 Radio Antenna Array on High Mountains 39
1.5.4 TAROGE Experiment 39
1.5.4.1 Detection Concept 39
1.5.4.2 TAROGE Stations in Taiwan and Antarctica 40

doi:10.6342/NTU202500216

Chapter 2 TAROGE-4 System **43**

2.1 Gneral Design 43

2.2 Antenna Design and Frequency Response 44

2.3 Front-End Electronics Module 47

2.3.1 Filters 48

2.3.2 Low Noise Amplifier Module 50

2.3.3 Responses 51

2.4 Data Acquisition System 51

2.4.1 Hardware 52

2.4.2 Program Algorithm 54

2.5 Power System 56

2.5.1 Photovoltaics Power Module 56

2.5.2 Monitor and Control 57

Chapter 3 TAROGE-4 Trigger System **59**

3.1 Suburban Environment 60

3.2 Trigger Banding 61

3.3 Design Logic 61

3.3.1 Single Band L1 Trigger 63

3.3.2 Multi-band L2 Trigger 64

3.3.3 Multi-antenna L3 Trigger 65

3.3.4 Global Trigger and Dynamic Threshold 66

3.4 Trigger Board Design 67

3.5 FPGA Programming 68

doi:10.6342/NTU202500216

Chapter 4 Event Angular Reconstruction and Calibration 73

4.1 Differential Responses Unfolding 74

4.1.1 Algorithm 74

4.1.2 Advantages 78

4.2 Interferometric Map 80

4.3 Drone-borne Pulser 82

4.3.1 Pulser Event Identification 84

4.3.2 Flight Summary 85

4.4 Angular Resolution 85

Chapter 5 UHECR Detection Simulation 91

5.1 Generation of Radio Signal 92

5.1.1 UHECR Air Shower Simulation 92

5.1.2 Radio Emission from Air Showers 94

5.1.3 Receiver Response Convolution 96

5.2 Trigger Simulation 97

5.2.1 Band Trigger Efficiency Modeling 98

5.2.2 Trigger System Simulation 98

5.2.3 Drone Pulser Verification 100

5.3 Monte Carlo Detection Simulation 101

5.3.1 Detection Efficiency for Individual Air Showers 101

5.3.2 Effective Area Calculation 103

5.4 Acceptance and Event Distribution 104

5.4.1 Potential Improvement 109

doi:10.6342/NTU202500216

Chapter 6 Cosmic Ray Searching **111**

6.1 Datasets 112

6.2 Selection Criteria 113

6.2.1 Dynamic Filtering and Cross-correlation 113

6.2.2 Software Trigger 114

6.2.3 Power Ratio Between Antennas 115

6.2.4 Reconstruction Reliability 116

6.2.5 Multi-pulses Anthropagenic Noise 117

6.2.6 Lightning Events 118

6.2.7 Temporal and Spatial Cluster 119

6.2.8 Template matching 120

6.3 Analysis Efficiency 121

6.4 Results 123

6.4.1 Background Estimates 123

6.4.2 CR Events 125

6.4.3 Zenithal Distributions 128

Chapter 7 Characteristics of TAROGE-4 UHECR Events **131**

7.1 Ocean Reflected Event 132

7.2 Double Pulses Events 134

7.2.1 Shower Maximum Estimation 136

7.3 Polarization Measurement 137

7.4 Energy Estimation 139

7.4.1 Energy Parametrization Techniques 141

doi:10.6342/NTU202500216

7.4.2 Fitting CR Events Spectrum 142
7.4.3 Observed Energy Distribution 145
7.5 Flux Measurement 147
Chapter 8 Conclusion and Discussion **149**
References **153**
Appendix A — Waveforms of CR candidates **171**

doi:10.6342/NTU202500216

List of Figures

1.1 Cosmic ray energy spectrum from various experiments. The left-hand side spans from 10^8 eV to 10^{21} eV, while the right-hand side focuses on 10^{17} eV to 10^{21} eV and is scaled with $E^{2.5}$ to highlight spectral features. Adapted from Ref. [74]. 8

1.2 Measurements of the depth of the shower maximum (X_{max}) from cosmic-ray-induced air showers recorded by various experiments. The left panel shows the mean $\langle X_{\text{max}} \rangle$, while the right panel displays the RMS $\sigma(\langle X_{\text{max}} \rangle)$. The lines represent the inferred cosmic ray composition, spanning from protons to iron, with different line styles corresponding to predictions from the hadronic interaction models Sibyll2.3d, EPOS-LHC, and QGSJet-II.04. Adapted from Ref. [122]. 10

doi:10.6342/NTU202500216

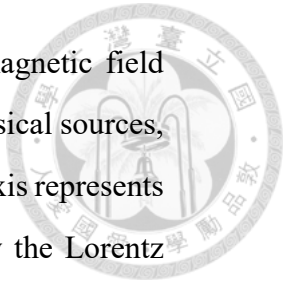

1.3 Left: Hillas diagram showing the relationship between magnetic field strength (B) and characteristic size (R) for various astrophysical sources, highlighting conditions for cosmic ray acceleration. The x-axis represents R, equal to the comoving size of the source multiplied by the Lorentz factor (Γ). Solid (dashed) lines indicate the thresholds for confining protons (red) and iron nuclei (blue) at 10^{20} eV, assuming outflow velocities of $\beta_{\rm sh} = 1$ (solid) and $\beta_{\rm sh} = 0.01$ (dashed). Only sources above these lines can confine such particles. Right: Characteristic source luminosity versus number density for steady sources and effective luminosity versus effective number density for transient sources, assuming a time spread of $\tau = 3 \times 10^5$ yr (corresponding to an extragalactic magnetic field strength of 1 nG). Stronger magnetic fields result in larger τ and higher effective number densities. Solid and dashed lines indicate the required energy budget for UHECRs ($L_{\rm CR}$) under different assumptions about their relationship with electromagnetic luminosity (L_γ). Adapted from Ref. [26]. . 14

1.4 Simplified sketch of an air shower caused by a cosmic ray interacting with the atmosphere and possible detection techniques. The shower consists of secondary particles propagating toward the ground, emitting Cherenkov and radio signals. Detection methods include ground-based particle detectors, radio antenna arrays, and fluorescence telescopes, which observe different components of the shower to reconstruct its properties. Adapted from Ref. [114]. 17

1.5 All-flavor neutrino spectrum from various sources, with solid curves representing neutrinos and dashed or dotted curves indicating antineutrinos. Contributions from cosmic, terrestrial, and astrophysical origins are highlighted. Adapted from Ref. [132]. 19

doi:10.6342/NTU202500216

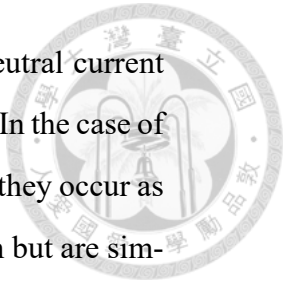

1.6 Feynman diagrams illustrating charged current (CC) and neutral current (NC) interactions between neutrinos and electrons or nuclei. In the case of ν_e, lepton scattering diagrams interfere, while for ν_μ and ν_τ, they occur as separate processes. Antineutrino ($\bar{\nu}$) diagrams are not shown but are similar, with $\bar{\nu}_e e^- \to W^-$ occurring via an s-channel, leading to the Glashow resonance. Neutrino-nucleon (νN) scattering involves underlying νq or $\nu \bar{q}$ sub-processes. Adapted from Ref. [121]. 23

1.7 The spectral flux of neutrinos, inferred from the eight-year IceCube upgoing track analysis (red fit) and the six-year HESE analysis (magenta fit), is compared to the flux of unresolved extragalactic gamma-ray sources (blue data) and ultra-high-energy cosmic rays (green data). The neutrino spectra are shown with the best-fit power-law (solid line) and the corresponding 1σ uncertainty range (shaded area). Adapted from Ref. [11]. 25

1.8 Neutrino-nucleon cross section measurements from various experiments (markers), with IceCube providing measurements at the highest energies. The black solid line and dashed band represent the model prediction. Colored bands illustrate the future prospects for IceCube-Gen2 in the UHE regime. Adapted from Ref. [8]. 27

1.9 Summary of the connections between various beyond Standard Model physics scenarios and neutrino observables. Adapted from Ref. [8]. . . . 28

doi:10.6342/NTU202500216

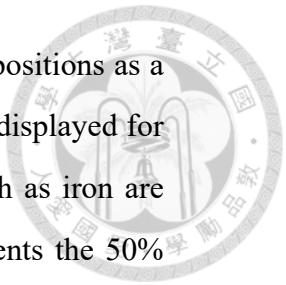

1.10 Left: The survival fraction of UHECRs with different compositions as a function of travel distance D (in Mpc). Hydrogen ions are displayed for energies $E > 40$, 60, and 100 EeV, while heavy ions such as iron are shown for $E > 60$ EeV. The solid horizontal line represents the 50% survival rate. Adapted from Ref. [88]. Right: The detection horizons of cosmic messengers, including protons, photons, and neutrinos, at various energy scales. The highest observed energies for protons and gamma rays are indicated in the plot. Protons at 10^{20} eV can only be observed within 100 Mpc due to attenuation caused by the GZK effect, excluding the red-shaded region. Gamma rays are limited as UHE messengers because of pair production with infrared and CMB photons, excluding them from the blue-shaded region. Neutrinos, in contrast, can traverse the entire universe up to 10^{25} eV, as the universe remains transparent to them. Adapted from Ref. [34]. 29

doi:10.6342/NTU202500216

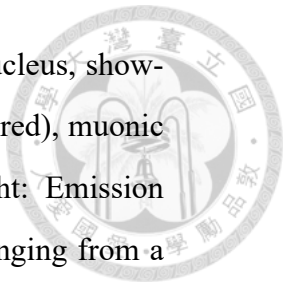

1.11 Left: Sketch of an EAS induced by a UHECR proton or nucleus, showing its key components: hadronic (black), electromagnetic (red), muonic (blue), and neutrino (green). Adapted from Ref. [9]. Right: Emission mechanisms relevant at typical observation frequencies (ranging from a few MHz to a few GHz) include geomagnetic and Askaryan emissions. Geomagnetic emission arises from the induction of a transverse current in the shower front, resulting in polarization aligned with the geomagnetic Lorentz force. In air, this mechanism is generally stronger than the Askaryan emission, which is caused by the time variation of the net charge excess in the shower front and is the dominant mechanism in dense media. For air showers, the observed radio emission is the coherent combination of both mechanisms. Depending on the local orientation of the electric-field vectors, the interference between the two can be constructive or destructive. The electric field's direction follows Lenz's law, which states that the induced field counteracts the cause of its origin. Consequently, the orientation of the electric field is constant for geomagnetic effects, while for the Askaryan effect, it reverses after the shower maximum as the charge excess begins to decrease. Adapted from Ref. [114]. 30

1.12 The detection concept of ANITA in the near-vertical Antarctic geomagnetic field. Geomagnetic signals from cosmic rays (CR) can be observed either directly or via reflection and include a small contribution from Askaryan radiation. Under-ice neutrino detection relies on Askaryan radiation, which dominates and originates from multiple particle showers caused by primary and secondary interactions. Additionally, geomagnetic signals may be produced by extensive air showers (EAS) initiated by τ-lepton decay following ν_τ charged-current (CC) interactions within the ice. Adapted from Ref [68]. 38

1.13 The detection concept of TAROGE. Adapted from Ref [101]. 40

1.14 TAROGE-4 station, LPDA antennas pointing horizontally to ocean. Adapted from Ref [40]. 42

doi:10.6342/NTU202500216

2.1 TAROGE-4 system architecture. Adapted from Ref. [101]. 45

2.2 TAROGE-4 antennas feature a Christmas-tree-shaped dual-polarization design, with H-pol and V-pol antennas collocated and crossing each other. This configuration enhances polarimetry capabilities and provides structural stability to withstand strong winds. 46

2.3 The measured realized gains (blue markers) and HFSS-simulated realized gains (orange curve) of the TAROGE-4 LPDA at boresight as a function of frequency. 47

2.4 FEE modules of TAROGE, including filter and LNA. 48

2.5 Gain (left) and phase shift (right) as functions of frequency for the TAROGE-4 FEE modules and cables, measured using a vector network analyzer. Two channels exhibit approximately 3 dB lower gain due to an additional combiner used to integrate a 100 MHz signal from the oscillator for synchronization between picoscopes. 51

2.6 Photo of TAROGE-4 DAQ system before installation. 54

2.7 DAQ program in block mode. 55

3.1 TAROGE-4 trigger system, including trigger boards and FPGA. 60

3.2 Trigger efficiency as a function of impulsive signal strength for different thresholds across all sub-bands in the TAROGE-4 trigger system. 62

3.3 The responses of the band-pass SAW filters used in TAROGE-4 trigger system. 62

3.4 General design logic of the TAROGE-4 trigger system. The L1 trigger is implemented in analog hardware, while the L2, L3, and system triggers are implemented digitally within the FPGA. Additionally, a command line (CMD) communication module is integrated into the FPGA, enabling communication with the DAQ computer, sending trigger signals to digitizers, and controlling the threshold settings of the trigger board DAC. 63

doi:10.6342/NTU202500216

3.5 Detailed implementation of the hierarchical trigger system shown in Fig. 3.4. Shift registers are utilized to record trigger information and evaluate coincidences. A delay module is employed to adjust for time delays caused by antenna geometry, while a pulse scaler accounts for delays introduced by signals arriving from different paths. Together, the delay module and pulse scaler module ensure that the system only detects signals originating from TAROGE-4's FoV, significantly reducing the impact of noise from the northern town. 64

3.6 Schematic of a single channel of the trigger board, illustrating the components and signal processing workflow for efficient triggering. Figure adapted from [39]. 67

3.7 Layout of the trigger board, showcasing the arrangement of components and design optimizations for minimizing interference and ensuring efficient signal processing. Figure adapted from [39]. 69

3.8 Produced trigger board, highlighting its compact yet sophisticated design, optimized for reliable and efficient signal processing in the TAROGE-4 trigger system. Figure adapted from [39]. 70

3.9 Simple testing of the trigger board. The red curve represents a cosmic ray-like impulse, the blue curve shows the output of the power detector, and the green curve represents the output of the comparator. The results confirm that the trigger board is functioning correctly. Figure adapted from [39]. 70

4.1 Drone-borne pulser system consisting of a high-power impulse generator, a programmable attenuator, a transmitting antenna, and a D-GPS module. This system enables precise calibration of TAROGE-4 by providing well-characterized signals across a wide frequency range and ensuring accurate positional tracking with centimeter-level precision. 84

4.2 Flight track (black curve) and the reconstructed direction of pulsers (red circles) for H-pol signals with elevation angles greater than 6°. 86

doi:10.6342/NTU202500216

4.3 The H-pol signals with elevation angles greater than 6° achieve an angular resolution of 0.27° in elevation (left) and 0.12° in azimuth (right). 86

4.4 Flight track (black curve) and the reconstructed direction of pulsers (red circles) for V-pol signals with elevation angles greater than 6°. 87

4.5 The V-pol signals with elevation angles greater than 6° achieve an angular resolution of 0.24° in elevation (left) and 0.10° in azimuth (right). 87

4.6 Flight track (black curve) and the reconstructed direction of pulsers (red circles) for H-pol signals with elevation angles within $\pm 6^\circ$. 87

4.7 The H-pol signals with elevation angles within $\pm 6^\circ$ achieve an angular resolution of 0.92° in elevation (left) and 0.24° in azimuth (right). 88

4.8 Flight track (black curve) and the reconstructed direction of pulsers (red circles) for V-pol signals with elevation angles within $\pm 6^\circ$. 88

4.9 The V-pol signals with elevation angles within $\pm 6^\circ$ achieve an angular resolution of 0.86° in elevation (left) and 0.23° in azimuth (right). 88

4.10 Angular resolution as a function of SNR for combined H-pol and V-pol signals within elevation angles of $\pm 6^\circ$. The angular resolution in both elevation (left) and azimuth (right) deteriorates as the SNR decreases. . . 89

4.11 Angular resolution as a function of elevation angle for combined H-pol and V-pol signals within elevation angles of $\pm 6^\circ$. The angular resolution in both elevation (left) and azimuth (right) deteriorates as the elevation angle decreases. 89

5.1 Left: 2D map illustrating the signal strength received at a 700 m altitude (by the TAROGE-4 station) for a $10^{18.5}$ eV proton-initiated air shower arriving from a zenith angle of 70°. Right: the waveforms of the electric fields sampled at points along the arm aligned with the $\vec{v} \times \vec{B}$ axis. . . . 95

5.2 Fourier transform of the waveforms shown in Fig. 5.1. The red line represents the best linear fit of the logarithmic amplitude spectrum within the frequency range of 180–350 MHz. 96

doi:10.6342/NTU202500216

5.3 Measured trigger efficiency compared to the results predicted by the trigger simulation model. The real pulser trigger efficiency closely matches the simulated efficiency as a function of SNR. 101

5.4 The dependence of acceptance on energy for pure proton (left) and iron (right) assumptions is shown. Generally, the acceptance increases with energy, and both assumptions exhibit similar trends in acceptance as a function of energy. 105

5.5 The dependence of acceptance on zenith angle for pure proton (left) and iron (right) assumptions is shown. At higher energies above approximately 2.5 EeV, the acceptance increases with zenith angle. Conversely, at lower energies, the acceptance decreases at larger zenith angles. Both assumptions demonstrate similar trends in acceptance as a function of zenith angle and energy. 105

5.6 The expected cosmic ray event rate distributions as functions of zenith angle for pure proton showers (left) and iron showers (right) across different energy ranges assuming 100% analysis efficiency. These distributions are computed assuming the Auger cosmic ray energy spectrum [130] and a one-year operation live time. 107

5.7 The expected cosmic ray event rate distributions as functions of zenith angle for pure proton showers (left) and iron showers (right) across different energy ranges with realistic analysis efficiency. These distributions are computed assuming the Auger cosmic ray energy spectrum [130] and a one-year operation live time. 107

5.8 The expected cosmic ray event rate distributions as functions of energy for pure proton showers (left) and iron showers (right) across different energy ranges assuming 100% analysis efficiency. These distributions are computed assuming the Auger cosmic ray energy spectrum [130] and a one-year operation live time. 108

doi:10.6342/NTU202500216

5.9 The expected cosmic ray event rate distributions as functions of energy for pure proton showers (left) and iron showers (right) across different energy ranges assuming 100% analysis efficiency. These distributions are computed assuming the Auger cosmic ray energy spectrum [130] and a one-year operation live time. 108

5.10 Concept diagram of an RFSoC design for real-time phased-array triggering. 110

6.1 The distribution of the number of frequency bins exceeding the software trigger threshold for RF-triggered, forced-triggered, and pulser data. . . . 115

6.2 Power imbalance between channels. The antenna located near the cliff (bottom panels) primarily receives the direct signal, while the other antennas primarily receive the diffracted signal. 116

6.3 Multi-pulses anthropogenic noise. 118

6.4 An angular distribution map showing impulses recorded over a single day with lightning activity. 119

6.5 Inefficiency caused by temporal and spatial isolation selection criteria across various angles within TAROGE-4 FoV. 120

6.6 ABCD method for background estimation in this CR search analysis. . . 124

6.7 Filtered, deconvolved, coherently summed waveforms of direct CR candidate event 00042337_4989 (left). And the corresponding angular distribution map for all RF-triggered events during that day with red circle indicates the CR candidate (right). 125

6.8 Observed zenith angle distributions of UHECR events, depicted by markers with error bars, are compared with the expected distributions derived from simulations based on the Auger cosmic ray spectrum. The red curve represents the expected distribution under the pure proton assumption, while the black curve corresponds to the pure iron assumption. 130

doi:10.6342/NTU202500216

7.1 Ocean-reflected events, in contrast to other direct cosmic ray (CR) candidates, exhibit a distinct phase inversion in both E_θ and E_ϕ waveforms. This phase inversion arises from the reflection of radio signals off the ocean surface, which alters the signal's polarity due to the boundary conditions at the air-water interface. 133

7.2 The magnitude (left) and phase (right) of the reflection coefficient as a function of the grazing angle for ocean reflection. The solid lines represent the more realistic case that accounts for the conductivity of seawater, while the dashed lines depict the simplified case where conductivity is not considered. 134

7.3 Double pulse CR candidate event 11897_3658. Similar to Fig. 7.4 135

7.4 Double pulse CR candidate event 16319_6029. Left: Coherent sum based on channel delays from the main pulse reconstruction direction. Right: Coherent sum based on channel delays from the second pulse reconstruction direction. 135

7.5 Double pulse CR candidate event 40661_5357. Similar to Fig. 7.4 135

7.6 Double pulse CR candidate event 43598_5124. Similar to Fig. 7.4 135

7.7 χ^2 fitting of the double pulse events: 11897_3658，16319_6029，40661_5357, 43598_5124, shown in order from left to right and top to bottom. 137

7.8 proton 139

7.9 Distribution of spectral slope versus energy-normalized intercept (to 1 EeV) for simulated proton showers coming from the same direction. The red line show the global linear fit. 142

7.10 Energy resolution for MC simulated events, showing an uncertainty of $\Delta(\log E) \approx 0.25$. 146

7.11 The energy distribution alongside detection simulations. The left panel represents the results under the pure proton assumption, while the right panel assumes pure iron composition. In both cases, the observed energy distributions align well with the simulations, indicating consistency between the observed events and theoretical models for cosmic ray detection. 146

doi:10.6342/NTU202500216

7.12 Comparison of the flux estimation results, with the left panel showing estimates under the assumption of pure proton composition and the right panel under pure iron composition. 148

A.1 Waveforms of 52 CR candidates, excluding one ocean-reflected event and four double-pulse events. 171

A.2 Waveforms of 52 CR candidates (continue), excluding one ocean-reflected event and four double-pulse events. 172

A.3 Waveforms of 52 CR candidates (continue), excluding one ocean-reflected event and four double-pulse events. 173

A.4 Waveforms of 52 CR candidates (continue), excluding one ocean-reflected event and four double-pulse events. 174

A.5 Waveforms of 52 CR candidates (continue), excluding one ocean-reflected event and four double-pulse events. 175

A.6 Waveforms of 52 CR candidates (continue), excluding one ocean-reflected event and four double-pulse events. 176

doi:10.6342/NTU202500216

List of Tables

6.1 Selection Criteria Efficiency for TAROGE-4 Dataset and MC Simulated CR Events 121

6.2 Summary of 57 CR candidates. 126

7.1 Fitting parameters and estimated energies of CR candidates. 143

doi:10.6342/NTU202500216

doi:10.6342/NTU202500216

Denotation

UHECR	UHECR (Ultra High Energy Cosmic Ray)
UHECN	UHECN (Ultra High Energy Cosmic Neutrino)
UHE	UHE (Ultra High Energy)
EAS	EAS (Extensive Air Shower)
AAE	AAE (ANITA Anomalous Event)
DAQ	DAQ (Data Acquisition)
RF	RF (Radio-Frequency)
RMS	RMS (Root Mean Square)
SNR	SNR (Signal-to-Noise Ratio)
TDOA	TDOA (Time Difference Of Arrival)
CMB	CMB (Cosmic Microwave Background)
SM	SM (Standard Model)

doi:10.6342/NTU202500216

CC	CC (Charged-Current)
NC	NC (Neutral-Current)
AGN	AGN (Active Galactic Nuclei)
GRB	GRB(Gamma Ray Burst)
TDE	TDE(Tidal Disruption Event)
UV	UV(Ultraviolet)
VHEGR	VHEGR(Very High Energy Gamma Ray)
GZK	GZK(Greisen-Zatsepin-Kuzmin effect)
LNA	LNA(Low-Noise Amplifier)
FEE	FEE(Front-End Electronics)
EMI	EMI(Electromagnetic Interference)
RFI	RFI(Radio Frequency Interference)

doi:10.6342/NTU202500216

Chapter 1 ULTRA HIGH ENERGY PARTICLES AND THEIR DETECTIONS

1.1 Introduction

Extreme environments in the universe can accelerate particles to incredibly high energies, far exceeding the energy levels achievable in terrestrial laboratories.[88]. Ultra-high-energy cosmic rays (UHECRs) and ultra-high-energy cosmic neutrinos (UHECNs) are among the highest-energy particles ever observed, with energies exceeding 10^{18} eV[89, 100]. These extraordinary particles provide a unique and valuable perspective for studying the mechanisms of cosmic accelerators, the large-scale structure of the universe, and potential interactions beyond the Standard Model (BSM).[17]. However, despite more than a century of research, their origins and acceleration mechanisms remain some of the most persistent mysteries in particle astrophysics.[41, 64, 79].

UHECRs with energy larger than $4 \cdot 10^{19}$ eV, predominantly protons and nuclei, interact with the cosmic microwave background (CMB) during their intergalactic journey, losing energy and generating secondary particles such as UHE neutrinos[28, 64]. These

doi:10.6342/NTU202500216

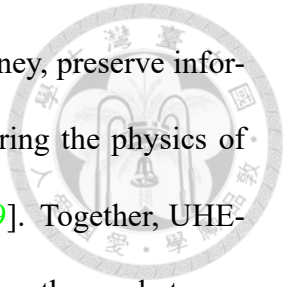

neutrinos, unimpeded by magnetic fields and matter during their journey, preserve information about their sources, making them invaluable tools for exploring the physics of ultra-UHECRs and the extreme environments that produce them.[139]. Together, UHECRs and UHECNs serve as complementary cosmic messengers, bridging the gap between astrophysical and particle physics[115, 128].

This dissertation focuses on the detection of UHECRs and UHECNs using radio techniques by the 4^{th} station of Taiwan Astroparticle Radiowave Observatory for Geosynchrotron Emissions (TAROGE), which leverages the coherent radio-frequency (RF) emissions from particle cascades initiated by these energetic particles[40]. By addressing the following key questions, this research aims to advance the understanding of UHE particles and their role in the universe:

- What are UHECRs and UHECNs? Their characteristics, origins, and significance in astrophysics and particle physics.
- How are UHECNs related to UHECRs? Their role in unraveling the mystery of UHECR sources and their potential as the final piece of multi-messenger astronomy.
- What makes radio detection effective? The principles behind RF emissions and their application in detecting both UHECRs and UHECNs.
- What are the current and future experimental efforts? A review of prominent experiments and their implications for UHE particle research.
- What do the anomalous upward-going events observed in the Antarctic Impulsive Transient Antenna (ANITA) experiment reveal[68–70]? Their potential implications for physics beyond the Standard Model (SM).

doi:10.6342/NTU202500216

1.2 The Standard Model

The SM of particle physics is one of the most successful theoretical frameworks in science, providing a comprehensive description of the fundamental particles and the laws governing their interactions in the universe. It unifies three of the four known fundamental forces (electromagnetic, weak, and strong interactions) into a single framework of quantum field theory.[1]. As the fourth fundamental force, gravity is excluded from the Standard Model SM of particle physics due to unresolved challenges in reconciling it with quantum mechanics at the quantum scale.[49]. While the SM has been remarkably successful in explaining numerous physical phenomena, it remains incomplete, especially at the extreme energy scales associated with UHECRs and UHECNs[31]. These particles provide a unique testing ground for exploring the limitations of the SM and the potential discovery of physics beyond it[60].

1.2.1 The Components of The Standard Model

The SM categorizes all known particles into two classes: fermions and bosons. Fermions, the building blocks of matter, obey Fermi-Dirac statistics, while bosons, the mediators of forces, follow Bose-Einstein statistics[73].

Fermions includes quarks and leptons. Quarks are the constituents of hadrons, such as protons and neutrons. They come in six flavors (up, down, charm, strange, top, and bottom) and carry both electric charge and color charge, the latter making them participants in the strong interaction. Due to confinement, quarks are never observed as free particles but always exist within composite structures like baryons (three quarks) or mesons (quark-

doi:10.6342/NTU202500216

antiquark pairs). Leptons include the electron (e), muon (μ), and tau (τ), each with a corresponding neutrino (electron neutrino ν_e, muon neutrino ν_μ, and tau neutrino ν_τ)[125]. Leptons, unlike quarks, are unaffected by the strong interaction. Neutrinos, in particular, are highly elusive, interacting solely via the weak force. This makes them challenging to detect but perfectly suited for studying extreme astrophysical environments[57].

Bosons include photon, W and Z bosons, gluons, and Higgs boson. Photons mediate electromagnetic interactions between particles with electric charge, while the W and Z bosons are responsible for weak interactions, including β decay and neutrino interactions[125]. Gluons mediate the strong interaction, binding quarks together within hadrons, while the Higgs boson provides mass to elementary particles through the Higgs mechanism which was confirmed experimentally by the discovery of the Higgs boson at CERN in 2012[3, 36].

These particles interact through gauge symmetries described by the mathematical groups $U(1)$, $SU(2)$, and $SU(3)$, corresponding to the electromagnetic, weak, and strong forces, respectively[73]. The symmetry breaking via the Higgs mechanism gives rise to the observed mass hierarchy among particles[78].

1.2.2 The Relevance of The Standard Model to UHE Particles

The SM serves as a robust framework for understanding particle interactions at accessible energy scales, but the extreme energies of UHECRs and UHECNs stretch its boundaries, presenting opportunities to test its limits and explore new physics[100]. Several phenomena associated with these particles challenge the SM and provide avenues for investigation.

doi:10.6342/NTU202500216

Neutrino oscillations, a phenomenon where neutrinos change their flavor during propagation, indicate that neutrinos have mass—something not accounted for by the original SM[31]. This discovery necessitates theoretical extensions, such as the inclusion of right-handed neutrinos or mechanisms like the seesaw model, which can explain the small observed masses of neutrinos[32, 55]. At ultra-high energies, neutrinos interact with matter via charged-current (CC) and neutral-current (NC) processes mediated by W and Z bosons[42, 94]. Understanding these interactions at energies above 10^{18} eV is critical for probing the weak interaction at extreme scales, as well as for determining neutrino propagation and detection probabilities[19, 65, 95].

The detection of UHE particles serves as a natural laboratory for exploring physics at energy scales far beyond the reach of terrestrial accelerators[35, 66]. Observations at these scales have profound implications, particularly for the unification of fundamental forces, as they may shed light on the relationship between electromagnetic, weak, and strong interactions[126, 133]. Moreover, the interactions of UHECNs provide a unique opportunity to measure weak interaction cross-sections at unparalleled energies, offering valuable constraints on theoretical models and advancing our understanding of particle physics[126, 127]. Additionally, anomalous upward-going events observed by ANITA, hint at potential new physical processes or particles beyond the SM, underscoring the transformative potential of UHE particle studies[68–70].

1.3 Cosmic Ray Overview

Cosmic rays are high-energy particles that originate from outer space and constantly bombard the Earth. Composed primarily of protons, atomic nuclei, and electrons, they

doi:10.6342/NTU202500216

span an immense energy range, from a few giga-electronvolts (GeV) to over $10^{20} eV$. The study of cosmic rays provides valuable understanding of the most energetic processes in the universe, the composition and distribution of interstellar matter, and the mechanisms that facilitate particle acceleration in extreme astrophysical conditions[52].

1.3.1 Cosmic Ray Acceleration

The acceleration of cosmic rays to ultra-high energies is a key question in astrophysics. Particles gain energy in astrophysical environments through repeated interactions with electromagnetic fields or shocks[29, 38]. Two prominent mechanisms for cosmic ray acceleration are Fermi acceleration and magnetic reconnection[88].

1.3.1.1 Fermi Acceleration

Fermi acceleration, named after physicist Enrico Fermi, is a stochastic process in which charged particles gain energy through repeated interactions with moving magnetic fields. This mechanism is categorized into two types[24]:

- First-Order Fermi Acceleration: This occurs in shock fronts, where particles are accelerated as they repeatedly cross the boundary between upstream and downstream regions of the shock. The particle's energy increases proportionally to the velocity of the shock front, making this process highly efficient in accelerating particles to UHE energies. Supernova remnants and relativistic jets in active galactic nuclei (AGN) are prime sites for first-order Fermi acceleration[48].

- Second-Order Fermi Acceleration: This occurs in turbulent magnetic fields, where particles gain energy through random collisions with moving magnetized plasma

doi:10.6342/NTU202500216

clouds. The energy gain is less efficient than in the first-order process, as it depends on the relative motion of the magnetic structures rather than a directional shock[90].

1.3.1.2 Magnetic Reconnection

Another mechanism capable of accelerating particles to high energies is magnetic reconnection, which occurs when magnetic field lines in a plasma break and reconnect, releasing immense energy. This process is highly efficient in strongly magnetized regions, such as the magnetospheres of pulsars or the coronae surrounding black holes. The rapid transformation of magnetic energy into kinetic energy accelerates charged particles to relativistic speeds, playing a crucial role in the generation of UHECRs[107].

1.3.2 Cosmic Ray Spectrum

The energy spectrum of cosmic rays spans more than 12 orders of magnitude and follows a piecewise power-law distribution, as depicted in Fig. 1.1. Several features in the spectrum indicate (γ) transitions in the origin and propagation mechanisms of cosmic rays[41, 58, 92]:

- The "Knee" ($\sim 10^{15.5}\ eV$): A steepening of the spectrum occurs, with γ increasing from approximately 2.7 to 3. This is thought to signify the transition from galactic to extragalactic sources or the energy limit of galactic accelerators.
- The "Second Knee" ($\sim 10^{17}\ eV$): A further steepening of the spectrum is observed at this energy, with γ increasing again. The second knee likely signifies the final energy cutoff for galactic cosmic rays, where even heavy nuclei can no longer be confined and accelerated by galactic sources. Beyond this energy, the extragalactic

doi:10.6342/NTU202500216

contribution becomes increasingly significant. This feature represents the boundary between the highest-energy particles of galactic origin and the onset of extragalactic dominance.

- The "Ankle" ($\sim 10^{18.5}\ eV$): A hardening of the spectrum, with γ decreasing to about 2.6, is observed. This is commonly interpreted as the dominance of extragalactic cosmic rays and a reduction in energy losses from interactions with the interstellar medium.

- The Greisen-Zatsepin-Kuzmin (GZK) Suppression ($> 10^{19.7}\ eV$): At the highest energies, the spectrum steepens due to energy losses from interactions with the cosmic microwave background (CMB), primarily through photopion production.

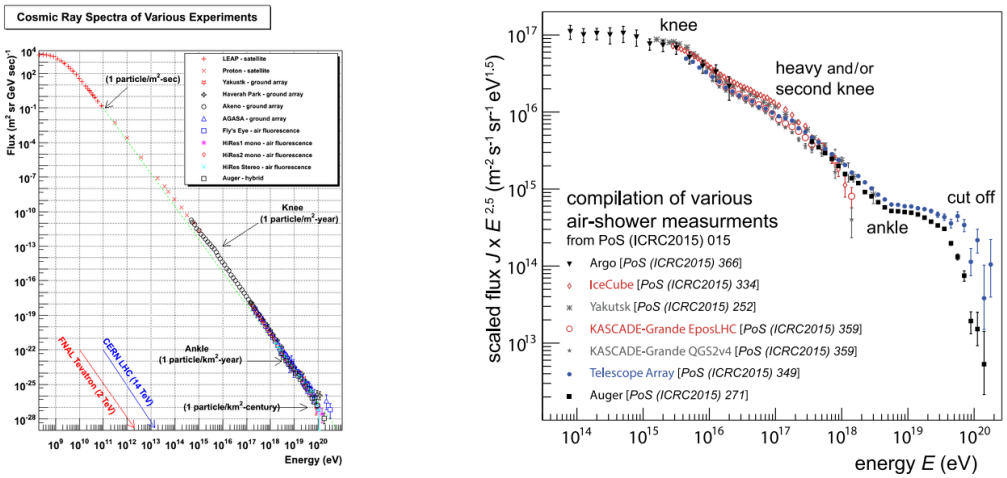

Figure 1.1: Cosmic ray energy spectrum from various experiments. The left-hand side spans from 10^8 eV to 10^{21} eV, while the right-hand side focuses on 10^{17} eV to 10^{21} eV and is scaled with $E^{2.5}$ to highlight spectral features. Adapted from Ref. [74].

1.3.3 Cosmic Ray Composition

The composition of cosmic rays provides essential insights into their origins, acceleration mechanisms, and interactions during propagation. These particles, predominantly

doi:10.6342/NTU202500216

charged, include protons, atomic nuclei, and a small fraction of electrons. Their composition evolves with energy as shown in Fig. 1.2, reflecting transitions between galactic and extragalactic sources and the physical processes that govern their journey through space[122, 122, 138].

At lower energies, below the "knee" ($\sim 10^{15.5}\ eV$), cosmic rays are predominantly protons ($\sim 90\%$), with helium nuclei ($\sim 9\%$) and a minor fraction of heavier nuclei ($\sim 1\%$). This composition reflects their origin in galactic sources such as supernova remnants (SNRs), where elements synthesized in stellar nucleosynthesis dominate the accelerated population. Electrons contribute a small fraction, yet they are crucial in understanding synchrotron and inverse Compton emissions in astrophysical processes.

As the energy surpasses the knee and approaches the "second knee" ($\sim 10^{17}\ eV$), a transition to heavier nuclei becomes evident. This transition is attributed to the energy-dependent cutoff of galactic accelerators. The maximum energy of cosmic rays accelerated in such environments depends on the particle's rigidity ($R = E/Z$), where Z is the charge of the nucleus. Consequently, lighter particles, such as protons, reach their maximum energy first, leaving a population increasingly dominated by heavier nuclei like iron. This progression indicates that galactic sources are nearing their acceleration limits for cosmic rays.

At energies near the "ankle" ($\sim 10^{18.5}\ eV$), the composition shifts back toward lighter elements, predominantly protons and helium nuclei. This energy range signifies the shift from galactic to extragalactic sources, where the contribution from astrophysical accelerators such as active galactic nuclei (AGN) or gamma-ray bursts (GRBs) becomes dominant. These extragalactic sources are believed to preferentially accelerate protons, given their

doi:10.6342/NTU202500216

abundance and efficient acceleration in large-scale magnetic fields.

Above the ankle, at ultra-high energies ($> 10^{19.7}\ eV$), the composition exhibits a trend back toward heavier nuclei. This could indicate the presence of UHECR sources with significant metallicity or the effect of photodisintegration during propagation through intergalactic space. Photodisintegration occurs when high-energy nuclei interact with photons from the CMB or extragalactic background light (EBL), causing them to break into lighter nuclei and protons. The observed composition at these energies reflects the balance between the primary acceleration environment, propagation effects, and detection limits.

This energy-dependent evolution of cosmic ray composition highlights the complexity of cosmic ray physics, where factors such as source properties, acceleration mechanisms, and propagation effects collectively shape the observed spectrum. It also underscores the importance of multi-observational techniques to disentangle these contributions and refine our understanding of cosmic ray origins.

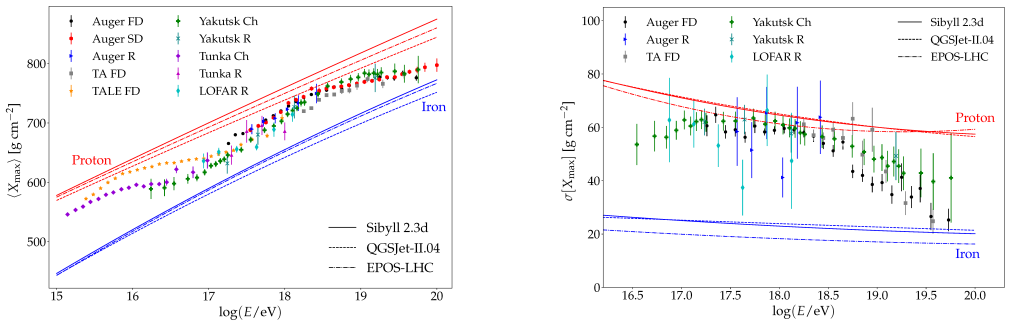

Figure 1.2: Measurements of the depth of the shower maximum ($X_{\max}$) from cosmic-ray-induced air showers recorded by various experiments. The left panel shows the mean $\langle X_{\max} \rangle$, while the right panel displays the RMS $\sigma(\langle X_{\max} \rangle)$. The lines represent the inferred cosmic ray composition, spanning from protons to iron, with different line styles corresponding to predictions from the hadronic interaction models Sibyll2.3d, EPOS-LHC, and QGSJet-II.04. Adapted from Ref. [122].

doi:10.6342/NTU202500216

1.3.4 Potential Sources

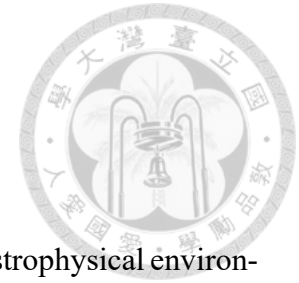

The acceleration of cosmic rays to ultra-high demands requires astrophysical environments with exceptional energy outputs and strong magnetic field configurations. These environments must confine charged particles long enough to accelerate them to the observed energies before they escape[17]. Directly pinpointing UHECR sources is challenging due to deflections caused by galactic and intergalactic magnetic fields[21]. However, potential sources can be inferred based on two critical criteria: their capability to achieve the necessary maximum acceleration energy and their ability to sustain the observed energy flux of UHECRs.

One framework for evaluating potential UHECR sources is the Hillas criterion, which sets a fundamental requirement for acceleration[79]. According to this criterion, the gyroradius of a particle must be smaller than the characteristic size of the source[106]. The gyroradius, also known as the Larmor radius, is given by:

$$R_g = \frac{E}{Z_e B}, \tag{1.1}$$

where E is the particle energy, Z is the charge number, e is the elementary charge, and B is the magnetic field strength. For a source to confine particles, its size L must satisfy:

$$R_g \leq L. \tag{1.2}$$

This condition can also be expressed in terms of the maximum achievable energy:

$$E_{max} \leq \eta^{-1} \beta Z_e B R \Gamma. \tag{1.3}$$

doi:10.6342/NTU202500216

Here, η is the acceleration efficiency, β is the velocity of the accelerated particles relative to the speed of light, R is the characteristic size of the source, and Γ is the Lorentz factor of bulk motion[29]. This equation shows that astrophysical sources with larger sizes, stronger magnetic fields, and higher acceleration efficiencies are more likely to accelerate particles to UHECR energies.

The Hillas plot, which compares magnetic field strength and characteristic size for various astrophysical objects, highlights several promising candidates as shown in left hand side of Figure 1.3. These include steady sources, such as AGNs and starburst galaxies, and transient events, such as GRBs and tidal disruption events (TDEs)[26]. AGNs, powered by accretion onto supermassive black holes, produce relativistic jets with high Lorentz factors ($\Gamma \sim 10$) and strong magnetic fields, making them ideal candidates for UHECR acceleration[59]. Similarly, GRBs, which are the most luminous explosions in the universe, involve highly energetic outflows with Lorentz factors as high as $\Gamma \sim 10$, providing an efficient environment for particle acceleration[137].

In addition to satisfying the Hillas criterion, the energy budget of UHECR sources provides a critical constraint on their plausibility, as potential sources must deliver sufficient luminosity to account for the observed UHECR flux at Earth[26]. Both steady and transient astrophysical objects are considered viable candidates, but their energy contributions differ significantly as shown in right hand side of Fig. 1.3. Steady sources, such as AGNs and starburst galaxies, rely on sustained cosmic ray production over long timescales[106]. In contrast, transient events like GRBs and TDEs compensate for their short durations with intense bursts of energy[30]. The relationship between the effective luminosity and the number density of these sources, factoring in magnetic deflection that spreads UHECR arrival times over $\sim 3 \times 10^5$ years, highlights the viability of various

doi:10.6342/NTU202500216

candidates[118]. AGNs, powered by supermassive black holes, and GRBs, with their relativistic jets and extreme Lorentz factors ($\Gamma \sim 10$), emerge as particularly promising UHECR accelerators, satisfying both the Hillas criterion and energy budget requirements. Energy-density plots further illustrate this balance, with AGNs and starburst galaxies dominating the steady-source regime, while GRBs and TDEs populate the transient regime, providing a comprehensive framework for understanding the origins of UHECRs.

SNRs, long considered primary accelerators of galactic cosmic rays, can accelerate particles up to the "knee" in the cosmic ray spectrum ($\sim 10^{15.5}\ eV$). However, their ability to contribute to UHECRs is limited by their size and magnetic field strength. Above the knee, heavier nuclei are favored due to their higher rigidity, but SNRs likely cannot account for cosmic rays beyond the "second knee" ($\sim 10^{17}\ eV$), which marks the limit of galactic accelerators[76].

Galaxy clusters, the largest gravitationally bound structures in the universe, are another candidate for UHECR sources. Large-scale shocks and turbulence in these clusters provide a mechanism for particle acceleration over long timescales. While their lower magnetic field strengths limit the maximum achievable energy, their immense sizes compensate, enabling particle confinement and acceleration to ultra-high energies[47].

Despite these promising candidates, distinguishing between potential UHECR sources remains challenging due to the lack of directional information from cosmic rays, which are deflected by magnetic fields. However, multi-messenger observations—incorporating neutrinos and gamma rays—offer a way to address this degeneracy. High-energy neutrinos, produced through hadronic interactions at cosmic accelerators, travel straight from their sources, providing unambiguous directional information[120]. Observations of cor-

doi:10.6342/NTU202500216

related neutrino and UHECR events, such as those detected by IceCube in association with AGN flares, strengthen the case for specific astrophysical objects as UHECR sources[43].

Ultimately, the study of UHECR sources requires not only larger and more sensitive cosmic ray detectors for improved statistics but also complementary observations across multiple messengers. The next generation of UHECR and neutrino observatories will play a pivotal role in unraveling the mysteries of UHECR origins, shedding light on the most extreme phenomena in the universe.

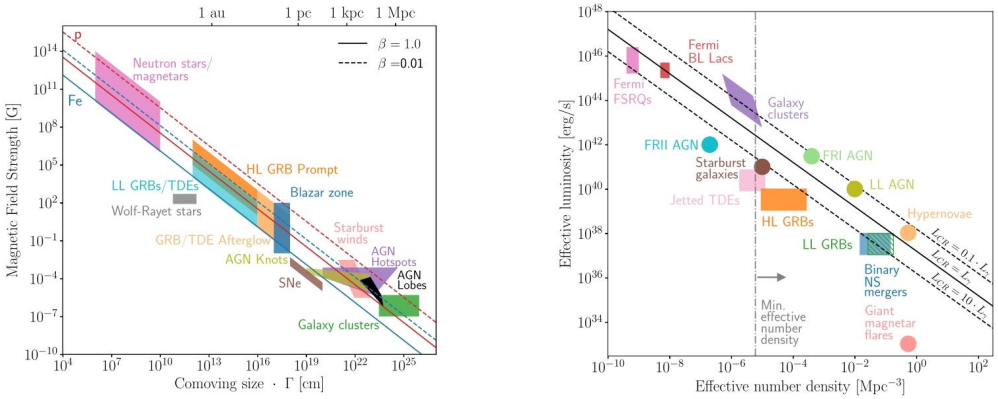

Figure 1.3: Left: Hillas diagram showing the relationship between magnetic field strength (B) and characteristic size (R) for various astrophysical sources, highlighting conditions for cosmic ray acceleration. The x-axis represents R, equal to the comoving size of the source multiplied by the Lorentz factor (Γ). Solid (dashed) lines indicate the thresholds for confining protons (red) and iron nuclei (blue) at 10^{20} eV, assuming outflow velocities of $\beta_{\rm sh} = 1$ (solid) and $\beta_{\rm sh} = 0.01$ (dashed). Only sources above these lines can confine such particles. Right: Characteristic source luminosity versus number density for steady sources and effective luminosity versus effective number density for transient sources, assuming a time spread of $\tau = 3\times10^5$ yr (corresponding to an extragalactic magnetic field strength of 1 nG). Stronger magnetic fields result in larger τ and higher effective number densities. Solid and dashed lines indicate the required energy budget for UHECRs ($L_{\rm CR}$) under different assumptions about their relationship with electromagnetic luminosity (L_γ). Adapted from Ref. [26].

1.3.5 UHECRs Detection

UHECRs are detected indirectly through extensive air showers (EAS) that occur when these cosmic rays interact with the Earth's atmosphere. These showers consist of

doi:10.6342/NTU202500216

billions of secondary particles, photons, and electromagnetic radiation, resulting from a cascade of interactions initiated by the primary cosmic ray. By studying these cascades, researchers can infer key characteristics of the primary cosmic ray, such as its energy, composition, and arrival direction. Various detection techniques have been developed, as shown in Fig. 1.4, each offering complementary insights into the EAS and the nature of cosmic rays[114].

Surface particle detectors measure secondary particles from EAS at ground level. These detectors, deployed in large arrays, provide a sampling of the shower front as it reaches the Earth. For instance, the Pierre Auger Observatory, located in Argentina, is the largest cosmic ray detector in the world, covering an area of 3,000 km². Its array of water-Cherenkov detectors measures the arrival times and densities of particles, enabling reconstruction of the primary particle's energy and arrival direction. By comparing the lateral distribution of secondary particles across the array, surface detectors also provide clues about the composition of the primary cosmic ray. For example, showers initiated by heavier nuclei tend to produce denser and more compact particle distributions compared to those initiated by protons[45, 46].

Optical fluorescence telescopes detect ultraviolet (UV) fluorescence light emitted by nitrogen molecules in the atmosphere, which are excited by the passage of charged particles in the EAS. These telescopes observe the development of the shower in the atmosphere, capturing the longitudinal profile of the cascade as it propagates toward the ground. The Telescope Array in Utah employs fluorescence detectors to monitor the faint UV light emitted by EAS during clear, moonless nights. This technique provides direct measurements of the depth of the shower maximum (X_{max}), a critical parameter for determining the composition of the primary cosmic ray[45, 46]. Protons tend to produce showers with

doi:10.6342/NTU202500216

deeper X_{max}, while heavier nuclei interact earlier, leading to shallower showers. By combining fluorescence data with surface detector measurements, hybrid systems like those at the Pierre Auger Observatory achieve high-precision energy and composition analyses[7].

Radio detection utilizes the coherent RF emissions generated during EAS, primarily through two mechanisms. When charged particles in extensive air showers interact with Earth's magnetic field, they generate geomagnetic radiation, which results from a transverse current producing polarized radio waves. In dense media like ice or salt, the Askaryan effect takes place as particle showers develop a charge imbalance, producing coherent radio waves at the Cherenkov angle. These mechanisms form the basis for modern radio detection techniques, enabling efficient observation of cosmic rays and neutrino-induced cascades. As radio detection continues to evolve, it holds the potential to significantly enhance our understanding of the highest-energy phenomena in the universe, bridging the gap between cosmic rays and their astrophysical sources[103]. Detailed discussions on radio detection techniques and their applications are presented in the following sections.

1.4 Neutrino Overview

Neutrinos are fundamental particles in the SM of particle physics, distinguished by their incredibly small mass and lack of electric charge. Neutrinos interact weakly with matter, enabling them to journey unimpeded across cosmic distances and preserve details of their astrophysical origins. Since their initial theoretical proposal by Wolfgang Pauli in 1930, neutrinos have become indispensable tools in understanding both astrophysics and particle physics[105, 109]. The study of neutrinos spans a range of energies and processes,

doi:10.6342/NTU202500216

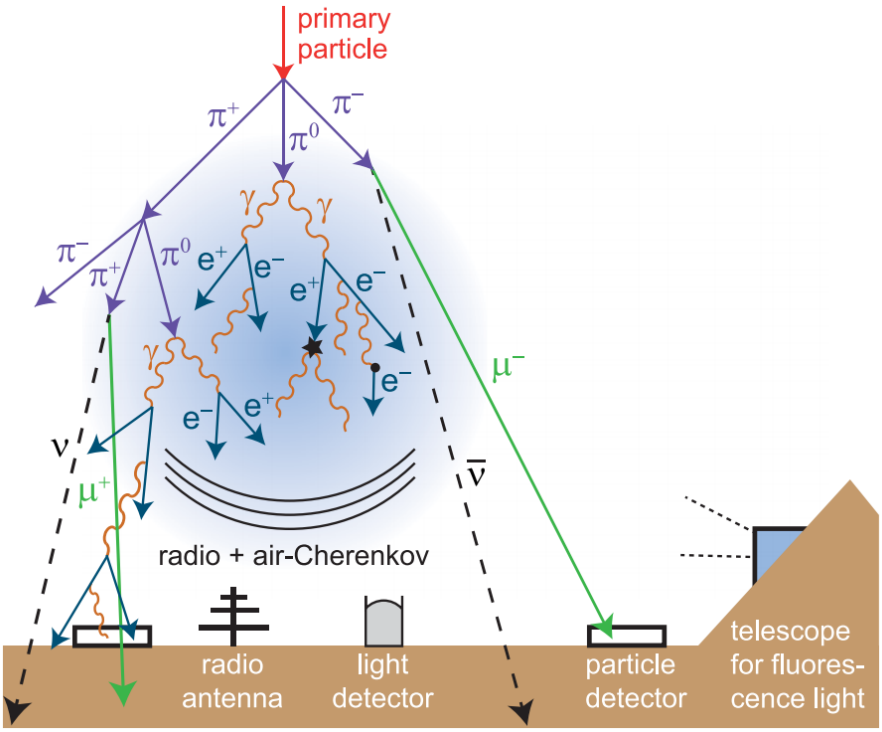

Figure 1.4: Simplified sketch of an air shower caused by a cosmic ray interacting with the atmosphere and possible detection techniques. The shower consists of secondary particles propagating toward the ground, emitting Cherenkov and radio signals. Detection methods include ground-based particle detectors, radio antenna arrays, and fluorescence telescopes, which observe different components of the shower to reconstruct its properties. Adapted from Ref. [114].

doi:10.6342/NTU202500216

from the sub-eV scale relevant to cosmology to the ultra-high-energy (UHE) range associated with cosmic accelerators. Fig. 1.5 shows all-flavor neutrino spectrum from various sources, with solid curves representing neutrinos and dashed or dotted curves indicating antineutrinos. The figure highlights contributions from multiple origins, including cosmic, terrestrial, and astrophysical sources[132].

This section explores the significance of neutrinos, the physics governing their behavior, and their diverse astrophysical and experimental manifestations. Particular emphasis is placed on UHE neutrinos, their detection, and their role as messengers in multi-messenger astronomy.

1.4.1 The Need for the Neutrino

The existence of the neutrino was first hypothesized to resolve discrepancies in beta decay. Early experiments appeared to violate the conservation of energy, momentum, and angular momentum. Wolfgang Pauli proposed the neutrino as a "desperate remedy", a neutral particle that carried away the missing energy and momentum[105]. In 1956, Cowan and Reines provided the first experimental confirmation of neutrinos through reactor neutrino detection[109].

Beyond beta decay, neutrinos are essential to our understanding of several astrophysical phenomena. Being electrically neutral, neutrinos are immune to electromagnetic fields and pass through matter with minimal interaction[111]. This property allows neutrinos to act as unparalleled messengers, escaping dense regions like supernova cores or black hole accretion disks, which are opaque to photons[96].

In modern astrophysics, neutrinos are indispensable for: probing the interiors of stel-

doi:10.6342/NTU202500216

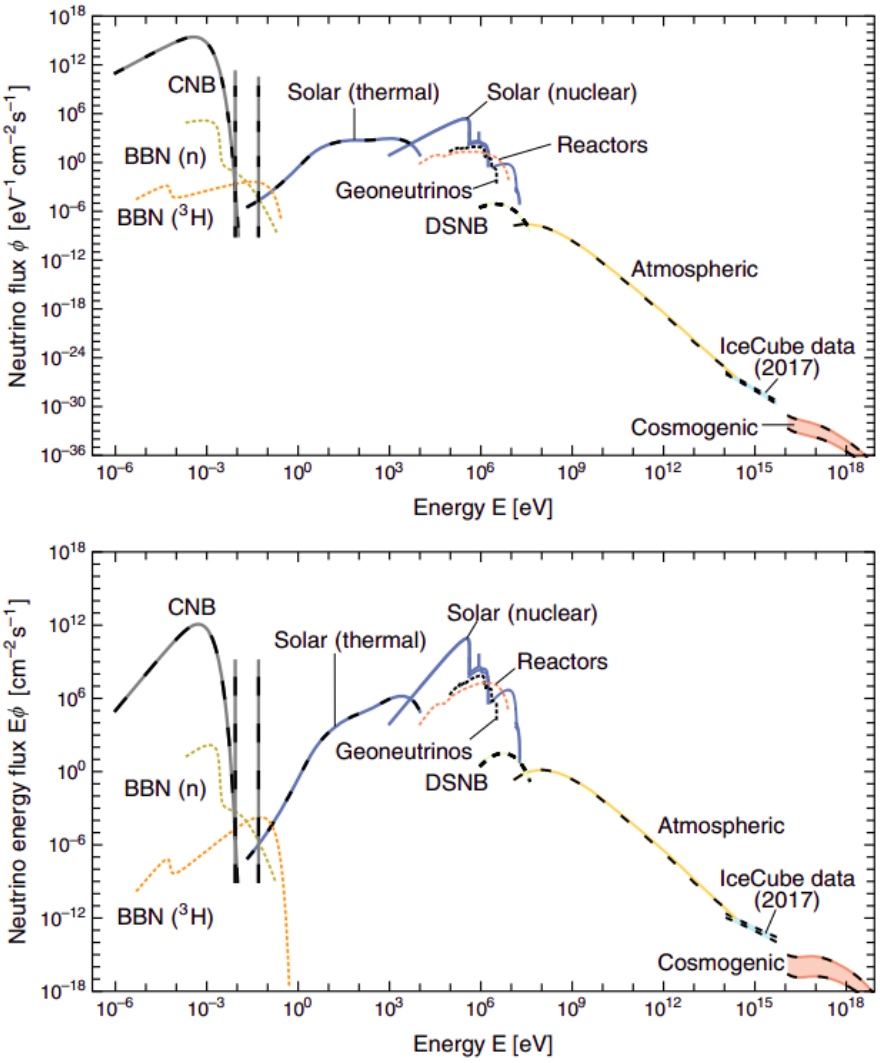

Figure 1.5: All-flavor neutrino spectrum from various sources, with solid curves representing neutrinos and dashed or dotted curves indicating antineutrinos. Contributions from cosmic, terrestrial, and astrophysical origins are highlighted. Adapted from Ref. [132].

doi:10.6342/NTU202500216

lar objects, as seen in the detection of neutrinos from Supernova 1987A; studying the role of hadronic processes in cosmic accelerators; exploring fundamental physics, such as mass generation and the behavior of weak interactions at extreme energies[33, 44, 87, 97].

1.4.2 Neutrino Oscillation

One of the most significant challenges to the SM arises from the discovery of neutrino oscillations, a phenomenon in which neutrinos change flavor (e, μ, or τ) during propagation. This occurs because neutrinos are created and detected as flavor eigenstates but propagate as mass eigenstates, which are quantum superpositions of the flavor states. The three mass eigenstates possess slightly different masses, resulting in phase differences that interfere constructively or destructively over time, producing the observed oscillations[86]. Experimentally confirmed through atmospheric, solar, reactor, and accelerator neutrino studies, this behavior conclusively demonstrates that neutrinos have mass, a property not accounted for in the original SM framework[61].

The discovery of neutrino oscillations necessitates theoretical extensions to account for their small but nonzero masses. One such extension involves the introduction of right-handed neutrinos, also known as sterile neutrinos, which are hypothesized to act as the right-handed counterparts to the SM's left-handed neutrinos. Sterile neutrinos interact only gravitationally and are unaffected by the weak force, allowing them to explain neutrino masses without directly altering the SM's particle interaction framework[50]. Another prominent extension is the seesaw mechanism, which posits the existence of heavy neutrino states that mix with light SM neutrinos. This interaction naturally explains the observed smallness of neutrino masses by leveraging the large mass difference between the light and heavy states, thereby producing the mass hierarchy observed in neutrino ex-

doi:10.6342/NTU202500216

periments[53]. These developments provide an indirect glimpse into physics beyond the SM, raising fundamental questions about the origin of mass, the structure of the neutrino mass hierarchy, and potential links to cosmological phenomena such as dark matter and the evolution of the early universe[54].

1.4.3 Neutrino Interactions

Neutrino interactions play a central role in understanding the behavior and detection of these elusive particles. As neutral, weakly interacting particles, neutrinos interact with matter predominantly via the weak nuclear force, mediated by $W^{\pm}$ and Z^{0} bosons[23]. The rarity of these interactions is both a challenge for detection and an opportunity to probe extreme energy scales and dense environments. The key interaction processes of neutrinos include charged-current (CC) interactions, neutral-current (NC) interactions, and neutrino-electron scattering[110]. The Feynman diagrams for CC and NC interactions are shown in Fig. 1.6.

In a charged-current interaction, a neutrino exchanges a $W^{\pm}$ boson with a target particle, transforming the neutrino into its corresponding charged lepton. For example:

$$\nu_{\ell} + n \rightarrow \ell^{-} + p, \tag{1.4}$$

$$\overline{\nu}_{\ell} + p \rightarrow \ell^{+} + n. \tag{1.5}$$

Here,ν_{ℓ} represents a neutrino of flavor ℓ (e,μ,τ), and ℓ^{-} is the corresponding charged lepton (electron, muon, or tau). The resulting charged lepton leaves a distinct signature that is often used to identify the flavor of the interacting neutrino. CC interactions are essential for high-energy neutrino detection, as they deposit significant energy into the

doi:10.6342/NTU202500216

detector medium, producing extensive cascades of secondary particles[10].

In a neutral-current interaction, a neutrino exchanges a Z^0 boson with a target particle, transferring energy and momentum without changing its flavor:

$$\nu_\ell + N \rightarrow \nu_\ell + N^*. \tag{1.6}$$

Here, N represents a nucleon, and N^* is the nucleon in an excited state. Unlike CC interactions, NC interactions leave the neutrino unchanged, with less energy deposited into the detector. As a result, NC events are harder to detect and provide less information about the flavor or energy of the incident neutrino[84].

Neutrinos can also scatter off electrons via both CC and NC interactions. For example:

$$\nu_e + e^- \rightarrow \nu_e + e^-. \tag{1.7}$$

This process, though rare due to the small cross-section, is significant in precise neutrino flux measurements and studies of neutrino properties. The recoil electron from such interactions carries information about the incoming neutrino's energy and direction[20].

The likelihood of a neutrino interacting with matter is quantified by its interaction cross-section, which depends on the neutrino's energy and the type of interaction. At low energies, neutrino interactions are governed by Fermi's theory of weak interactions, with cross-sections proportional to the square of the neutrino energy ($\sigma \propto {E_\nu}^2$). At UHE ($> 10^{15} eV$), cross-sections increase significantly, making neutrino interactions more likely in dense media. However, even at these high energies, the interaction probabilities remain small, requiring large detector volumes for effective observation[62, 94].

doi:10.6342/NTU202500216

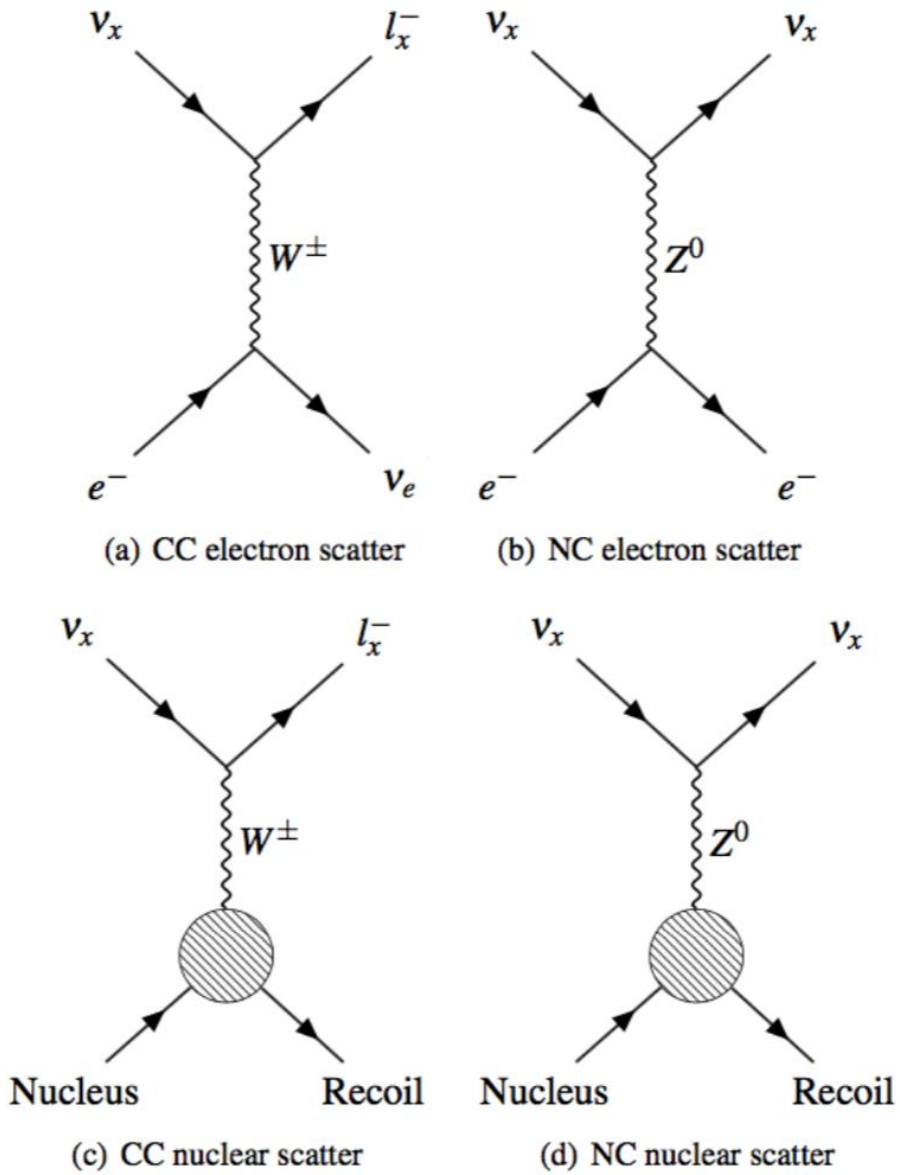

Figure 1.6: Feynman diagrams illustrating charged current (CC) and neutral current (NC) interactions between neutrinos and electrons or nuclei. In the case of ν_e, lepton scattering diagrams interfere, while for ν_μ and ν_τ, they occur as separate processes. Antineutrino ($\bar{\nu}$) diagrams are not shown but are similar, with $\bar{\nu}_e e^- \to W^-$ occurring via an s-channel, leading to the Glashow resonance. Neutrino-nucleon (νN) scattering involves underlying νq or $\nu \bar{q}$ sub-processes. Adapted from Ref. [121].

doi:10.6342/NTU202500216

1.4.4 Astrophysical Neutrinos

Astrophysical neutrinos are high-energy neutrinos produced in some of the most extreme environments in the universe. These neutrinos are byproducts of high-energy cosmic phenomena, such as supernovae, GRBs, AGNs, and cosmic ray interactions with matter and radiation. Their ability to traverse vast distances without deflection or significant energy loss makes them invaluable messengers for probing astrophysical sources and understanding fundamental physical processes[112].

Astrophysical neutrinos are primarily generated through hadronic interactions, where high-energy cosmic rays interact with surrounding matter or photon fields. These interactions produce charged pions ($\pi^{\pm}$) and kaons ($K^{\pm}$), which subsequently decay into neutrinos:

$$\pi^{+} \rightarrow \mu^{+} + \nu_{\mu} \ \ and \ \ \mu^{+} \rightarrow e^{+} + \nu_{e} + \overline{\nu}_{\mu}, \tag{1.8}$$

$$\pi^{-} \rightarrow \mu^{-} + \overline{\nu}_{\mu} \ \ and \ \ \mu^{-} \rightarrow e^{-} + \overline{\nu}_{e} + \nu_{\mu}. \tag{1.9}$$

These decay chains produce neutrinos of all three flavors (ν_e, ν_μ, ν_τ) in roughly equal proportions after accounting for neutrino oscillations over cosmic distances. Such neutrinos span a broad energy range, from $\sim 10^{11}\ eV$ to beyond $10^{20}\ eV$, with higher-energy neutrinos linked to the most extreme astrophysical sources[27]. The energy spectra observed for very-high-energy gamma rays (VHEGRs) by Fermi-LAT, high-energy astrophysical neutrinos by IceCube, and UHECRs by Auger exhibit comparable energy flux levels, as illustrated in Fig. 1.7[11].

doi:10.6342/NTU202500216

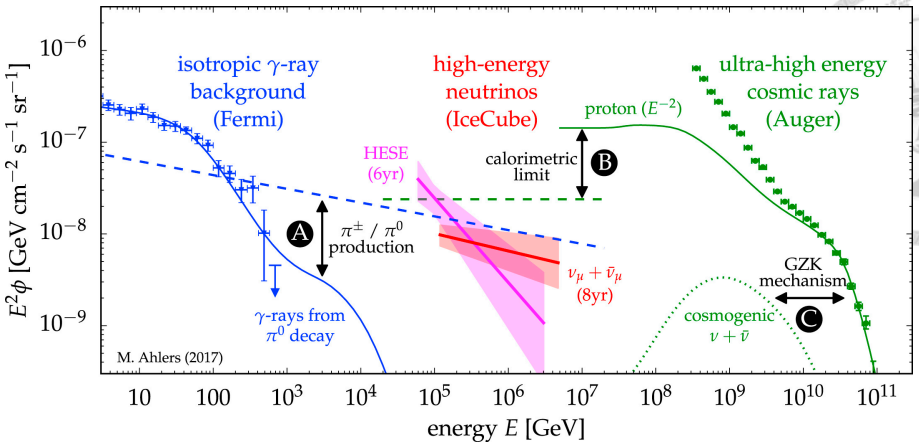

Figure 1.7: The spectral flux of neutrinos, inferred from the eight-year IceCube upgoing track analysis (red fit) and the six-year HESE analysis (magenta fit), is compared to the flux of unresolved extragalactic gamma-ray sources (blue data) and ultra-high-energy cosmic rays (green data). The neutrino spectra are shown with the best-fit power-law (solid line) and the corresponding 1σ uncertainty range (shaded area). Adapted from Ref. [11].

1.4.5 GZK Effect and Cosmogenic Neutrinos

The Greisen-Zatsepin-Kuzmin (GZK) effect, independently proposed by Kenneth Greisen, Georgi Zatsepin, and Vadim Kuzmin in 1966, describes the energy attenuation of UHECRs as they propagate through intergalactic space[72]. When UHECRs protons reach energies above $\sim\ 5 \times 10^{19}\ eV$, they interact with the photons of the CMB via photopion production:

$$p + \gamma_{CMB} \rightarrow \Delta^+ \rightarrow \pi^0 + p \ \ or \ \ \pi^+ + n \tag{1.10}$$

where Δ^+ is a resonance state formed during the interaction. And π^0 decays into gamma rays, while π^+ decays into neutrinos and muons.

This interaction limits the maximum energy of UHECRs that can reach Earth, as they lose energy to pion production over cosmological distances. This energy loss process is characterized by the GZK energy threshold, which depends on the center-of-mass energy

doi:10.6342/NTU202500216

required for such interactions and is determined by the energy spectrum of CMB photons. The GZK effect imposes an effective horizon for UHECRs, beyond which higher-energy particles are unlikely to survive their journey to Earth[13]. This suppression is evident in the observed UHECR spectrum, where the flux drops sharply at energies above $\sim 10^{19.7}\ eV$[67].

1.4.6 Messengers of the UHE Universe

UHE neutrinos are indispensable messengers in multi-messenger astrophysics, providing a direct link to the most extreme and energetic processes in the universe. Unlike photons, which can be absorbed or scattered, and cosmic rays, which lose directional information due to magnetic deflections, neutrinos travel vast cosmic distances unaffected, carrying unaltered information about their sources. Fig. 1.10 shows the survival fraction of UHECRs with different compositions as a function of travel distance, and the detection horizons of cosmic messengers, including protons, photons, and neutrinos, at various energy scales. UHE neutrinos are generated in extreme environments, including GRBs, active AGNs, and during the interactions of UHECRs with the CMB[60]. For example, the detection of a high-energy neutrino by IceCube in 2017, coinciding with a blazar flare, confirmed neutrino production in AGNs, marking a milestone in identifying astrophysical sources of UHE particles[5, 43, 44].

In addition to tracing cosmic accelerators, UHECNs enable tests of fundamental physics at energy scales far beyond those achievable in laboratories. Fig. 1.8 shows the neutrino-nucleon cross section measurements from various experiments. Summary of the connections between various BSM physics scenarios and neutrino observables is shown in Fig. 1.9. Their interactions provide valuable data on neutrino-nucleon cross-sections,

doi:10.6342/NTU202500216

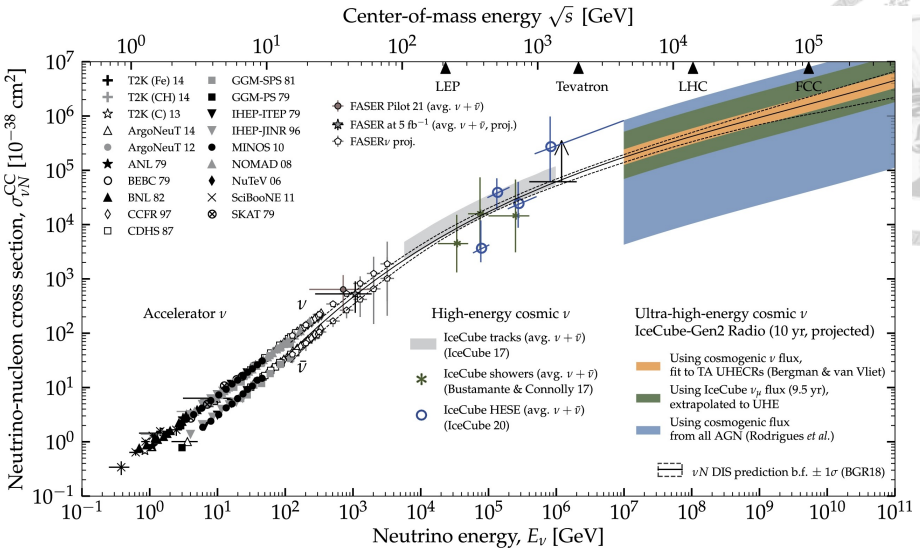

Figure 1.8: Neutrino-nucleon cross section measurements from various experiments (markers), with IceCube providing measurements at the highest energies. The black solid line and dashed band represent the model prediction. Colored bands illustrate the future prospects for IceCube-Gen2 in the UHE regime. Adapted from Ref. [8].

weak interaction dynamics, and potential deviations from the SM. By correlating neutrino detections with gravitational waves, photons, or cosmic rays, researchers can construct a more comprehensive picture of high-energy astrophysical events, such as black hole mergers or supernovae[126]. Future observatories like IceCube-Gen2, PUEO, and GRAND will further enhance sensitivity, offering the potential to uncover new physics and deepen our understanding of the extreme universe[5, 14, 131].

1.5 Radio Detection of Ultra High Energy Cosmic Particles

The detection of UHECRs and UHE neutrinos via radio techniques has revolutionized the field of particle astrophysics. The underlying principle is based on the coherent electromagnetic radiation emitted by charged particles in extensive particle cascades. Radio detection offers a powerful tool for studying UHE particles due to its ability to cover

doi:10.6342/NTU202500216

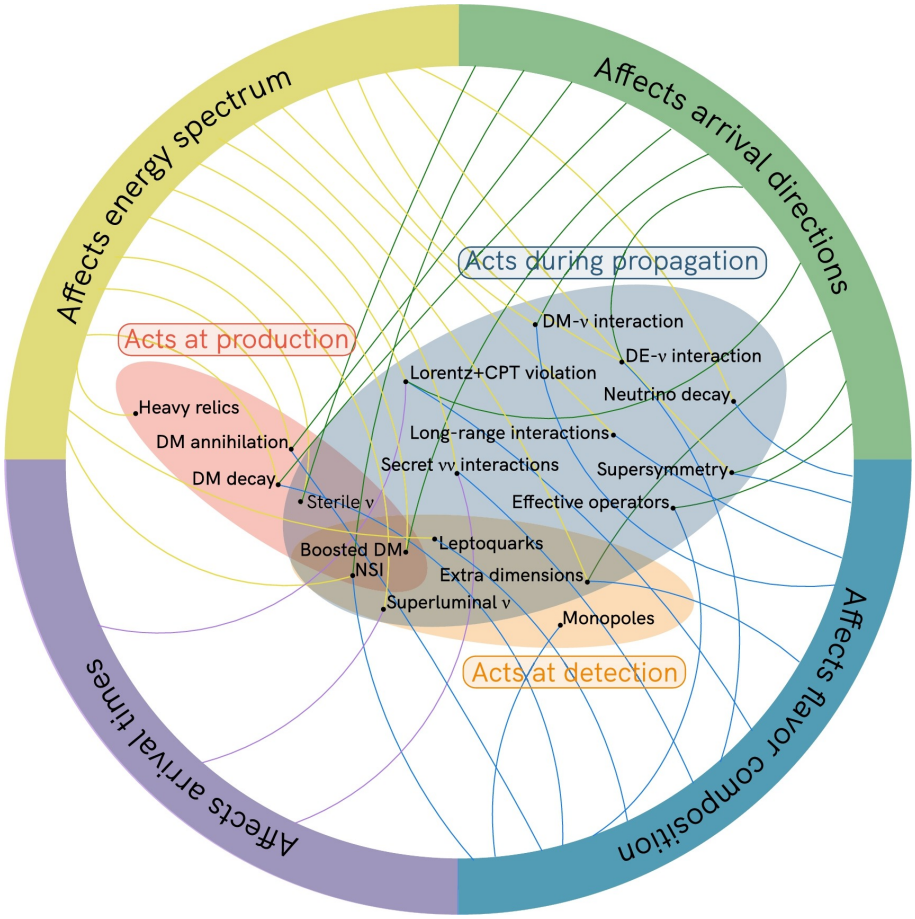

Figure 1.9: Summary of the connections between various beyond Standard Model physics scenarios and neutrino observables. Adapted from Ref. [8].

doi:10.6342/NTU202500216

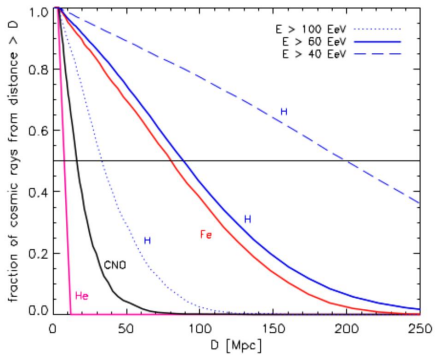

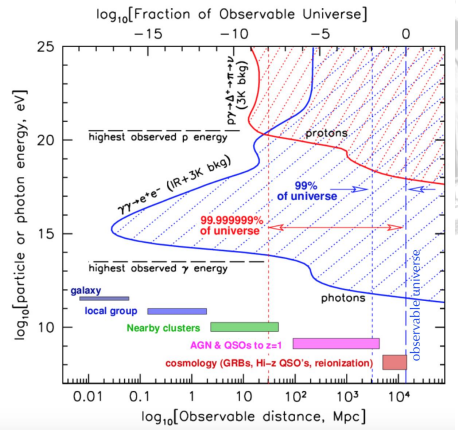

Figure 1.10: Left: The survival fraction of UHECRs with different compositions as a function of travel distance D (in Mpc). Hydrogen ions are displayed for energies $E > 40$, 60, and 100 EeV, while heavy ions such as iron are shown for $E > 60$ EeV. The solid horizontal line represents the 50% survival rate. Adapted from Ref. [88]. Right: The detection horizons of cosmic messengers, including protons, photons, and neutrinos, at various energy scales. The highest observed energies for protons and gamma rays are indicated in the plot. Protons at 10^{20} eV can only be observed within 100 Mpc due to attenuation caused by the GZK effect, excluding the red-shaded region. Gamma rays are limited as UHE messengers because of pair production with infrared and CMB photons, excluding them from the blue-shaded region. Neutrinos, in contrast, can traverse the entire universe up to 10^{25} eV, as the universe remains transparent to them. Adapted from Ref. [34].

large areas, operate continuously, and achieve sensitivity across vast energy ranges[82]. This section elaborates on the physics of particle cascades, mechanisms of radio emission, and the application of these principles in modern experiments, with a focus on the TAROGE experiment.

1.5.1 Particle Cascades

When UHE particles interact with matter, they initiate a cascade of secondary particles, commonly referred to as EAS in the atmosphere or particle showers in dense media. Left hand side of Fig. 1.11 is the sketch of an EAS induced by UHECR proton or nucleus. These cascades are characterized by their high particle multiplicity and the broad distribution of energies among the secondary particles. The evolution of such cascades

doi:10.6342/NTU202500216

is governed by a series of physical interactions that depend on the nature of the primary particle and the medium it traverses[56]. The processes governing particle cascades fall into two main categories: electromagnetic showers and hadronic showers[82].

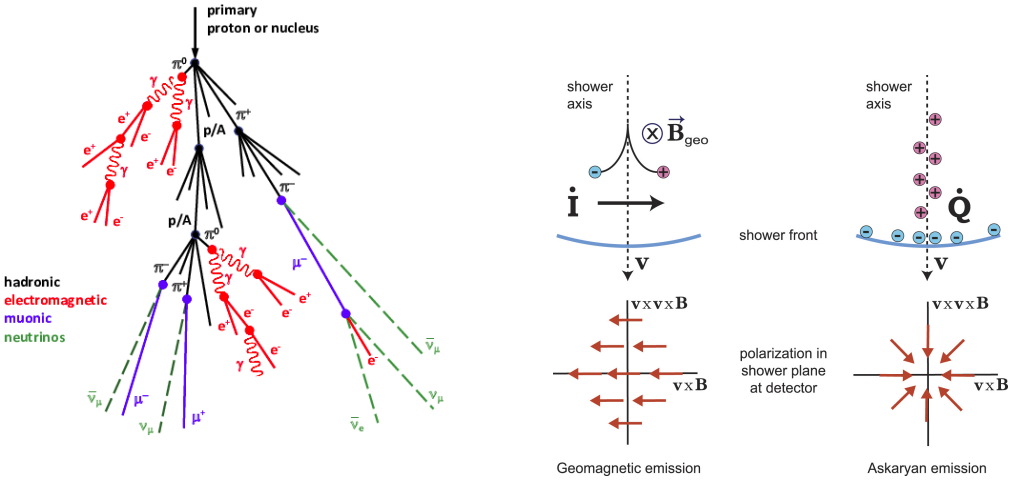

Figure 1.11: Left: Sketch of an EAS induced by a UHECR proton or nucleus, showing its key components: hadronic (black), electromagnetic (red), muonic (blue), and neutrino (green). Adapted from Ref. [9]. Right: Emission mechanisms relevant at typical observation frequencies (ranging from a few MHz to a few GHz) include geomagnetic and Askaryan emissions. Geomagnetic emission arises from the induction of a transverse current in the shower front, resulting in polarization aligned with the geomagnetic Lorentz force. In air, this mechanism is generally stronger than the Askaryan emission, which is caused by the time variation of the net charge excess in the shower front and is the dominant mechanism in dense media. For air showers, the observed radio emission is the coherent combination of both mechanisms. Depending on the local orientation of the electric-field vectors, the interference between the two can be constructive or destructive. The electric field's direction follows Lenz's law, which states that the induced field counteracts the cause of its origin. Consequently, the orientation of the electric field is constant for geomagnetic effects, while for the Askaryan effect, it reverses after the shower maximum as the charge excess begins to decrease. Adapted from Ref. [114].

Electromagnetic showers dominate when the primary particle is a photon or electron. These cascades grow via bremsstrahlung and pair production:

$$\gamma + Z \rightarrow e^+ + e^- + Z \tag{1.11}$$

$$e^\pm + Z \rightarrow e^\pm + \gamma + Z \tag{1.12}$$

doi:10.6342/NTU202500216

At high energies, photons generate electron-positron pairs, and the resulting electrons and positrons emit bremsstrahlung photons when deflected by the Coulomb fields of nuclei (Z) in the medium. The process continues until the energy of the secondary particles drops below the critical energy (E_c), where ionization losses dominate, halting further particle multiplication.

Hadronic showers, initiated by protons or heavier nuclei, involve inelastic collisions with target nuclei in the medium:

$$p + A \rightarrow \pi^0 + \pi^{\pm} + other\ secondaries \tag{1.13}$$

Here, neutral pions (π^0) decay almost instantly into gamma rays, contributing to electromagnetic subshowers:

$$\pi^0 \rightarrow \gamma + \gamma \tag{1.14}$$

Charged pions ($\pi^{\pm}$) decay into muons and neutrinos, forming the characteristic muonic component of hadronic showers:

$$\pi^{\pm} \rightarrow \mu^{\pm} + \nu_{\mu}(\overline{\nu}_{\mu}) \tag{1.15}$$

The longitudinal development of a particle cascade, describing the evolution of the number of particles $N(X)$ as a function of the atmospheric depth X, is well modeled by the Gaisser-Hillas function[98]:

$$N(X) = N_{max}(\frac{X - X_0}{X_{max} - X_0})^{\frac{X_{max} - X_0}{\lambda}} e^{\frac{X_{max} - X}{\lambda}} \tag{1.16}$$

doi:10.6342/NTU202500216

where: X_0 is the depth at which the shower starts, X_{max} is the depth at which the particle number reqches its maximum, λ is the interaction length scale of the particles and N_{max} is the maximum number of particles in the shower.

Electromagnetic showers tend to reach X_{max} deeper in the atmosphere due to the longer mean free path of photons, while hadronic showers, involving larger cross-sections for nuclear interactions, develop earlier and produce a broader distribution of secondary particles[91].

The shower profile and its features—such as X_{max}—are influenced by the energy and type of the primary particle, as well as the density and composition of the medium. These parameters are critical for reconstructing the properties of the original UHE particle. Theoretical modeling of particle cascades plays a central role in advancing our understanding of UHECRs and UHECNs detection methods[108].

1.5.2 Electromagnetic Radiation from Moving Particles

Charged particles in motion emit electromagnetic radiation when accelerated. The total power radiated is governed by the relativistic Larmor formula:

$$P = \frac{\gamma^4 q^2 a^2}{6\pi\epsilon_0 c^3} \tag{1.17}$$

where: P is the total radiated power, $\gamma = \frac{1}{\sqrt{1-\frac{v^2}{c^2}}}$ is the Lorentz factor, q is the charge of the particle, a is the acceleration of the particle, ϵ_0 is the permittivity of free space, and c is the speed of light[136].

The total energy radiated depends on the particle's charge and acceleration, making

doi:10.6342/NTU202500216

high-energy charged particles in cascades efficient sources of radiation. Two primary mechanisms dominate the production of electromagnetic radiation in EAS: geomagnetic emission and Askaryan effect as illustrated in the right hand side of Fig. 1.11[82, 114].

1.5.2.1 Cherenkov Radiation

Cherenkov radiation occurs when a charged particle moves through a dielectric medium at a speed greater than the phase velocity of light in that medium ($v > c/n$, where n is the refractive index of the medium). This creates a coherent shockwave of electromagnetic radiation, analogous to a sonic boom in air. The Cherenkov angle (θ_c) at which the radiation is emitted is given by:

$$cos(\theta_c) = \frac{1}{n\beta} \tag{1.18}$$

where: $\beta = v/c$, is the velocity of the particle as a fraction of the speed of light, n is the refractive index of the medium and θ_c is the Cherenkov angle.

Cherenkov radiation is characterized by its conical emission pattern, which depends on the velocity and refractive index of the medium. In EAS, Cherenkov radiation occurs predominantly at optical and ultraviolet wavelengths but can extend into the radio regime due to coherent radiation effects. This is especially significant for dense media like ice, salt, or the lunar regolith, where coherent Cherenkov radiation forms the basis for Askaryan radiation detection[85]. The intensity of Cherenkov radiation increases with the square of the particle's charge (q^2) and depends on the refractive properties of the medium.

doi:10.6342/NTU202500216

1.5.2.2 Askaryan Effect

The Askaryan effect, first proposed by Gurgen Askaryan in 1962, builds on the principles of Cherenkov radiation but specifically describes the production of coherent radio-frequency radiation in dense media during the development of particle cascades[22]. As a high-energy particle interacts with the medium, a cascade of secondary particles is generated, leading to a net charge asymmetry within the shower. This asymmetry arises from two primary processes: the annihilation of positrons with electrons and the ionization of atoms, which liberates additional electrons. This excess of negative charge produces a time-varying current that emits coherent radiation at the Cherenkov angle, with the intensity of the emitted radio waves scaling as N^2, where N is the number of particles in the cascade. The coherence of the radiation at radio frequencies enhances the detectability of high-energy particle interactions, making the Askaryan effect particularly effective for observing UHECNs and UHECRs over large distances[16].

1.5.2.3 Geomagnetic Emission

This mechanism arises when charged particles in EAS are deflected by the Earth's geomagnetic field. The deflection causes the particles to accelerate, creating a transverse current that emits RF radiation, commonly referred to as geo-synchrotron radiation.

The production of geo-synchrotron radiation is governed by the interaction between the charged particles' velocity vector ($\overrightarrow{v}$) and the Earth's magnetic field ($\overrightarrow{B}$), as described by the Lorentz force:

$$\overrightarrow{F} = q(\overrightarrow{v} \times \overrightarrow{B}) \tag{1.19}$$

doi:10.6342/NTU202500216

The emitted radio waves are linearly polarized, with the polarization direction aligned perpendicular to both the particle's velocity and the geomagnetic field, providing a distinctive signature that is critical for reconstructing the direction of the primary UHE particle. Geo-synchrotron radiation spans a broad range of frequencies, but coherence effects dominate in the MHz range ($\sim$ 30−300 MHz) for air showers. Coherent radiation arises when the wavelength of the emitted radiation is larger than the separation of individual charges in the cascade, leading to an amplification of the signal. The radiation is strongest in the forward direction of the shower, with a characteristic cone-shaped emission pattern. The angular spread depends on the energy and composition of the primary particle, as well as the density and geometry of the atmosphere[2].

1.5.3 Radio Antenna Array on High Altitude

High-altitude radio antenna arrays play a pivotal role in detecting UHECRs and UHECNs by capturing RF emissions produced during particle cascades. By deploying arrays in high altitude, such as high-altitude balloons or mountain tops, these systems leverage their elevated vantage points to cover vast detection areas and observe near-horizontal or Earth-skimming particle interactions[103, 135]. With its scalability, day-night operational capability, and direct correlation between signal intensity and primary particle energy, These arrays are particularly well-suited for capturing near-horizontal air showers, including those induced by Earth-skimming neutrinos.

1.5.3.1 ANITA Anomalous Events

ANITA experiment is a high-altitude radio antenna array carried by a balloon flying at altitudes of $\sim$ 37 km over Antarctica. Its location and altitude provide a large

doi:10.6342/NTU202500216

detection volume, enabling the experiment to capture rare signals over distances exceeding $1,000\ km$. The array is sensitive to radio pulses in the 200–1000 MHz frequency band, particularly those generated by the Askaryan effect in Antarctic ice[103]. Additionally, ANITA can capture radio signals emitted by cosmic ray-induced air showers, either directly from above the horizon or through reflections off the ice, as shown in Fig. 1.12.

ANITA's design enables differentiation between UHECR signals and potential UHE ν_τ-induced events based on the polarity of the detected signal. Signals originating from above the horizon are identified as CR-induced, while signals from below the horizon are classified as either reflected CR signals, marked by inverted polarity, or upward-going tau neutrino events, characterized by a lack of phase inversion. Across four flights (ANITA-I to IV), the experiment recorded 60 UHECR events, including 54 reflected signals and 6 direct ones. However, it is the detection of six upward-going air shower events, dubbed "ANITA anomalous events" (AAEs), that has generated considerable interest and debate[68–70].

The AAEs are distinct for their reconstructed shower energies around the EeV scale and characteristics resembling those of UHE τ neutrino interactions. Notably, two AAEs detected during ANITA-I and III flights exhibited steep elevation angles of $-27°$ and $-35°$ below the horizon, corresponding to paths through the Earth much longer than the expected interaction lengths of ν_τ under the SM. These events present a survival probability for ν_τ that appears inconsistent with diffuse neutrino flux limits established by experiments like IceCube and the Pierre Auger Observatory, making their SM origin unlikely. Four additional AAEs observed during ANITA-IV occurred at shallower angles (within $1°$ below the horizon) but similarly challenge the hypothesis of τ neutrino origins, given the constraints from existing diffuse flux limits and ANITA's own sensitivity in the Askaryan

doi:10.6342/NTU202500216

detection channel. The lack of lower-energy neutrino counterparts observed by IceCube further complicates τ neutrino interpretation[4].

Numerous alternative explanations for AAEs have been proposed, ranging from known physics to BSM scenarios. Hypotheses involving known phenomena include coherent transition radiation emitted when cosmic ray-induced air showers interact with the air-ice interface or subsurface reflections within the ice that bypass phase inversion[51, 116]. However, these models have faced scrutiny and are largely disfavored by subsequent analyses, including data from the HiCal-2 pulser and ANITA-IV[117]. On the other hand, BSM physics models offer intriguing possibilities, such as sterile neutrinos, supersymmetric particles, or other exotic mechanisms, yet these remain speculative without further supporting evidence. The precise origin of AAEs remains an open question, requiring additional observations and improved statistics to unravel their nature[18, 37, 63, 77, 80].

Despite its groundbreaking discoveries, ANITA's balloon-borne platform imposes inherent limitations, including a relatively low duty cycle of approximately one month per flight every three years, which restricts its overall exposure. To address these constraints, ANITA's successor, PUEO (Payload for Ultrahigh Energy Observations), is under development[6]. PUEO aims to significantly enhance sensitivity by incorporating additional antennas and implementing advanced interferometric beamforming triggers using RF System-on-Chip (RFSoC) technology. These advancements promise to improve the detection capabilities and shed further light on the mysteries of UHECRs, UHE neutrinos, and the enigmatic anomalous events observed by ANITA.

doi:10.6342/NTU202500216

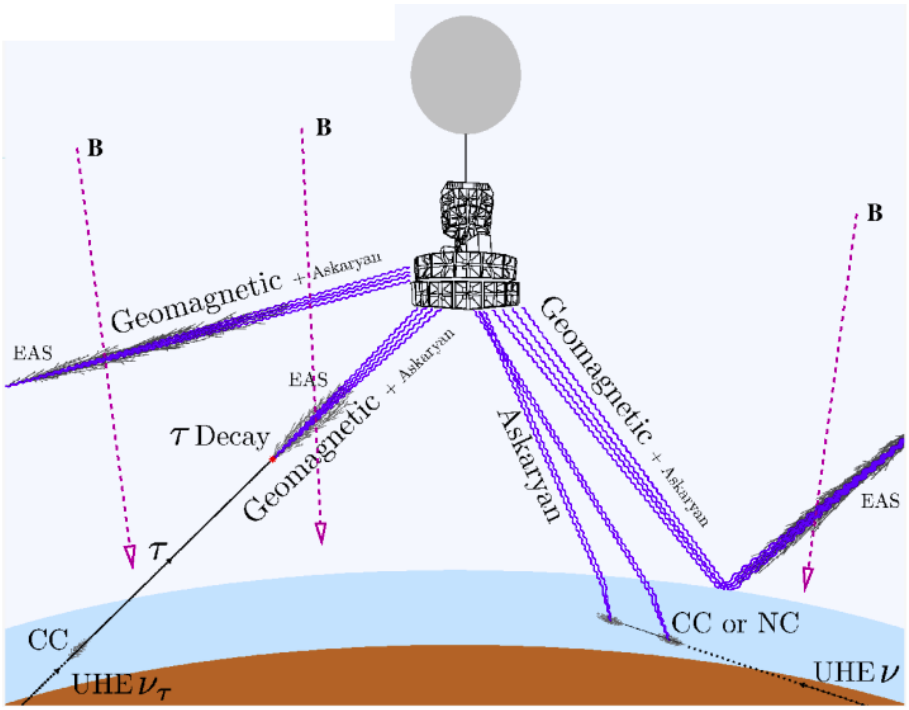

Figure 1.12: The detection concept of ANITA in the near-vertical Antarctic geomagnetic field. Geomagnetic signals from cosmic rays (CR) can be observed either directly or via reflection and include a small contribution from Askaryan radiation. Under-ice neutrino detection relies on Askaryan radiation, which dominates and originates from multiple particle showers caused by primary and secondary interactions. Additionally, geomagnetic signals may be produced by extensive air showers (EAS) initiated by τ-lepton decay following ν_τ charged-current (CC) interactions within the ice. Adapted from Ref [68].

doi:10.6342/NTU202500216

1.5.3.2 Radio Antenna Array on High Mountains

Deploying radio antenna arrays on high mountains provides an alternative approach to enhance exposure and rapidly collect more anomalous AAEs. These high-altitude detectors offer a wide field of view toward the horizon, enabling the observation of UHECRs from the sky and UHE ν_τ from below the horizon[140]. Although mountain-based detectors operate at lower altitudes compared to balloon-borne platforms, resulting in a reduced detection volume, they benefit from a lower energy threshold due to proximity to the shower maximum[135]. Additionally, their greater duty cycle and scalability allow for competitive sensitivity over extended observation periods.

Radio experiments leveraging this strategy include TAROGE, BEACON, and GRAND, all of which aim to capture UHECR and neutrino signals with high precision[14, 40, 101, 119, 135]. High-mountain arrays thus provide a practical and efficient complement to balloon-borne systems, enabling continuous observations and contributing significantly to the study of UHECRs and neutrinos.

1.5.4 TAROGE Experiment

1.5.4.1 Detection Concept

TAROGE comprises high-mountain radio antenna arrays designed to detect UHECRs and Earth-skimming UHE ν_τ via RF emissions. Strategically located on the eastern coastal cliffs of Taiwan and Antarctica, TAROGE leverages its unique geographic and atmospheric conditions to monitor near-horizontal EAS over expansive areas, including land and adjacent ocean (or ice). The detection concept, as illustrated in Figure 1.13,

doi:10.6342/NTU202500216

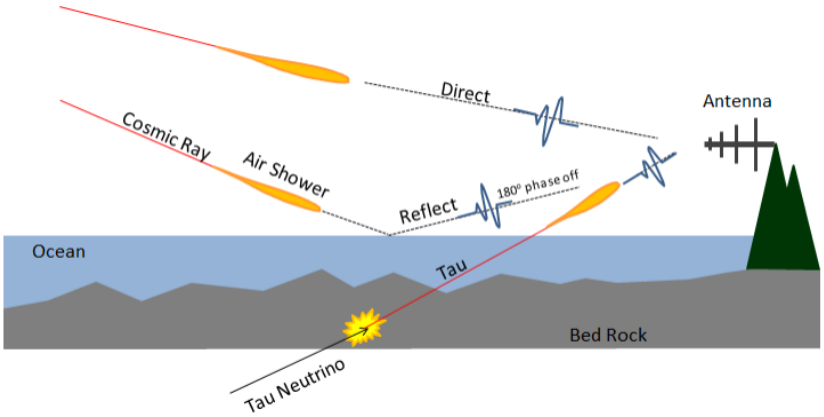

Figure 1.13: The detection concept of TAROGE. Adapted from Ref [101].

highlights TAROGE's ability to detect RF signals from air showers with both direct and surface-reflected paths[40, 101, 135].

TAROGE's design emphasizes practicality and efficiency, with advantages such as low unit cost, ease of deployment, and straightforward maintenance. These features, combined with the array's sensitivity to geomagnetic and Askaryan radiation, make TAROGE particularly effective in capturing radio signals from EAS initiated by Earth-skimming UHE ν_τ and UHECRs. By providing continuous observation capabilities and covering a vast detection area, TAROGE represents a versatile and innovative approach to high-energy particle detection[40].

1.5.4.2 TAROGE Stations in Taiwan and Antarctica

The TAROGE observatory began with the deployment of TAROGE-1 in July 2014 on Yongshih Mountain, Taiwan, at an altitude of 1,000 meters. As a proof-of-concept prototype, TAROGE-1 successfully demonstrated the detection of impulsive RF signals with a pointing resolution better than 0.3°. However, its proximity to anthropogenic noise sources and damage from a typhoon in 2015 led to its retirement. Despite these challenges, TAROGE-1 provided essential data for refining the observatory's design.

doi:10.6342/NTU202500216

TAROGE-2, constructed in late 2015 approximately $1.7\ km$ away from TAROGE-1, featured an off-grid solar power system and an upgraded DAQ system with a wider bandwidth ($350\ MHz$) and a maximum event rate of $40\ Hz$. Improved antenna placement and system design reduced interference, but operations were interrupted in 2018 due to mining activities, and the station was later damaged by lightning in 2021[101].

In 2018, TAROGE-3 was deployed at a higher altitude of 1,090 meters near the TAROGE-2 site. The station employed a phased array of dual-polarized log-periodic dipole antennas (LPDAs) to enhance sensitivity to near-horizontal signals. Its operating frequency range was adjusted to 180–330 MHz to reduce noise, and it achieved the longest operational period among TAROGE stations, spanning over six years. TAROGE-3 highlighted the observatory's capacity for stable long-term observations despite local challenges, such as mining-related noise.

TAROGE-4 (as shown in Fig. 1.14), deployed in August 2019 in Guanyin, Yilan County, at a lower altitude of 675 meters, addressed radio frequency interference (RFI) issues with a quieter operational environment. It introduced a novel trigger module with eight bands by using Surface Acoustic Wave (SAW) filters to improve sensitivity and used drone-based calibration to refine event reconstruction[40]. TAROGE-4's configuration demonstrated the adaptability of the observatory to diverse deployment environments. More details of TAROGE-4 will be introduced in the next chapter.

TAROGE-M, first deployed in January 2020 on Mt. Melbourne at an altitude of $2,700$ meters, marked a significant expansion of the TAROGE observatory. Designed to endure the extreme Antarctic environment, TAROGE-M featured antennas with enhanced mechanical strength, thermal insulation, and a modularized DAQ system, ensur-

doi:10.6342/NTU202500216

Figure 1.14: TAROGE-4 station, LPDA antennas pointing horizontally to ocean. Adapted from Ref [40].

ing resilience against low temperatures and high winds. The station's six antennas, operating in the 180–450 MHz range, achieved an angular resolution of approximately $0.3°$ for high-elevation events through drone-based calibration. During its initial deployment, TAROGE-M operated for 26.3 days, a period shortened by power failures caused by icing and extremely low temperatures. Despite this, it successfully identified seven UHECR candidates with a mean energy of 1 EeV. These results aligned closely with findings from other experiments, demonstrating the station's capability for UHE particle detection[135]. TAROGE-M was redeployed in January 2023 and remained operational for almost one year, further contributing to the study of UHE particles under extreme environmental conditions.

doi:10.6342/NTU202500216

Chapter 2 TAROGE-4 System

This chapter provides a detailed overview of the TAROGE-4 system, which is designed to operate autonomously in a remote, noise-prone environment. Each subsystem is tailored to optimize sensitivity, ensure reliability, and support long-term operations. The following sections outline the system's general design, component specifications, and operational strategies.

2.1 Gneral Design

The establishment of radio observatories for detecting air shower radio pulses necessitates meticulous planning, taking into account geographical factors, accessibility, and environmental conditions. The TAROGE antenna stations are designed with key components to enhance detection sensitivity while ensuring durability in extreme environments. These components include:

- **LPDA Antennas**: Optimized for wideband radio pulse detection.
- **Bandpass Filters**: To isolate the relevant frequency range and reduce noise.
- **Low-Noise Amplifier (LNA) Modules**: To enhance weak signals with minimal distortion.

doi:10.6342/NTU202500216

- **Trigger System**: For real-time identification and recording of significant events.
- **Digitization Module**: Converts the analog signals into digital format, enabling accurate data analysis.
- **Solar Power Systems**: Providing sustainable energy for operations in remote locations.

The whole system architecture of TAROGE-4 is depicted in Fig. 2.1. Each antenna polarization has its own signal chain and the received signal is fed into Radio Frequency (RF) front-end electronics (FEE) which consists of a band-pass filter and a LNA and then processed by the data-acquisition (DAQ) system. Inside DAQ, the RF signals are split into two paths for trigger system and digitizers respectively. This autonomous station is powered by photovoltaic system and the communication with lab service is through 4G network. All active devices are typically housed in electromagnetic interference (EMI) shielding enclosures made of stainless steel or aluminum to prevent radio frequency interference (RFI) with the receivers. Additionally, the DAQ and power systems are enclosed in weatherproof housings to ensure a stable operating environment, protecting them from direct sunlight, rain, and strong winds[40]. The design of each component is described in the following sections.

2.2 Antenna Design and Frequency Response

The chosen antenna for TAROGE-4 is the Log-Periodic Dipole Array (LPDA) due to its wide bandwidth (fractional bandwidth > 1) and high gain ($\sim 7dBi$), making it well-suited for detecting air showers from near-horizontal directions. The LPDA's fishbone-

doi:10.6342/NTU202500216

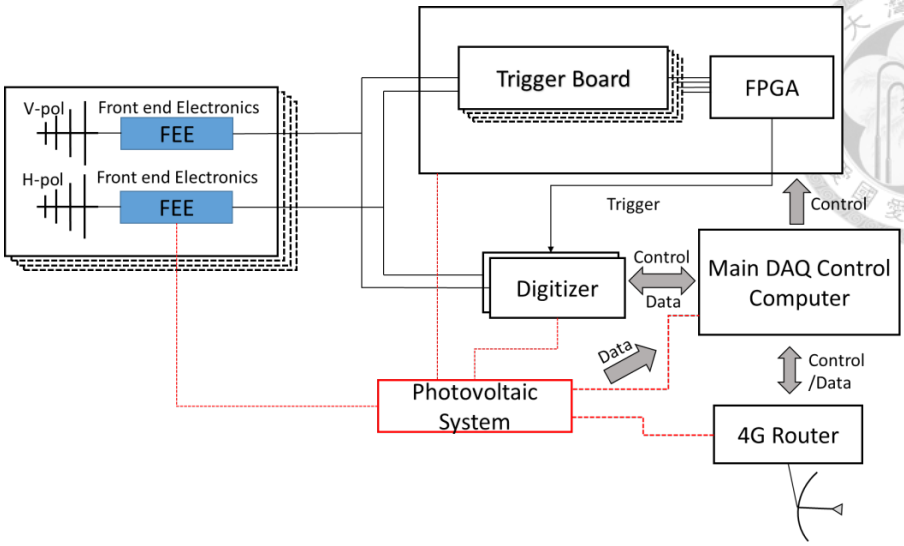

Figure 2.1: TAROGE-4 system architecture. Adapted from Ref. [101].

like structure offers significant advantages, such as being lightweight, portable, and resistant to wind, ensuring durability in typhoon-prone environments.

Although geomagnetic emission is more coherent and stronger at lower frequencies, the lower cutoff frequency of TAROGE-4 LPDAs was set at approximately $180\ MHz$. This decision balances two key factors: the presence of persistent and strong narrowband radio frequency interference (RFI) at selected sites, often in the 90–$180\ MHz$ range (e.g., from FM radio, walkie-talkies, or marine communication), and the need to limit the antenna size to approximately 1.5 meters for easier transportation, installation, and reduced wind resistance.

The angular size of the main lobe, characterized by the $3-dB$ beamwidth, is about $\pm 45°$ in the E-plane (the plane containing the antenna elements that receive the electric field) relative to the boresight and approximately $\pm 60°$ in the H-plane (the plane containing the magnetic field, perpendicular to the E-plane). Both horizontal (H-pol) and vertical (V-pol) antennas exhibit similar performance characteristics.

The TAROGE-4 LPDAs are constructed from $6061-T6$ aluminum alloy tubing,

doi:10.6342/NTU202500216

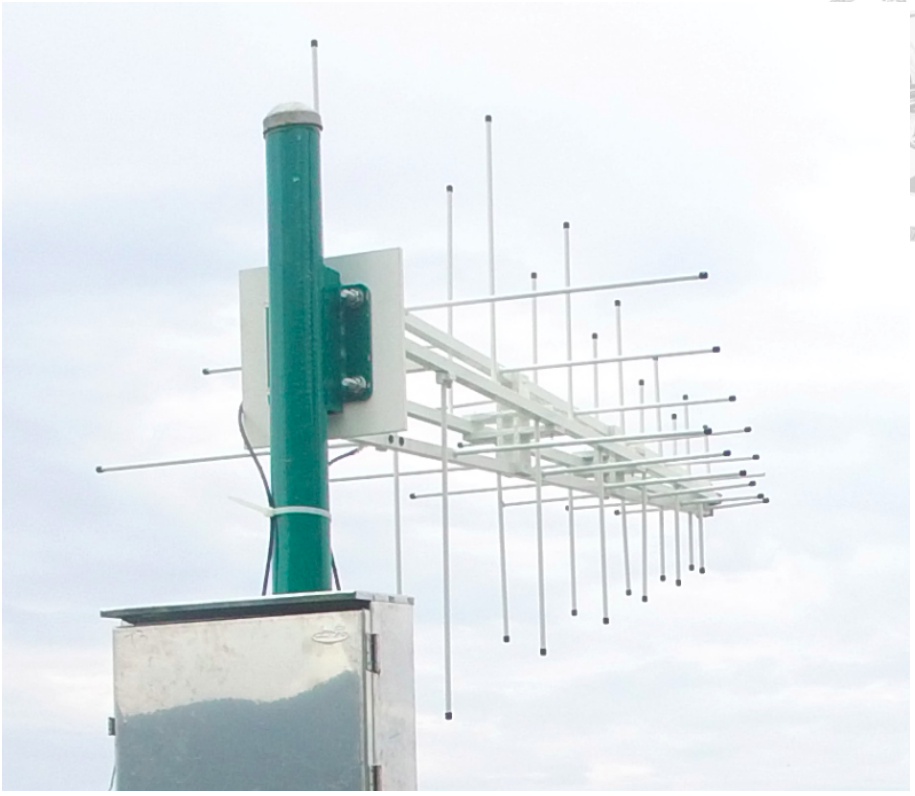

Figure 2.2: TAROGE-4 antennas feature a Christmas-tree-shaped dual-polarization design, with H-pol and V-pol antennas collocated and crossing each other. This configuration enhances polarimetry capabilities and provides structural stability to withstand strong winds.

chosen for its high strength and low weight. The surface is iridited with a chromate conversion coating to maintain conductivity and improve corrosion resistance, followed by a white paint finish to minimize heat absorption from sunlight. The antenna feed features two brass pieces at the front end connected to an RG-400 coaxial cable running inside one of the booms, one piece attached to the cable shield and the other to its central conductor—separated by a bakelite spacer. The antennas use a Christmas-tree-shaped dual-polarization design, with collocated H-pol and V-pol antennas crossing each other (as shown in Fig. 2.2), enhancing polarimetry and structural stability against strong winds.

The TAROGE-4 station, depicted in Fig. 1.14, comprises four antennas mounted on 3.5-meter-high towers, each with independent signal chains for H-pol and V-pol polarizations. These antennas, strategically placed at separate locations, achieve higher directional

doi:10.6342/NTU202500216

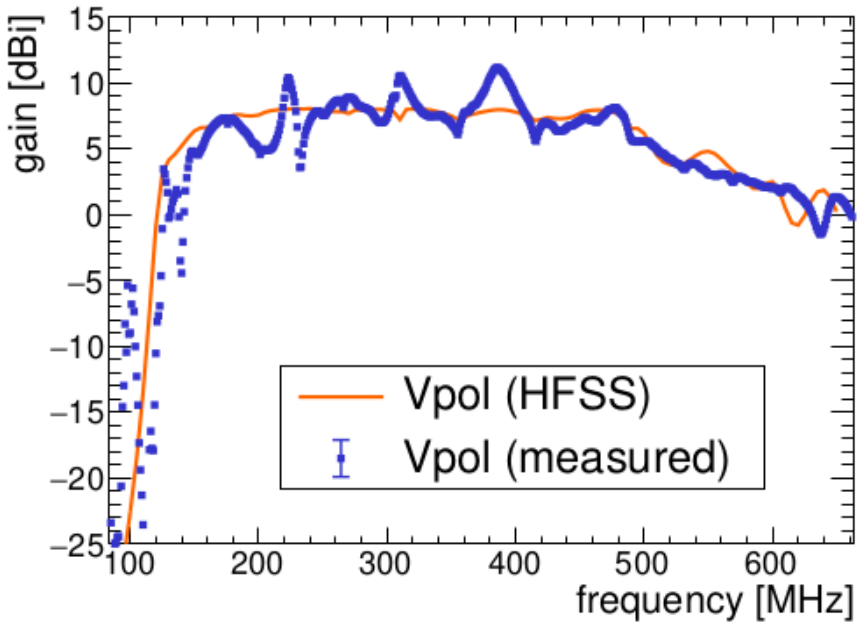

Figure 2.3: The measured realized gains (blue markers) and HFSS-simulated realized gains (orange curve) of the TAROGE-4 LPDA at boresight as a function of frequency.

resolution for event reconstruction using time-difference-of-arrival (TDOA) techniques.

The impulse response of the LPDA exhibits an anti-chirped characteristic, where higher frequencies ring earlier due to shorter dipoles positioned closer to the feed, resulting in reduced delay. Measurement results of the TAROGE-4 LPDA frequency response are compared with simulations conducted using High-Frequency Structure Simulator (HFSS) software, as shown in Fig. 2.3. The results generally align well, though a noticeable shift in the dips of the frequency response is observed[134].

2.3 Front-End Electronics Module

Each antenna polarization has its own dedicated signal chain, with the received signal fed into the RF FEE. The FEE includes a 180–350 MHz band-pass filter and a 63 dB gain LNA. After being processed by the FEE, the signal is sent to the DAQ system for further analysis.

doi:10.6342/NTU202500216

Figure 2.4: FEE modules of TAROGE, including filter and LNA.

The entire FEE module is housed in a weather-proof enclosure, which is installed near and directly behind the antennas to minimize receiver noise temperature and ensure optimal signal quality. The assembled TAROGE FEE modules are depicted in Fig. 2.4. These modules are connected to the DAQ system via long UV-resistant LMR-400 coaxial cables, ensuring durability and reliable signal transmission in outdoor environments.

2.3.1 Filters

The radio signal received by the antenna is initially passed through filters designed to suppress noise that could potentially saturate subsequent amplifiers or digitizers. To prevent narrowband RFI from saturating amplifiers or digitizers, bandpass filters are essential. These filters restrict the bandwidth of Galactic and thermal background signals, thereby increasing the signal-to-noise ratio (SNR). To achieve a low noise figure, it is important to minimize the insertion loss of RF components before the LNA. This involves reducing the length of coaxial cables and optimizing the insertion loss of the filters.

doi:10.6342/NTU202500216

The filters used in the system are constructed using high-Q factor surface-mounted device (SMD) capacitors and inductors, which offer low parasitic resistance, inductance, and capacitance. These SMD components are soldered onto a printed circuit board (PCB) that is enclosed in a brass box to provide EMI shielding, as shown in Fig. 2.4.

An elliptic filter design was selected for its steep transition between the passband and stopband, offering $\sim 40\ dB$ attenuation in the stopband while maintaining acceptable ripples in the passband. This design is particularly effective for suppressing narrowband RFIs, which are prevalent in suburban environments such as those encountered in Taiwan. The steep cutoff maximizes the usable bandwidth, which is critical for TAROGE stations. Although the design introduces some ripple in both the passband and stopband, these effects are tolerable once the receiver response is precisely measured. Additionally, the compact design of the filters, with fewer components, minimizes insertion loss due to the resistance of copper traces and SMD parts.

The TAROGE filter design was customized using Iowa Hills Filter Design software. This tool allows for the calculation of optimal commercially available components based on specific requirements, such as cutoff frequency and stopband attenuation. The filters are modularized and connected in series, with the low-pass and high-pass filters forming a bandpass filter that typically has an insertion loss of $\sim 1\ dB$. The lower cutoff frequency of the filter is typically determined by the frequencies of the strongest CW noise, while the upper cutoff frequency depends on the sampling rate or digitizer bandwidth. In cases of strong and persistent CW interference within the passband, additional notch filters is added to mitigate the interference effectively[134].

doi:10.6342/NTU202500216

2.3.2 Low Noise Amplifier Module

Weak radio signals from air showers, typically at microvolt (μV) levels, require amplification to millivolt (mV) levels to meet the dynamic range and resolution requirements of the triggering and sampling electronics. LNAs play a critical role in boosting the signal while preserving the SNR. The total gain of the LNA module is approximately $63\ dB$, with a low noise temperature of around $100\ K$($\sim 1\ dB$ noise figure). After this amplification stage, the noise introduced by subsequent receiver components becomes negligible.

The LNA module is enclosed within an EMI shielding box made of nickel-coated cast aluminum for effective electromagnetic interference protection. The enclosure includes a feedthrough capacitor for DC power, with the module consuming approximately $1.8\ W$at $12\ V$DC.

The customized first-stage LNA, referred to as the NTU LNA, provides $\sim 34\ dB$ gain and contributes most of the noise temperature in the frequency range of 50–1000 MHz. This LNA has been used in other high-profile experiments, such as ARA and ANITA-III and IV[12, 70]. Its power consumption is relatively low, remaining roughly constant at $31\ mA$ across a DC voltage range of 5–12 V, corresponding to 0.155–0.372 W (approximately $0.35\ W$ at $12\ V$).

The second-stage amplifier employs the commercial Mini-Circuits ZKL-2+, providing an additional $32\ dB$ gain. This stage has a higher power consumption of approximately $1.44\ W$. In the TAROGE-4 system, a $1\ dB$ RF power attenuator is inserted between the two amplification stages to minimize potential signal reflection in the transmission line, ensuring stable signal transmission and reducing potential mismatches.

doi:10.6342/NTU202500216

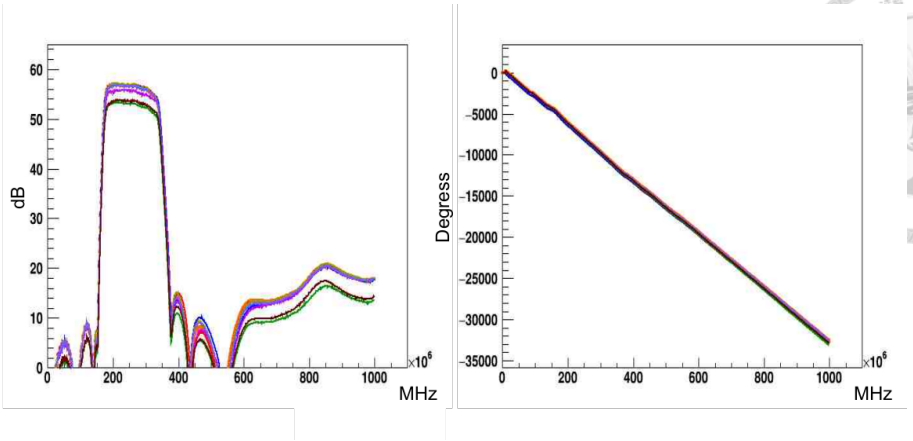

Figure 2.5: Gain (left) and phase shift (right) as functions of frequency for the TAROGE-4 FEE modules and cables, measured using a vector network analyzer. Two channels exhibit approximately 3 dB lower gain due to an additional combiner used to integrate a 100 MHz signal from the oscillator for synchronization between picoscopes.

2.3.3 Responses

The frequency responses of the FEE modules and cables, represented by the S-parameter, were measured using a vector network analyzer for subsequent signal deconvolution. The overall gain and phase shift as functions of frequency for the TAROGE-4 FEE modules and cables are shown in Figure 2.5.

2.4 Data Acquisition System

The DAQ system is central to TAROGE-4's operations, combining signal processing, data storage, and communication capabilities. It includes oscilloscopes for high-resolution digitization, a programmable trigger module, and a power management unit. The system's modular design allows for scalable performance and straightforward integration of upgrades.

doi:10.6342/NTU202500216

2.4.1 Hardware

The TAROGE-4 DAQ system (as shown in Fig. 2.6) primarily comprises four components: a trigger system for pulse detection, a digitization system for signal sampling, a power module for power management and scheduling, and a computer for overall control, data recording, and communication.

The trigger module is a critical component of the TAROGE system, responsible for initiating data acquisition by identifying signals of interest while suppressing background noise. This functionality is essential for achieving reliable detection of UHECRs and UHECNs, whose event rates are exceptionally low amidst significant environmental and thermal noise. This will be explained in detailed in next chapter.

TAROGE-4 utilized Picoscope 6403C oscilloscopes, each equipped with 8-bit analog-to-digital converters (ADCs) and a bandwidth of $350\ MHz$, capable of capturing detailed signal characteristics. These oscilloscopes were configured to sample at a period of 0.8 nanoseconds ($1.25 Gsample/s$), enabling high temporal resolution for detecting fast radio pulses. The time window for each event was extended to 1.2 microseconds, providing 1500 samples per waveform. This extended window was critical for capturing both direct and reflected signals from cosmic rays interacting with the ocean surface. TAROGE-4 operates with two data acquisition modes: block mode ("got-1-send-1") and rapid block mode ("got-N-send-N"). In block mode, events are read out individually as they are triggered, achieving a maximum event rate of approximately $44\ Hz$, with an average readout time of about 22.5 microseconds per event. This mode is suitable for scenarios requiring immediate data transfer. In contrast, rapid block mode leverages deep memory to store and read out up to 100 events simultaneously, boosting the event rate to approximately

doi:10.6342/NTU202500216

330 Hz. This configuration greatly enhances the system's ability to handle high trigger rates without data loss. Currently, TAROGE-4 operates in block mode, as the trigger system maintains a controlled trigger rate of around 10 Hz, making this mode sufficient for its operational needs.

Synchronization between Picoscopes is critical for precise event reconstruction based on TDOA between channels. Since the oscilloscopes operate independently without a shared external clock, trigger jitter with a typical root mean square (RMS) of 400 picoseconds can occur, potentially affecting directional accuracy. To mitigate this, a stable sinusoidal wave generated by a 100 MHz RF oscillator Crystek CPRO5-0100 is split and injected into one channel of each oscilloscope. By calibrating the phase differences between the injected signals, the trigger jitter can be corrected. This single-oscillator synchronization method maintaining a high timing resolution of a few picoseconds, ensuring reliable performance in the TAROGE-4 system.

The power system of TAROGE-4 is designed to ensure reliable operation in diverse environmental conditions while supporting the continuous functionality of all subsystems. It features a modularized power module responsible for power distribution, scheduling, and monitoring. Further details of this system will be introduced in the next section.

The main DAQ program runs continuously on an industrial-grade computer Hystou FMP04-1037U, which interfaces with the field-programmable gate array (FPGA) board, oscilloscopes and power board. The DAQ computer performs several critical tasks, including coordinating the operation of DAQ components, saving triggered events to a local solid-state drive (SSD), and transferring data back to the laboratory for further analysis. It also dynamically adjusts the trigger threshold to maintain a manageable event rate,

doi:10.6342/NTU202500216

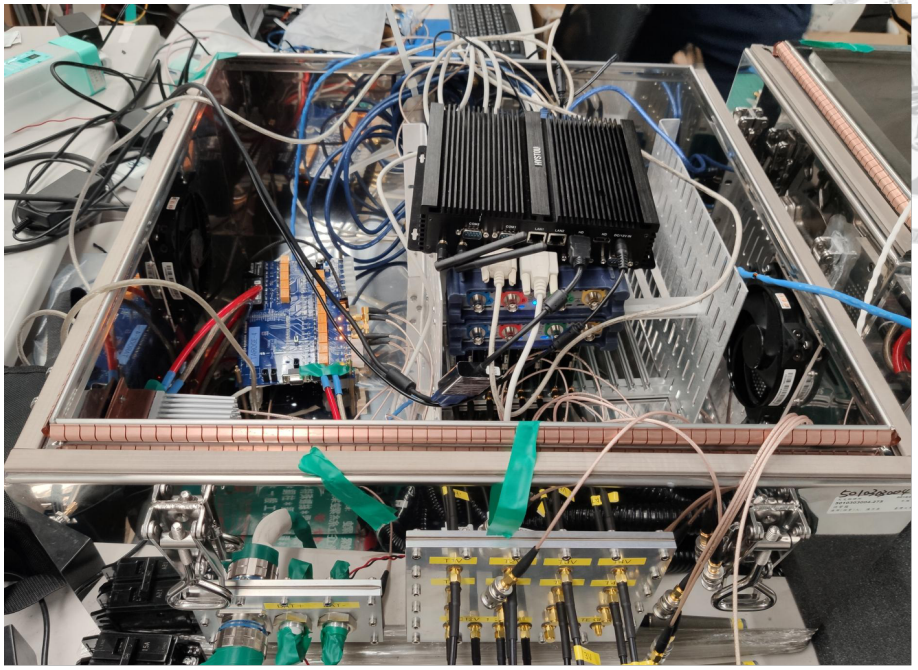

Figure 2.6: Photo of TAROGE-4 DAQ system before installation.

minimizing dead time during the readout process. Additionally, the DAQ computer communicates with the power module to monitor power system status and implement power management strategies when needed.

2.4.2 Program Algorithm

As shown in Fig. 2.7, the DAQ program workflow run with following steps:

- Initialization and Trigger Configuration: At the start of the DAQ process, the trigger rates for all channels and frequency bands are scanned as a function of trigger threshold to determine the optimal initial threshold value. The oscilloscopes are configured and set to standby mode, ready to detect trigger signals.

- Trigger Monitoring: The trigger module is unlocked to begin processing incoming triggers. Both the computer and oscilloscopes wait for trigger signals from the FPGA. If no trigger is received within a specified timeout window (5 seconds), the

doi:10.6342/NTU202500216

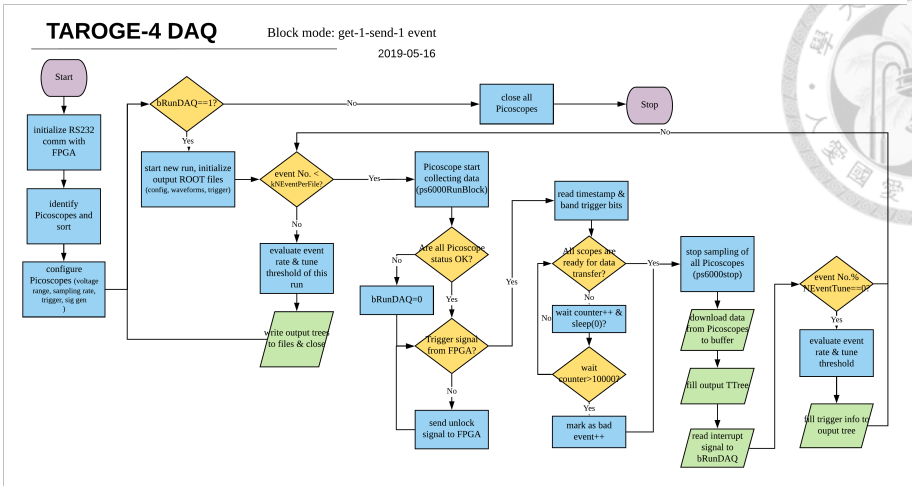

Figure 2.7: DAQ program in block mode.

computer sends a reset signal to the FPGA to address potential system hangs.

- Data Acquisition: Upon receiving a trigger signal, the trigger module is locked to prevent additional triggers during data acquisition. If the Picoscopes are operating in block mode, the computer requests the scopes to transfer sampled data immediately. If the Picoscopes are in rapid block mode, events are buffered on the scopes, and data is transferred only after 100 events have been recorded.

- Dynamic Trigger Adjustment: To maintain an optimal event rate between 5–$20\ Hz$, the trigger thresholds are dynamically adjusted every 100 events. This balances sensitivity and system performance while minimizing dead time.

- Data Storage: Every $10,000$ events are saved to disk in a ROOT file format, and the system starts a new data acquisition run to continue recording.

- System Monitoring and Looping: The system checks for any interruption signals, either from the user or the power control program. If an interruption signal is detected, the DAQ program halts. Otherwise, the program loops back to step 2 and continues the data acquisition cycle.

doi:10.6342/NTU202500216

2.5 Power System

The power system of TAROGE-4 is designed to provide reliable, autonomous operation in remote locations without access to grid power. Drawing from the experience of TAROGE-2 and TAROGE-3, the system combines renewable energy sources, advanced battery technology, and real-time monitoring and control mechanisms to ensure year-round functionality, even under challenging environmental conditions.

2.5.1 Photovoltaics Power Module

The core of TAROGE-4's power system is the solar power module, which includes several key components:

- Photovoltaic (PV) Panels: TAROGE-4 employs PV panels with a nominal power output of $1040\ W$, optimized for the system's power consumption of approximately $120\ W$. The panels are oriented southward and tilted by $\sim 25^{\circ}$ to align with the local latitude in Taiwan, maximizing solar energy absorption throughout the year. The PV panels operate at $\sim 10\%$ efficiency, converting sunlight into electrical power while being robust enough to withstand weather fluctuations.

- Deep-Cycle Battery Bank: The power generated by the PV panels is stored in a battery bank composed of sealed gel lead-acid deep-cycle batteries Ritar DG12-100. These batteries, with a capacity of $100\ Ah$ each, are arranged in a serial-parallel configuration to maintain a $48\ V$ operating voltage, reducing current and improving overall efficiency. This design ensures high capacity, charge balance, and long battery life. The battery bank provides consistent power during periods of

doi:10.6342/NTU202500216

low sunlight, such as during winter or cloudy weather.

- Charge Controller: The solar power system uses a maximum power point tracking (MPPT) charge controller (MorningStar TriStar TS-MPPT-60) to regulate the power flow between the PV panels and the battery bank. The MPPT controller maximizes power throughput and maintains efficiency even under variable weather conditions. It also monitors and communicates system status, including voltage and current readings, with the micro-controller for centralized power management. The controller consumes less than $3\ W$ and includes surge protection circuits to safeguard against power faults, such as lightning.

- Weatherproofing and EMI Shielding: To protect the power system from environmental factors and EMI, the charge controller is housed in an EMI shielded enclosure, which, along with the batteries and DAQ box, is placed inside a weatherproof housing. The stainless steel EMI shielded enclosure and DC feedthrough capacitors Schaffner FN7563-63 effectively minimize the risk of EMI contamination, ensuring the integrity of the data acquisition process.

2.5.2 Monitor and Control

The TAROGE-4 power system incorporates a robust monitoring and control framework to ensure reliability and flexibility in its autonomous operation. To protect the battery bank and extend its lifespan, the system monitors battery voltage closely. When the state of charge drops to 50–60%, the system automatically shuts down to prevent over-discharge. Once the state of charge rises to around 80%, the system reboots, maintaining a consistent power supply and prolonging battery health.

doi:10.6342/NTU202500216

Individual components, including amplifiers, the DAQ computer, oscilloscopes, and network routers, are managed using solid-state relays. This setup enables precise power control, allowing for remote power cycling of specific devices during maintenance or testing.

An Arduino Mega 2560 microcontroller communicates with the MPPT charge controller via RS232 using the Modbus protocol. It monitors real-time performance metrics, such as battery voltage, charge status, and internal temperatures. The system sends regular housekeeping reports for system monitoring and diagnosis, and generates alerts for any anomalies, such as low battery voltage or abnormal behaviors, prompting immediate user intervention.

doi:10.6342/NTU202500216

Chapter 3 TAROGE-4 Trigger System

The TAROGE-4 trigger system (as illustrated in Fig. 3.1) represents a sophisticated and highly adaptive framework designed to detect faint impulsive signals from EAS induced by UHECRs and UHECNs. Operating in a suburban environment, TAROGE-4 must contend with significant noise challenges, including anthropogenic interference and environmental variability. Despite these obstacles, the trigger system's innovative design ensures high sensitivity, precision, and robustness, enabling reliable detection of astrophysical signals.

The system incorporates advanced features such as dynamic noise suppression, multi-band frequency partitioning, and hierarchical triggering logic, which collectively enhance its efficiency and accuracy. With a modular architecture and FPGA-driven programmability, the trigger system is not only capable of real-time data processing but also highly scalable for future upgrades. This chapter details the components and operational principles of the TAROGE-4 trigger system, emphasizing its critical role in overcoming the unique challenges of detecting UHE particles in a noise-prone suburban setting.

Subsequent sections provide insights into the suburban noise environment, the innovative design of the trigger banding and hierarchical logic, the engineering behind the trigger boards, and the advanced FPGA programming that enables real-time adaptability.

doi:10.6342/NTU202500216

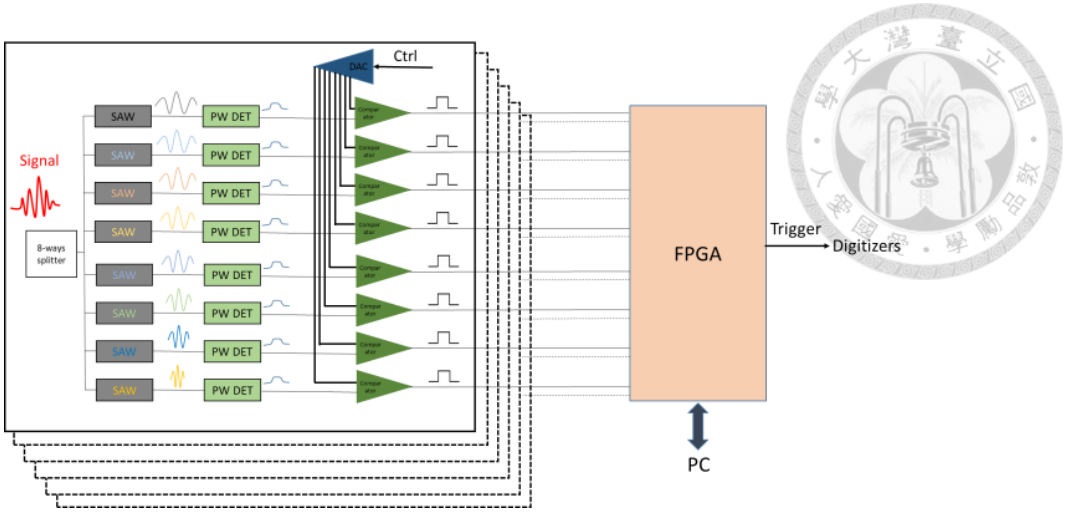

Figure 3.1: TAROGE-4 trigger system, including trigger boards and FPGA.

Together, these elements establish TAROGE-4 as a pioneering system for UHE particle detection, paving the way for future advancements in cosmic ray and neutrino astrophysics.

3.1 Suburban Environment

The TAROGE-4 station, situated in a suburban environment on the eastern coast of Taiwan, faces unique challenges due to the prevalence of anthropogenic noise sources. These include communication signals, radar emissions, and other continuous wave (CW) interferences. These noise sources significantly challenge the detection of faint impulsive signals generated by EAS. Despite these challenges, the TAROGE-4 site benefits from its geographical positioning, which enables a clear line of sight over the ocean, a natural reflector that enhances signal reception.

Addressing the suburban noise challenges is critical for preserving the integrity and sensitivity of the TAROGE-4 trigger system. To counteract these interferences, the trigger design incorporates advanced noise suppression strategies. These include dynamic thresholding, which adjusts detection thresholds in real-time to adapt to fluctuating noise levels, and multi-band coincidence logic, which enhances the reliability of detection by cross-

doi:10.6342/NTU202500216

verifying signals across multiple frequency bands. Together, these methods form a robust system capable of maintaining high detection accuracy in a noise-prone environment[40].

3.2 Trigger Banding

Trigger banding is a pivotal feature of the TAROGE-4 trigger system, designed to optimize the detection of EAS events while mitigating background noise. The full frequency band, spanning 180 MHz to 350 MHz, is partitioned into eight discrete sub-bands using surface acoustic wave (SAW) filters[99]. This segmentation allows for enhanced discrimination between impulsive radio signals and background noise. The responses of the band-pass SAW filters are shown in Fig. 3.3.

By isolating specific frequency ranges, the trigger system analyzes each sub-band independently for signal activity. This modular approach ensures that localized noise sources or narrowband interference, which might affect only one or a few sub-bands, do not compromise the overall trigger logic. Consequently, TAROGE-4 can maintain high detection efficiency in noisy environments (suburban coastal regions). Each sub-bands in TAROGE-4 has similar trigger efficiency against impulsive signal strength as shown in 3.2.

3.3 Design Logic

The TAROGE-4 trigger system implements a hierarchical approach to signal processing, utilizing three distinct levels of trigger logic to iteratively refine the selection of candidate events. This multi-tiered structure enhances the system's ability to identify true

doi:10.6342/NTU202500216

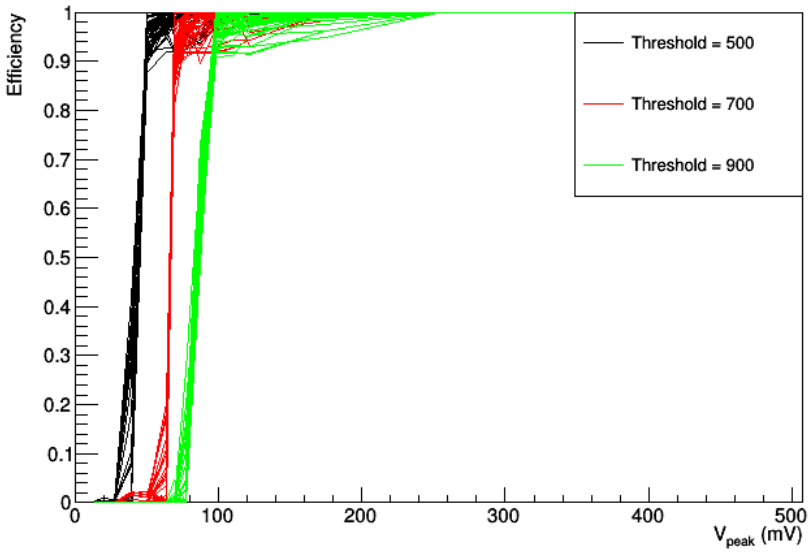

Figure 3.2: Trigger efficiency as a function of impulsive signal strength for different thresholds across all sub-bands in the TAROGE-4 trigger system.

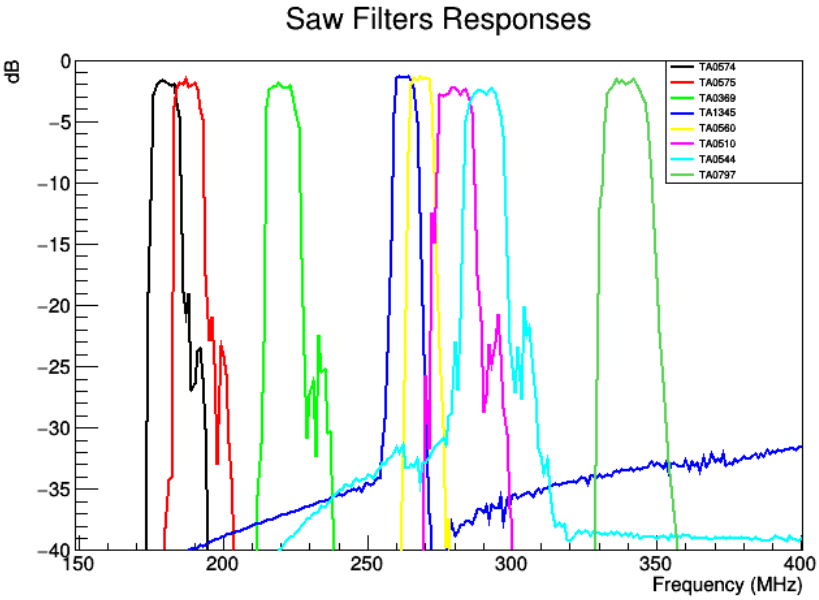

Figure 3.3: The responses of the band-pass SAW filters used in TAROGE-4 trigger system.

doi:10.6342/NTU202500216

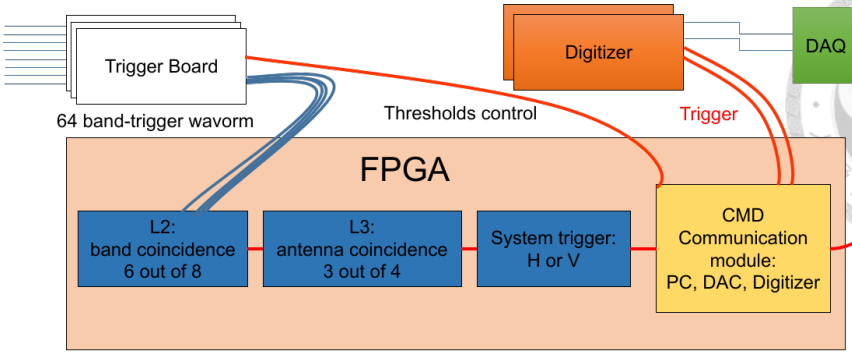

Figure 3.4: General design logic of the TAROGE-4 trigger system. The L1 trigger is implemented in analog hardware, while the L2, L3, and system triggers are implemented digitally within the FPGA. Additionally, a command line (CMD) communication module is integrated into the FPGA, enabling communication with the DAQ computer, sending trigger signals to digitizers, and controlling the threshold settings of the trigger board DAC.

EAS events while effectively filtering out noise and spurious signals. The modular design not only ensures scalability for future upgrades but also provides the flexibility needed to adapt to varying noise environments in suburban regions. Fig. 3.4 and Fig. 3.5 illustrate the FPGA design logic, detailing the implementation of the hierarchical trigger system and its key components.

3.3.1 Single Band L1 Trigger

The Level 1 (L1) trigger is a cornerstone of the TAROGE-4 trigger system, designed to efficiently process signals within individual frequency sub-bands. Each sub-band's output is continuously monitored for amplitude levels that surpass a dynamically set threshold, allowing the system to filter potential events based on their spectral intensity in real-time. This initial level of processing acts as a crucial preliminary filter, isolating candidate signals that exhibit characteristics consistent with EAS events as mention in 3.2. Operating with minimal latency, the L1 trigger ensures that all flagged signals are promptly forwarded for further analysis. Its rapid response capability is essential for capturing fleeting, high-energy signals in a noisy environment

doi:10.6342/NTU202500216

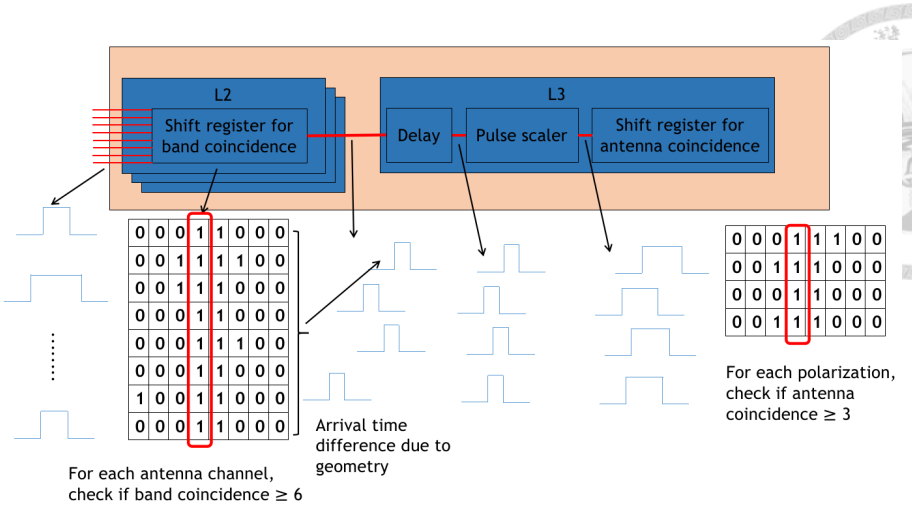

Figure 3.5: Detailed implementation of the hierarchical trigger system shown in Fig. 3.4. Shift registers are utilized to record trigger information and evaluate coincidences. A delay module is employed to adjust for time delays caused by antenna geometry, while a pulse scaler accounts for delays introduced by signals arriving from different paths. Together, the delay module and pulse scaler module ensure that the system only detects signals originating from TAROGE-4's FoV, significantly reducing the impact of noise from the northern town.

The L1 trigger is implemented on dedicated trigger boards, where sub-band outputs are processed and evaluated independently. These outputs are then forwarded to the FPGA board, which consolidates the data for higher-level triggering. This architecture not only ensures efficient processing of large data volumes but also supports scalability and adaptability for future system upgrades or operational adjustments. The L1 trigger thus serves as a robust and agile mechanism, laying the groundwork for reliable and precise impulse detection.

3.3.2 Multi-band L2 Trigger

The Level 2 (L2) trigger plays a pivotal role in refining the initial signal processing by integrating outputs from multiple sub-bands to detect coherent signals spanning the frequency spectrum. By applying advanced coincidence logic, the L2 trigger ensures that triggers in separate sub-bands occur simultaneously within a carefully calibrated temporal

doi:10.6342/NTU202500216

window, a condition characteristic of genuine EAS events.

This multi-band analysis offers a robust mechanism for mitigating false positives, which are often caused by localized noise or spurious signals confined to individual sub-bands. By requiring temporal and spectral consistency across multiple frequency channels, the L2 trigger filters out random, isolated noise, effectively enhancing the system's selectivity. This approach is particularly effective in identifying impulsive events, as UHECR-induced and UHECN-induced signals are expected to exhibit broad spectral signatures that manifest coherently across the sub-bands. The integration of data from multiple bands provides a high degree of confidence in distinguishing genuine astrophysical signals from environmental or anthropogenic interference. This capability is critical for maintaining the sensitivity of the TAROGE-4 system, ensuring it remains adept at detecting faint, transient signals amidst challenging noise environments.

3.3.3 Multi-antenna L3 Trigger

The Level 3 (L3) trigger in the TAROGE-4 system extends coincidence logic across multiple antennas, incorporating both spatial delay and temporal alignment to ensure detected signals originate from a consistent field of view (FoV) direction. By enforcing these criteria within a narrow coincidence window, the L3 trigger effectively filters out localized noise and transient interference that lack the coherent directional and temporal characteristics expected of UHECR-induced and UHECN-induced signals. Through a time-domain analysis of coincidences, the L3 trigger maintains robustness in complex noise environments while preserving sensitivity to faint, transient signals. This combination of spatial-temporal correlation significantly enhances the system's reliability and precision in identifying genuine EAS events.

doi:10.6342/NTU202500216

3.3.4 Global Trigger and Dynamic Threshold

The global trigger serves as the final decision-making stage in the TAROGE-4 trigger system, synthesizing inputs from all preceding levels to determine the validity of an event. This stage is equipped with a dynamic threshold mechanism that continuously adjusts band threshold values based on real-time noise conditions targeting on $5-20\ Hz$ global trigger rate. By adapting trigger criteria to the prevailing noise environment, the global trigger ensures optimal performance under varying conditions, balancing the competing demands of minimizing false positives and maximizing detection sensitivity.

The dynamic threshold mechanism operates through continuous monitoring of background noise levels, enabling real-time adjustments to the trigger thresholds. This approach effectively mitigates the impact of environmental fluctuations, such as intermittent anthropogenic interference or natural noise sources, which are common in suburban and coastal settings. The ability to dynamically respond to these variations allows the trigger system to maintain a consistent detection capability for faint, transient signals indicative of UHECR or UHECN events.

This adaptability is particularly critical for long-term operation in environments with variable and unpredictable noise profiles. By preventing the system from being overwhelmed by excessive false positives while ensuring high sensitivity to genuine events, the trigger system provides a robust and reliable framework for sustained data collection and analysis in challenging noise conditions.

doi:10.6342/NTU202500216

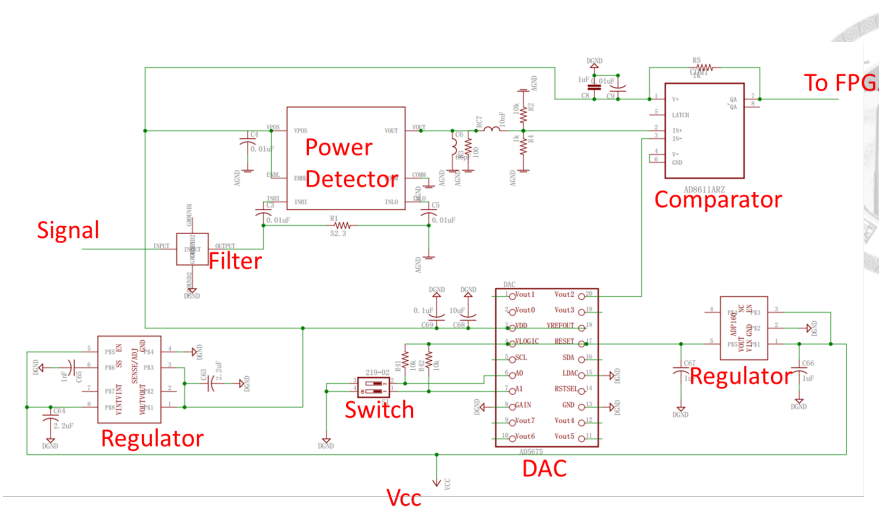

Figure 3.6: Schematic of a single channel of the trigger board, illustrating the components and signal processing workflow for efficient triggering. Figure adapted from [39].

3.4 Trigger Board Design

The trigger board for TAROGE-4 was meticulously designed using Eagle software[104], ensuring a robust and efficient architecture for signal processing. As illustrated in Fig. 3.6, the schematic of a single channel reveals the intricate layout, with the board containing a total of eight channels to handle multiple frequency bands simultaneously. Each channel's threshold is precisely controlled by a 16-bit digital-to-analog converter (DAC), the AD5675, which provides eight independent outputs for optimal flexibility and accuracy.

To ensure stable operation, the DAC' s logic is powered by a $1.8\ V$ output regulator (ADP160), while the other components of the board are powered by a $3.3\ V$ output regulator (DP7118). The inclusion of these on-board regulators plays a vital role in stabilizing the power supply and reducing noise, enhancing the overall performance and reliability of the system. Incoming signals are routed through an 8-way splitter before being divided into eight frequency bands, each of which processes the signal via a SAW filter, a power detector, and a comparator. The processed outputs from the comparators are transmitted to the FPGA via secure connectors and cables, ensuring seamless integration with higher-

doi:10.6342/NTU202500216

level logic.

The layout of the trigger board, depicted in Fig. 3.7, demonstrates careful attention to signal integrity. To prevent impedance mismatches, the trace width in the analog section is carefully matched to the pad dimensions. Furthermore, ground polygons are implemented on both sides of the board to minimize channel-to-channel interference, a critical design element in reducing cross-talk and preserving signal fidelity. The digital outputs from the comparators are strategically placed far from the sensitive analog circuitry to further reduce potential interference, maintaining the precision required for detecting faint EAS events.

In Fig. 3.8, the trigger board is showcased, highlighting its compact yet sophisticated design. Fig. 3.9 provides performance validation, with the red trace representing a cosmic ray-like impulse, the blue trace showing the power detector's output, and the green trace illustrating the comparator's output. These traces confirm the system's capability to effectively process signals and demonstrate the trigger board's ability to meet the stringent demands of the TAROGE-4 system.

3.5 FPGA Programming

The FPGA firmware serves as the core of TAROGE-4's trigger logic, executing L2 and L3 triggers along with the global trigger. This sophisticated programming is optimized for parallel processing, enabling the simultaneous analysis of signals from multiple frequency bands and antennas, a critical feature for maintaining high detection efficiency under varying environmental conditions.

Key Features of FPGA Programming include:

doi:10.6342/NTU202500216

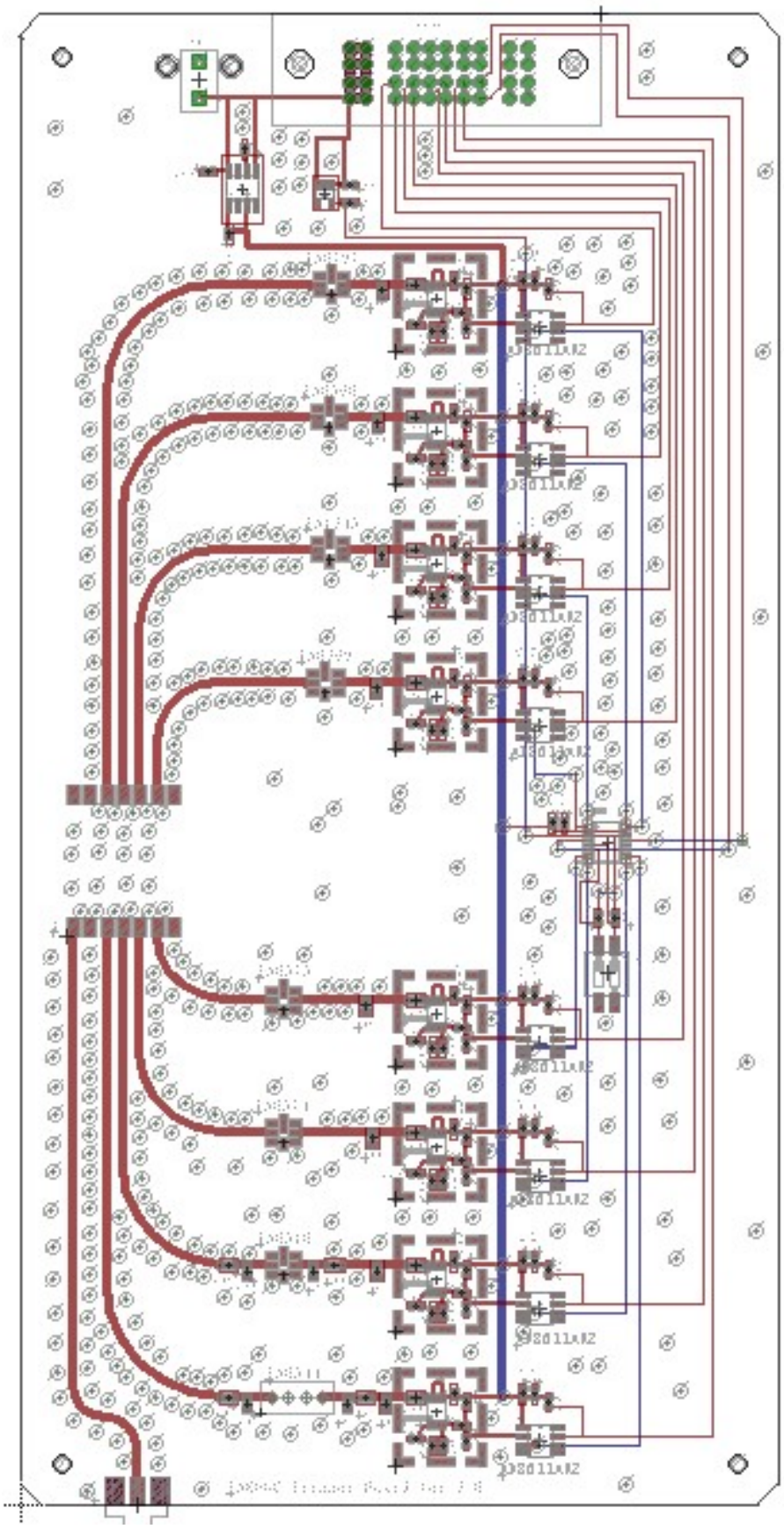

Figure 3.7: Layout of the trigger board, showcasing the arrangement of components and design optimizations for minimizing interference and ensuring efficient signal processing. Figure adapted from [39].

doi:10.6342/NTU202500216

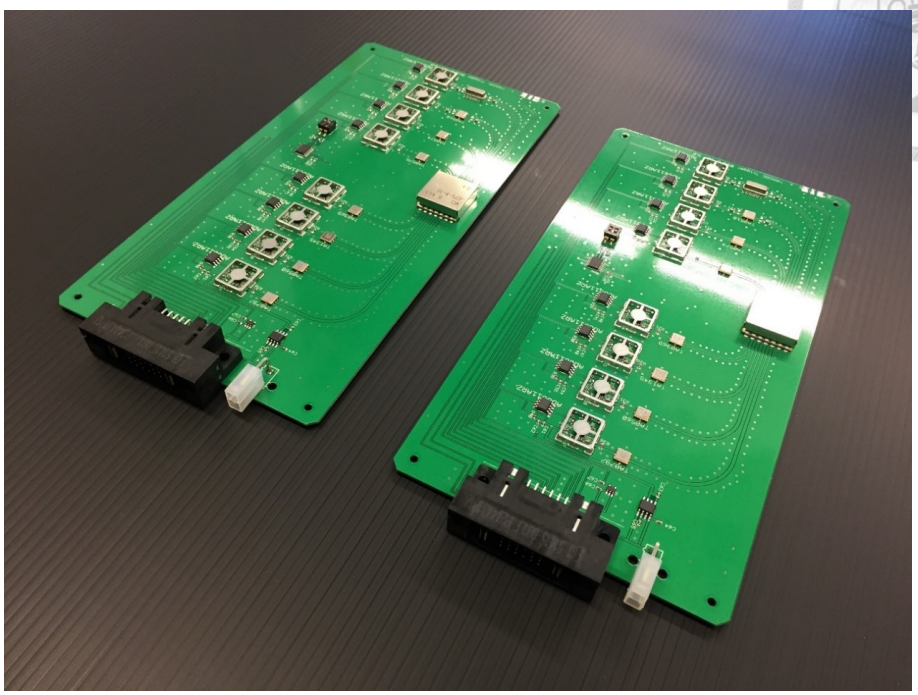

Figure 3.8: Produced trigger board, highlighting its compact yet sophisticated design, optimized for reliable and efficient signal processing in the TAROGE-4 trigger system. Figure adapted from [39].

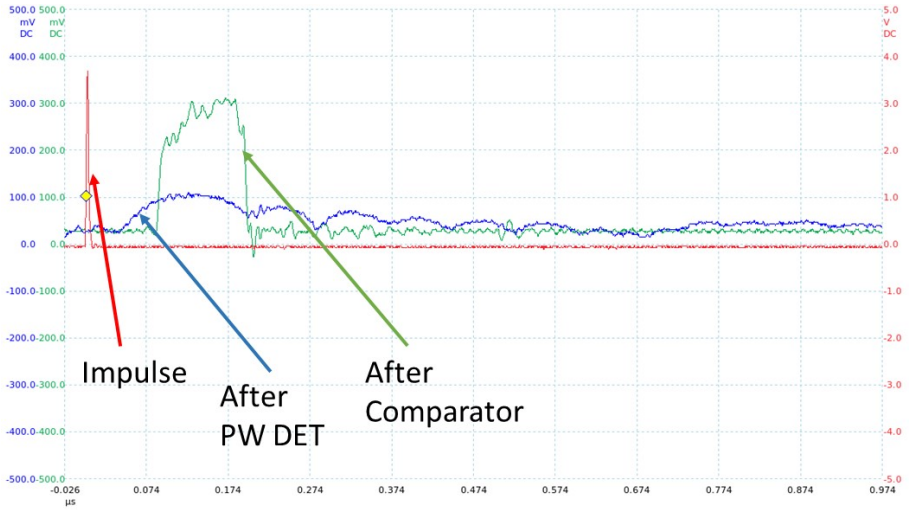

Figure 3.9: Simple testing of the trigger board. The red curve represents a cosmic ray-like impulse, the blue curve shows the output of the power detector, and the green curve represents the output of the comparator. The results confirm that the trigger board is functioning correctly. Figure adapted from [39].

doi:10.6342/NTU202500216

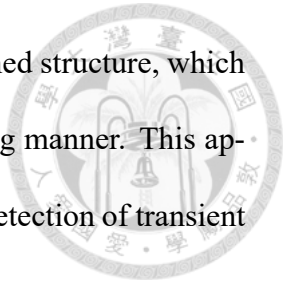

- Pipelined Architecture: The firmware is designed with a pipelined structure, which allows operations to be executed in a sequential but overlapping manner. This approach ensures low-latency processing, essential for real-time detection of transient signals.
- Real-Time Coincidence Logic: The trigger logic implements both temporal and spatial correlation, enabling the system to detect coherent signals across sub-bands and antennas. This feature is crucial for distinguishing genuine UHECR and UHECN events from spurious noise.
- Dynamic Reconfiguration: The firmware supports on-the-fly adjustments to trigger thresholds and logic parameters, responding dynamically to changes in environmental noise levels. This adaptability ensures optimal performance and minimizes false positives.

The FPGA firmware is developed in Verilog, a hardware description language (HDL) that provides precise control over the system's logic and architecture[124]. Extensive simulation and testing are conducted to validate the firmware under diverse operating conditions, ensuring its reliability and robustness.

Advanced debugging tools, such as logic analyzers and simulation frameworks, are employed during development to identify and resolve potential issues. These tools allow for in-depth analysis of the firmware's behavior, ensuring that it meets the stringent performance requirements of TAROGE-4. Before deployment, the firmware undergoes rigorous testing in both simulated and real-world environments to verify its functionality and reliability.

The combination of cutting-edge programming techniques, real-time adaptability,

doi:10.6342/NTU202500216

and thorough validation processes makes the FPGA firmware a critical component in the success of TAROGE-4's trigger system.

doi:10.6342/NTU202500216

Chapter 4 Event Angular Reconstruction and Calibration

Accurate angular reconstruction is a critical component of TAROGE-4's capability to identify and characterize UHECRs and UHECNs. This chapter outlines the methodologies employed to calibrate and refine angular measurements, focusing on overcoming challenges posed by reflections, systematic biases, and environmental noise.

By employing innovative approaches such as differential response unfolding and interferometric mapping, TAROGE-4 achieves precise angular resolution while minimizing systematic errors. A drone-borne pulser system provides essential calibration data, enabling detailed modeling of the system's differential response across the FoV. This system also serves as a validation tool, ensuring the reliability of angular reconstruction algorithms.

The comprehensive calibration and reconstruction framework detailed in this chapter allows TAROGE-4 to maintain sub-degree angular resolution under a variety of conditions, from near-horizon events to high-elevation angles. These advancements not only improve the precision of TAROGE-4's directional measurements but also lay a strong

doi:10.6342/NTU202500216

foundation for future upgrades and applications in the radio detection of high-energy astrophysical phenomena.

4.1 Differential Responses Unfolding

The angular reconstruction performance of TAROGE-4 is influenced by interference from both ground-reflected signals and reflections from nearby objects, in addition to direct signals. This issue is particularly pronounced for near-horizon events, introducing a bias of approximately 4°. Instead of directly deconvoluting the reflection response, we propose a new algorithm that maps and unfolds the differential response between channels, utilizing data from a drone-borne calibration system. Unlike deconvolution methods that attempt to eliminate reflection effects for each channel individually, this unfolding approach ensures that all channels experience an equivalent response. This novel method effectively alleviates interference effects while simultaneously calibrating out other system responses[40].

4.1.1 Algorithm

The received waveform consists of two components: the direct signal, which travels straight from the source to the receiver, and the reflected signal, which originates from interactions with the ground or nearby objects. These two components can interfere, introducing complexities in accurately interpreting the signal. The received waveform in an individual channel is modeled as:

$$W_i(f,\theta,\phi) = S(f) * P_i(f,\overrightarrow{r}) * R_i(f,\theta,\phi) * X_i(f,\theta,\phi) + N_i(f), \tag{4.1}$$

doi:10.6342/NTU202500216

where i denotes the channel label. $S(f)$ represents the source signal from the event, which contains the intrinsic characteristics of the physical phenomenon being observed. $P_i(f, \overrightarrow{r})$ is the phase change introduced during signal propagation from the event source to the receiver antenna's phase center. This phase term is influenced by the geometry of the source-receiver path and provides critical TDOA information necessary for direction reconstruction. $R_i(f, \theta, \phi)$ describes the response due to reflections, which depends on the angle of incidence, the nature of the reflecting surface, and the frequency of the signal. This term encapsulates the additional phase shifts and amplitude changes introduced by the reflection process. $X_i(f, \theta, \phi)$ represents the system response of the individual channel, including the antenna characteristics, signal conditioning components such as filters, and the amplification provided by the LNA. It incorporates the unique frequency-dependent behavior of the hardware. $N_i(f)$ accounts for the noise contributions from environmental and electronic sources, which can obscure the underlying signal. f means frequency, θ and ϕ are elevation angle and azimuth angle respectively, describing the direction of the incoming signal, $\overrightarrow{r}$ is event source coordinate.

The phase shift term $P_i(f, \overrightarrow{r})$is particularly crucial as it encodes the TDOA information required for angular reconstruction of the event's origin. However, accurately extracting $P_i(f, \overrightarrow{r})$ is challenging because it is entangled with the ground reflection term $R_i(f, \theta, \phi)$ and the system response term $X_i(f, \theta, \phi)$. These interdependencies necessitate sophisticated algorithms and calibration techniques to disentangle and compensate for the effects of reflections and hardware responses, ensuring reliable reconstruction of the event's direction and characteristics.

doi:10.6342/NTU202500216

The differential response between channels is defined as:

$$\alpha_{ij}(f,\theta,\phi) = \frac{R_i(f,\theta,\phi) * X_i(f,\theta,\phi)}{R_j(f,\theta,\phi) * X_j(f,\theta,\phi)}. \tag{4.2}$$

where α_{ij} represents the relative amplitude and phase response between channels i and j as functions of frequency f and angular coordinates (θ, ϕ). The terms $R_i(f,\theta,\phi)$ and $R_j(f,\theta,\phi)$ denote the ground reflection components for channels i and j, while $X_i(f,\theta,\phi)$ and $X_j(f,\theta,\phi)$ account for their respective system responses.

To derive α_{ij} with high precision, a drone-borne calibration pulser system is utilized and will be briefly introduced in next section[102]. This calibration system includes a solid-state impulse generator paired with a broad-band transmitter antenna, capable of emitting well-characterized signals over a wide frequency range. Additionally, the system is equipped with a differential GPS (D-GPS) module that provides centimeter-level positional accuracy, ensuring precise knowledge of the pulser's location at all times.

The drone-borne system can systematically scan the entire Field of View (FoV) of the array, allowing for detailed calibration across all angular coordinates. Each calibration pulser event's source coordinates, including elevation and azimuth, are logged with high accuracy using the GPS module. For a cal-pulser event originating from (θ, ϕ) direction, the differential response between channels can be defined as::

$$\alpha^m_{ij}(f,\theta,\phi) = \frac{W^m_i(f,\theta,\phi)}{W^m_j(f,\theta,\phi)} * \frac{P^m_j(f,\theta,\phi)}{P^m_i(f,\theta,\phi)} \approx \frac{R^m_i(f,\theta,\phi) * X^m_i(f,\theta,\phi)}{R^m_j(f,\theta,\phi) * X^m_j(f,\theta,\phi)} + O(N^m_i(f)) + O(N^m_j(f)), \tag{4.3}$$

where m is the label of cal-pulser event, $O(N^m_i(f))$ and $O(N^m_j(f))$ presents the noise terms and the relative propagation phase shift term $\frac{P^m_j(f,\theta,\phi)}{P^m_i(f,\theta,\phi)}$ can be computed with

doi:10.6342/NTU202500216

high precision by leveraging the known coordinates of the cal-pulser event. The use of a D-GPS system ensures accurate localization of the pulser, enabling the straightforward calculation of this term based on the geometry of the array and the source. By averaging $\alpha_{ij}^{m}(f,\theta,\phi)$ across multiple calibration pulser events, the noise terms $O(N_i^m(f))$ and $O(N_j^m(f))$ can be further suppressed due to their random nature. This averaging process allows the derivation of the differential response with higher accuracy, as given by::

$$\alpha_{ij}(f,\theta,\phi) \approx 1/M \sum_{m} \alpha_{ij}^{m}(f,\theta,\phi). \tag{4.4}$$

where M represents the total number of calibration pulser events included in the average. This averaging process effectively reduces the impact of random noise contributions, which average out to near zero over a sufficiently large number of events. As a result, the derived $\alpha_{ij}(f,\theta,\phi)$ provides a reliable representation of the underlying relative differential response between channels i and j for the given frequency f and angular coordinates (θ,ϕ). This step is crucial for accurate calibration of the system and the subsequent reconstruction of event directions.

For events requiring reconstruction, unfolding $\alpha_{ij}(f,\theta,\phi)$ on $W_j(f,\theta,\phi)$, the received waveform in channel j, yields:

$$W_j'(f,\theta,\phi) = \alpha_{ij} * W_j(f,\theta,\phi) = *S(f) * P_j(f,\overrightarrow{r}) * R_i(f,\theta,\phi) * X_i(f,\theta,\phi) + N_j(f), \tag{4.5}$$

where $W_j'(f,\theta,\phi)$ represents the unfolded waveform. The common systematic responses of $W_j'(f,\theta,\phi)$ and $W^{i(f,\theta,\phi)}$, such as the system response $X_i(f,\theta,\phi)$, and reflection effects $R_i(f,\theta,\phi)$, can be effectively canceled out through the cross-correlation pro-

doi:10.6342/NTU202500216

cess. By cross-correlating the unfolded waveforms $W'_j(f,\theta,\phi)$ and $W^{i(f,\theta,\phi)}$, the TDOA information can be accurately extracted. This TDOA information provides precise relative timing between channels, which is essential for applying an interferometric method to achieve accurate angular reconstruction. The interferometric approach leverages the phase and timing information across multiple channels to determine the event's direction with high resolution.

The challenge now lies in determining which differential response $\alpha_{ij}(f,\theta,\phi)$ should be selected for unfolding, as the event source direction (θ,ϕ) is not a known parameter but rather the target of reconstruction. To address this, a grid search method is employed across the FoV.

For each possible direction within the FoV, the unfolding process is applied using the corresponding hypothetical $\alpha_{ij}(f,\theta,\phi)$. This is followed by a cross-correlation for every antenna pair. The correlation coefficient, a measure of similarity between the unfolded waveforms, is calculated as a function of the hypothetical TDOA derived for each direction. The average correlation coefficient across all antenna pairs is then computed. If the hypothetical event source direction is correct and the unfolding process is accurate, the waveforms from different channels will align perfectly after cross-correlation, leading to an average correlation coefficient value close to 1. The reconstructed event direction is thus identified as the direction that yields the highest average correlation coefficient value.

4.1.2 Advantages

The differential response unfolding method for angular reconstruction in TAROGE-4 offers several distinct advantages that enhance both its accuracy and practicality. These

doi:10.6342/NTU202500216

benefits address key challenges in systematic error mitigation and operational efficiency, making the method a robust solution for precision event reconstruction.

Firstly, as a software-based solution, the unfolding method operates entirely at the analysis level, eliminating the need for hardware modifications. This approach not only reduces development time and resource expenditure but also allows for greater flexibility. The algorithm can be readily adapted or optimized to accommodate different operational environments, updated experimental configurations, or evolving scientific requirements, ensuring long-term applicability.

Secondly, the method significantly reduces systematic errors. Traditional deconvolution techniques often depend on complex terrain models or assumptions about electromagnetic ground properties, which can introduce biases due to environmental uncertainties. The unfolding method circumvents these assumptions by ensuring that all channels undergo consistent calibration, effectively neutralizing biases from unknown or variable environmental factors and improving reliability.

Moreover, the unfolding technique is largely insensitive to signal source characteristics, particularly the pulser spectrum $S(f)$. Unlike methods that require precise modeling of the source spectrum, the unfolding process remains robust against variations or uncertainties in the spectral properties of both calibration pulsers and detected events. This insensitivity ensures consistent performance across a wide range of conditions.

Another key strength of this method is its comprehensive system calibration. By integrating all relevant system responses, such as antenna characteristics, filters, and LNA, into the unfolding process, the method accounts for every component of the signal chain. This thorough calibration minimizes residual errors and enhances the reliability of angular

doi:10.6342/NTU202500216

reconstruction, ensuring precise directional information for detected events.

Finally, the method's scalability and applicability extend its utility beyond TAROGE-4. With minimal modifications, the algorithm can be implemented at other TAROGE stations or similar experiments, making it a versatile tool for future high-precision astroparticle physics projects. This adaptability, coupled with its ability to mitigate errors and improve accuracy, positions the differential response unfolding method as a critical innovation in the field of event reconstruction.

4.2 Interferometric Map

The interferometric map is a fundamental technique for reconstructing the direction of incoming radio signals, enabling precise determination of their origin. Widely utilized in experiments such as ANITA[103] and adapted for TAROGE-4, this method capitalizes on the time-domain coherence of RF signals received by multiple antennas in an array. By cross-correlating the signals from different antenna pairs and aligning them based on hypothesized source directions, the interferometric map highlights regions of maximum coherence, corresponding to the most probable direction of the source. This approach is particularly effective for detecting and localizing UHE particle events, as it combines the spatial and temporal information of the received signals. The interferometric map not only provides a precise angular resolution for event reconstruction but also enhances the ability to discriminate between genuine astrophysical events and background noise.

The interferometric map is constructed by summing the cross-correlation of voltage signals from antenna pairs for a hypothesized incoming wave direction (θ, ϕ). This process involves aligning the signals from each antenna pair by accounting for the time delay

doi:10.6342/NTU202500216

$\tau_{ij}(\theta, \phi)$, which is determined based on the relative positions of the antennas in the array and the assumed arrival direction of the wavefront. The time delay is calculated as:

$$\tau_{ij}(\theta, \phi) = \frac{\overrightarrow{r}_j - \overrightarrow{r}_i}{c} \cdot \hat{k}(\theta, \phi), \tag{4.6}$$

where: $\overrightarrow{r}_i$ and $\overrightarrow{r}_i$ are the positions vectors of antennas i and j in the array, c is the speed of light, $\hat{k}(\theta, \phi)$ is the unit vector pointing in the hypothesized direction of the incoming wave.

The cross-correlation $C_{ij}(\tau)$ between the signals received at antennas i and j quantifies the similarity of the voltage signals as a function of a time delay τ. It is defined as:

$$C_{ij}(\tau) = \int_{-\infty}^{+\infty} V_i(t) V_j(t - \tau) dt, \tag{4.7}$$

where $V_i(t)$ and $V_j(t)$ are the voltage signals received by antennas i and j, and τ represents the time delay applied to align the signals in time.

For each hypothesized direction (θ, ϕ), the signals are time-shifted by the calculated delay $\tau_{ij}(\theta, \phi)$, derived from the relative positions of the antennas and the assumed arrival direction of the wavefront. This alignment accounts for the propagation time differences due to the geometry of the array and the incoming wave's direction. The coherence of the signals is then evaluated by computing $C_{ij}(\tau)$ at $\tau = \tau_{ij}(\theta, \phi)$. By summing the cross-correlation values for all antenna pairs, the interferometric map reveals the direction of maximum coherence, corresponding to the most likely origin of the incoming wave. This method allows precise determination of the source direction while leveraging the spatial and temporal coherence of the detected signals.

doi:10.6342/NTU202500216

The cross-correlation $C_{ij}(\tau)$ between the signals at antennas i and j can also be computed in frequency domain as:

$$C_{ij}(\tau) = \int_{-\infty}^{\infty} \tilde{V}_i(f)\tilde{V}_j^*(f)e^{2\pi i f\tau}W(f)\,df, \tag{4.8}$$

where: $\tilde{V}_i(f)$ is the Fourier transform of $V_i(t)$, $W(f)$ is a windowing function applied to suppress frequencies outside the detection range.

The total interferometric coherence is obtained by summing the cross-correlations across all antenna pairs:

$$\mathcal{C}(\theta,\phi) = \sum_{i<j} C_{ij}(\tau_{ij}(\theta,\phi)), \tag{4.9}$$

where $\mathcal{C}(\theta,\phi)$ represents the level of coherence for the hypothesized direction (θ,ϕ). This summation is computed for all possible directions within the antenna array' s field of view, creating a 2D map of coherence. Peaks in the interferometric map correspond to the most probable directions of the incoming signal.

4.3 Drone-borne Pulser

The drone-borne pulser system (as shown in Fig. 4.1) is a compact and lightweight calibration tool tailored for high-precision radio observatories such as TAROGE. The system is designed to overcome the challenges posed by remote and inaccessible detector locations, providing an efficient method for in-situ calibration. Key components of the system include a high-power solid-state impulse generator, a programmable attenuator, a transmitting antenna, and a D-GPS module for precise positional tracking[102].

doi:10.6342/NTU202500216

The pulse generator produces radio signals within a frequency range of 180–450 MHz, tailored to match the operating frequencies of the TAROGE stations. These signals are transmitted through an omnidirectional antenna, enabling calibration across a wide angular field. The programmable attenuator adjusts the signal strength, ensuring compatibility with varying detector sensitivities. All electronic components are housed within a lightweight Faraday-shielded enclosure to minimize RFI during operation.

The D-GPS module, an integral component of the system, operates with a dual-band configuration. It enables simultaneous reception of signals from multiple global navigation satellite systems (GNSS), including GPS, GLONASS, GALILEO, and Beidou, thereby enhancing positional accuracy. The module records raw carrier phase signals, which are processed offline to achieve centimeter-level precision. This high accuracy is crucial for timing calibration and angular reconstruction of detector responses. The entire system weighs approximately 1.3 kg, making it compatible with commercially available drones. The lightweight design and modular construction ensure flexibility and ease of deployment, even in extreme environments.

In addition to its core calibration functionality, the drone-borne pulser system supports aerial photogrammetry through its built-in camera and GPS. This feature enables rapid and accurate 3D mapping of antenna arrays, further enhancing the utility of the system for deployment in high-altitude and polar research stations. The system's innovative design and modular features make it a versatile tool for advancing radio detection techniques in UHECR ray and UHECN research.

doi:10.6342/NTU202500216

Figure 4.1: Drone-borne pulser system consisting of a high-power impulse generator, a programmable attenuator, a transmitting antenna, and a D-GPS module. This system enables precise calibration of TAROGE-4 by providing well-characterized signals across a wide frequency range and ensuring accurate positional tracking with centimeter-level precision.

4.3.1 Pulser Event Identification

Pulser event identification is primarily achieved through timestamp matching and template matching methods. These techniques rely on precise synchronization between the transmitted pulses and the radio observatories' receivers. Timestamp matching involves comparing the recorded arrival times of pulses with the expected timing information from the D-GPS, ensuring alignment within sub-millisecond precision. Template matching, on the other hand, cross-references the received pulse waveforms with predefined signal templates to identify calibration events, accounting for potential distortions from environmental interference.

doi:10.6342/NTU202500216

4.3.2 Flight Summary

The drone-borne pulser system provides a comprehensive dataset of pulser signals across the FoV. A total of 39 flights for H-pol pulsers and 38 flights for V-pol pulsers were conducted, each lasting approximately 15 minutes. The flights followed inclined paths at an approximate distance of 700 meters from the station. The pulse rate was set to 5 Hz, ensuring consistent signal generation throughout the campaign.

For calibration, the collected templates served to derive the differential response $\alpha_{ij}(f, \theta, \phi)$, crucial for angular reconstruction. Around $500,000$ H-pol and $500,000$V-pol templates were collected for angles within $\pm 6°$ in elevation, while approximately $320,000$ templates were gathered for both H-pol and V-pol signals at elevation angles greater than $6°$. This comprehensive dataset ensures reliable modeling of the system's differential response across different directions.

For validation purposes, the dataset included around $75,000$ H-pol and $60,000$ V-pol signals for elevation angles within $\pm 6°$, and approximately $22,000$ H-pol and $18,000$ V-pol signals for elevation angles exceeding $6°$. These signals were instrumental in testing and confirming the accuracy of the angular reconstruction, providing a high degree of confidence in the performance of the TAROGE-4 array.

4.4 Angular Resolution

For elevation angles greater than $6°$, Fig. 4.2 illustrates the flight track (black curve) and the reconstructed direction of pulsers (red circles) for H-pol signals. The H-pol signals achieve an angular resolution of $0.12°$ in azimuth and $0.27°$ in elevation, as shown in Fig.

doi:10.6342/NTU202500216

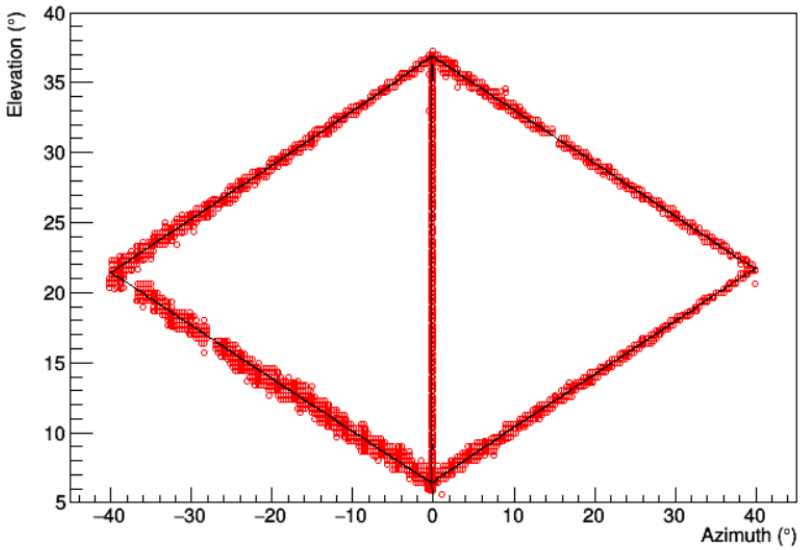

Figure 4.2: Flight track (black curve) and the reconstructed direction of pulsers (red circles) for H-pol signals with elevation angles greater than $6°$.

4.3. Similarly, Fig. 4.4 shows the flight track (black curve) and the reconstructed direction of pulsers (red circles) for V-pol signals, which achieve an angular resolution of $0.10°$ in azimuth and $0.24°$ in elevation, as depicted in Fig. 4.5.

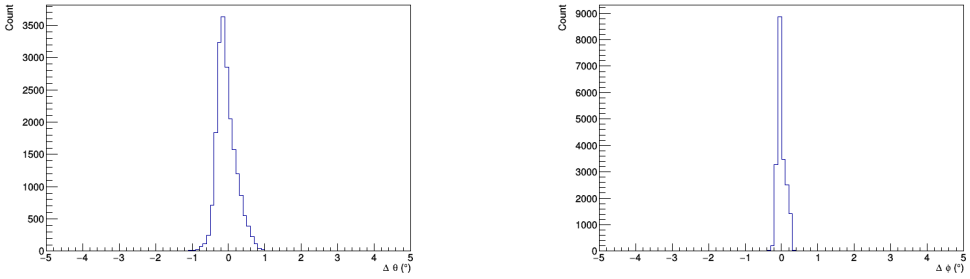

Figure 4.3: The H-pol signals with elevation angles greater than $6°$ achieve an angular resolution of $0.27°$ in elevation (left) and $0.12°$ in azimuth (right).

For elevation angles within $\pm 6°$, Fig. 4.6 illustrates the flight track (black curve) and the reconstructed direction of pulsers (red circles) for H-pol signals. The H-pol signals achieve an angular resolution of $0.24°$ in azimuth and $0.92°$ in elevation, as shown in Fig. 4.7. Similarly, Fig. 4.8 shows the flight track (black curve) and the reconstructed direction of pulsers (red circles) for V-pol signals, which achieve an angular resolution of $0.23°$ in azimuth and $0.86°$ in elevation, as depicted in Fig. 4.9.

doi:10.6342/NTU202500216

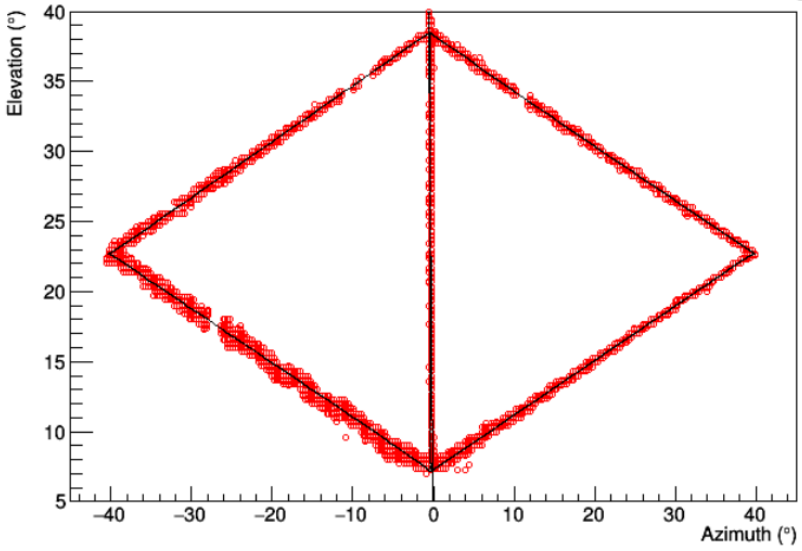

Figure 4.4: Flight track (black curve) and the reconstructed direction of pulsers (red circles) for V-pol signals with elevation angles greater than $6°$.

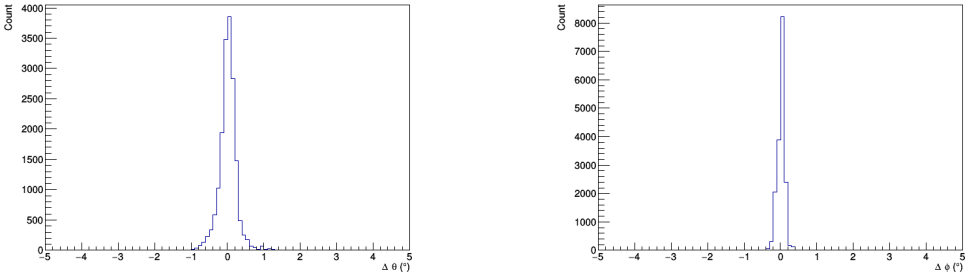

Figure 4.5: The V-pol signals with elevation angles greater than $6°$ achieve an angular resolution of $0.24°$ in elevation (left) and $0.10°$ in azimuth (right).

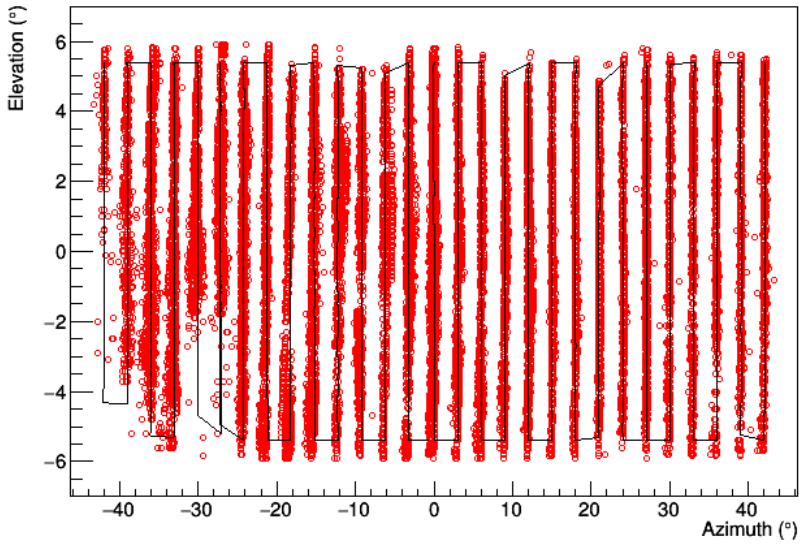

Figure 4.6: Flight track (black curve) and the reconstructed direction of pulsers (red circles) for H-pol signals with elevation angles within $\pm 6°$.

doi:10.6342/NTU202500216

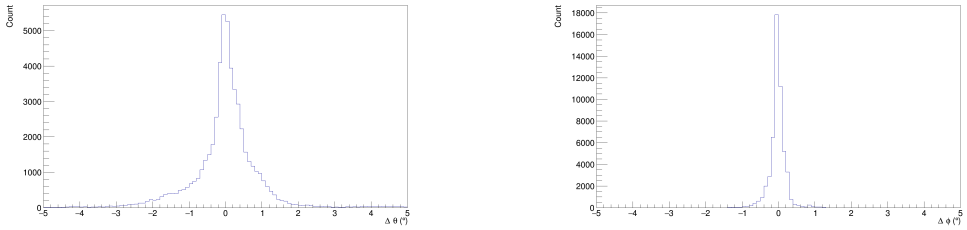

Figure 4.7: The H-pol signals with elevation angles within $\pm 6^\circ$ achieve an angular resolution of 0.92° in elevation (left) and 0.24° in azimuth (right).

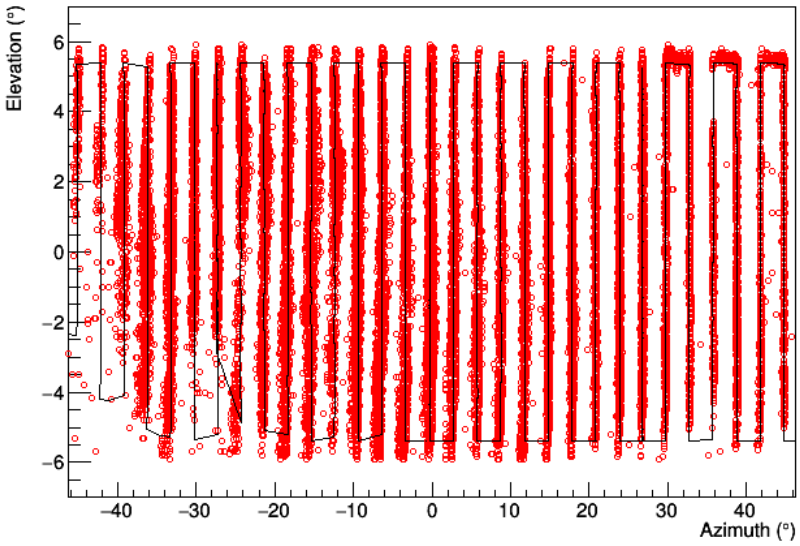

Figure 4.8: Flight track (black curve) and the reconstructed direction of pulsers (red circles) for V-pol signals with elevation angles within $\pm 6^\circ$.

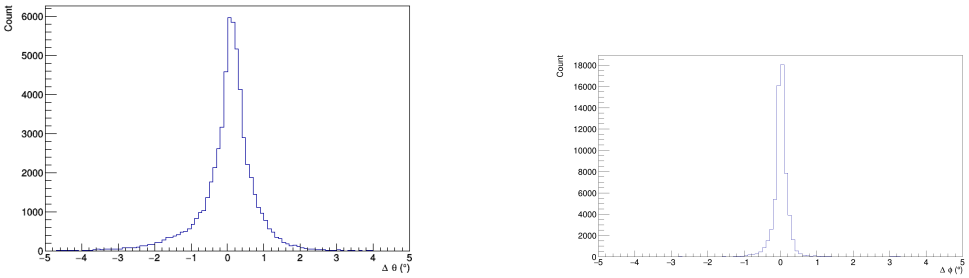

Figure 4.9: The V-pol signals with elevation angles within $\pm 6^\circ$ achieve an angular resolution of 0.86° in elevation (left) and 0.23° in azimuth (right).

doi:10.6342/NTU202500216

Fig. 4.10 presents the angular resolution as a function of SNR for combined H-pol and V-pol signals within elevation angles of $\pm 6°$. As the SNR decreases, angular resolution in both azimuth and elevation deteriorates, highlighting the dependence of accuracy on signal quality. Similarly, Fig. 4.11 illustrates the angular resolution as a function of elevation angle. The resolution in both azimuth and elevation degrades as the elevation angle approaches the horizon, where detection becomes inherently more challenging. Near the horizon of TAROGE-4, which is approximately $-0.85°$, the system achieves sub-degree resolution, even under these more demanding conditions. This performance underscores the system's capability to deliver precise angular measurements across its field of view, enabling reliable event reconstruction.

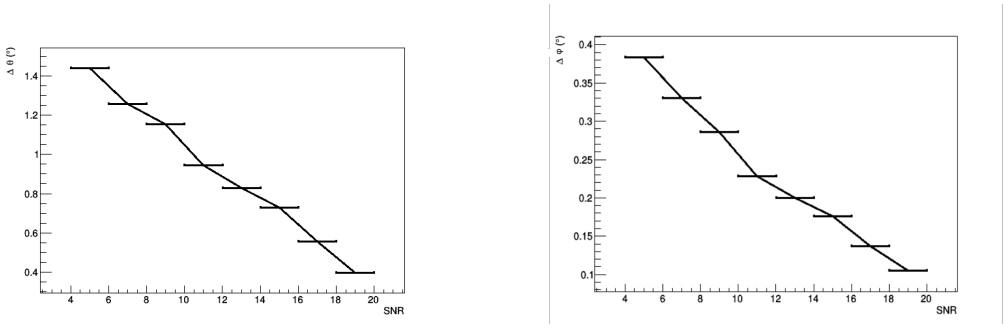

Figure 4.10: Angular resolution as a function of SNR for combined H-pol and V-pol signals within elevation angles of $\pm 6°$. The angular resolution in both elevation (left) and azimuth (right) deteriorates as the SNR decreases.

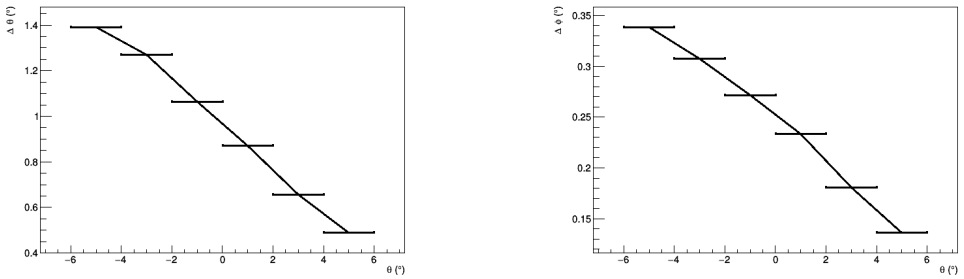

Figure 4.11: Angular resolution as a function of elevation angle for combined H-pol and V-pol signals within elevation angles of $\pm 6°$. The angular resolution in both elevation (left) and azimuth (right) deteriorates as the elevation angle decreases.

doi:10.6342/NTU202500216

doi:10.6342/NTU202500216

Chapter 5 UHECR Detection Simulation

A comprehensive Monte Carlo simulation framework was meticulously developed to model the detection of UHECRs and predict the corresponding radio signals generated by extensive air showers. This framework is indispensable for a variety of applications, including the creation of precise radio signal templates for event searches within TAROGE-4 data, detailed characterization of cosmic ray candidate events, and robust estimation of cosmic ray acceptance and flux measurements.

The simulation begins with the generation of UHECR-induced air showers using advanced air shower modeling tools like CORSIKA, integrated with CoREAS to simulate radio emission[83]. These tools accurately account for the geomagnetic deflection of electrons and positrons in the shower, as well as the Askaryan effect, which arises from charge imbalances. The resulting radio signals are modeled with high fidelity, taking into consideration realistic atmospheric density profiles, geomagnetic field strength, and local environmental conditions to ensure accurate representations of signal generation and propagation.

The simulation also models the interactions of radio waves with the TAROGE-4 antenna array, incorporating its specific design parameters, such as antenna frequency re-

doi:10.6342/NTU202500216

sponse and spatial orientation. This ensures that the simulated signals closely mimic those detected by the physical system. Furthermore, the framework integrates the TAROGE-4 trigger system, allowing researchers to study the effects of trigger thresholds and system efficiencies on event detection. By simulating the energy and angular distributions of detected events, the framework provides a detailed understanding of the detector's performance across a wide range of scenarios. This includes evaluating detection efficiency, estimating energy thresholds, and exploring the effects of event geometry on signal reconstruction.

The Monte Carlo simulation framework is not only a vital tool for interpreting observed data but also for optimizing the design and operation of TAROGE-4. By offering insights into the detector's sensitivity and response, it lays the foundation for the accurate identification of UHECR events and enhances the scientific output of the observatory.

5.1 Generation of Radio Signal

The generation of radio signals for TAROGE-4 involves a multi-faceted approach that combines sophisticated simulations of UHECR air showers, precise modeling of radio emissions, and the incorporation of detailed receiver responses. These steps are essential for creating realistic waveforms that represent the signals expected at the TAROGE-4 site, ensuring accuracy in event reconstruction, energy estimation, and system calibration.

5.1.1 UHECR Air Shower Simulation

The simulation of UHECR air showers was conducted using the well-established CORSIKA (COsmic Ray SImulations for KAscade) simulation package[75]. This pack-

doi:10.6342/NTU202500216

age employs the QGSJET-II-04 model for high-energy hadronic interactions, the GHEISHA model for low-energy hadronic interactions, and EGS4 for detailed electromagnetic EM cascade simulations, ensuring a comprehensive modeling of particle interactions across a wide energy range. To optimize computational efficiency, the thinning algorithm was applied when particle energies fell below thresholds of 10^{-6} and 10^{-8} of the primary energy for electromagnetic and hadronic particles, respectively. Additionally, a kinetic energy cutoff was set at $0.3\ GeV$ for hadrons and muons and $0.401\ MeV$ for electrons and photons, striking a balance between computational feasibility and simulation accuracy.

The simulations were conducted for two primary particle types: protons and iron nuclei. Protons, as lighter particles, penetrate deeper into the atmosphere and produce broader distributions of the shower maximum (X_max), while heavier nuclei like iron exhibit shallower atmospheric penetration and narrower X_max distributions. This distinction allows the simulation to capture the diversity in air shower characteristics resulting from different primary particles. Primary particle energies were sampled within the range of $10^{17.25}eV$ to $10^{19.5}$, covering the relevant energy spectrum for UHECR observations. The showers were simulated across all azimuth angles and zenith angles within the TAROGE-4 detector's field of view, ensuring comprehensive coverage of possible event geometries.

A total of $4,427$ air showers were simulated for each primary particle type (protons and iron nuclei), resulting in a combined dataset of $8,854$ showers. This extensive dataset provides a statistically robust foundation for studying the propagation and detection of UHECR-induced radio signals. By capturing the full range of physical and geometric variations, the simulations enable the development of precise radio signal templates for use in event reconstruction and flux estimation.

doi:10.6342/NTU202500216

5.1.2 Radio Emission from Air Showers

The CoREAS module, integrated with CORSIKA, calculates radio emissions from extensive air showers using a microscopic approach based on the Liénard-Wiechert potentials of point charges. The simulation employs the endpoint formalism, which focuses on the instantaneous acceleration and deceleration of charged particles, particularly electrons and positrons, at the endpoints of their tracks. This approach ensures that the electric field contributions from individual charged particle trajectories are precisely computed, capturing the subtle dynamics of radio wave production during the air shower's evolution. CoREAS aggregates the contributions of all particle tracks in the shower, combining them to model the resultant radio emission. This detailed and physically grounded method accounts for the complex interplay of geomagnetic and charge excess effects, ensuring that the simulated radio signals accurately reflect the underlying physics of UHECR-induced air showers.

To simulate radio emissions for TAROGE-4, predefined sampling locations were arranged in a star-shaped array, inspired by configurations used in experiments such as ARIANNA and TAROGE-M[25, 135]. This array consists of eight equiangular arms on the horizontal plane, derived by projecting the shower plane—orthogonal to the air shower axis—onto the observation plane. Two of the arms are aligned with the $\vec{v} \times \vec{B}$ axis, where $\vec{v}$ represents the velocity of the air shower axis and $\vec{B}$ is the geomagnetic field vector. This alignment ensures the accurate capture of the dominant geomagnetic emission component, which arises from the deflection of charged particles in the Earth's magnetic field.

The arms include 15 sampling points strategically distributed around the Cherenkov

doi:10.6342/NTU202500216

ring. A denser distribution of 10 points is placed near the Cherenkov ring, where the intensity of radiation is highest, while additional points sample regions inside and outside the Cherenkov ring to capture the full lateral radiation profile. This configuration provides a detailed representation of the asymmetric lateral distribution of radio signals, accounting for both the intensity peak and the signal's spatial extent. At each sampling location, waveforms for the three orthogonal components of the electric field vector were recorded with a temporal resolution of $0.1\ ns$, allowing for precise characterization of rapid signal variations such as those near the Cherenkov peak. The observation plane was positioned at an altitude of $700\ m$ to match the TAROGE-4 site, ensuring that the local atmospheric density and geomagnetic field conditions were accurately reflected in the simulation. Fig. 5.1 presents a 2D map illustrating the signal strength received at a 700 m altitude (by the TAROGE-4 station) for a $10^{18.5}$ eV proton-initiated air shower arriving from a zenith angle of $70°$ (left). The right panel shows the waveforms of the electric fields sampled at points along the arm aligned with the $\overrightarrow{v} \times \overrightarrow{B}$ axis. Fig. 5.2 presents the Fourier transform of the waveforms shown in Fig. 5.1. The red line represents the best linear fit of the logarithmic amplitude spectrum within the frequency range of 180–350 MHz.

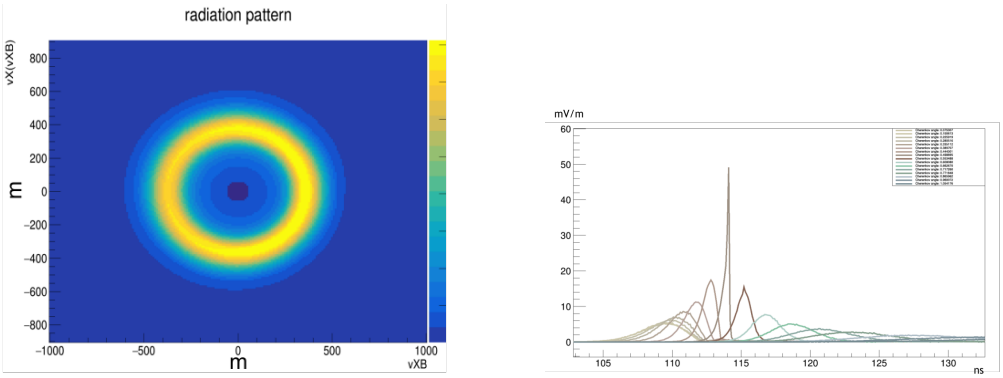

Figure 5.1: Left: 2D map illustrating the signal strength received at a 700 m altitude (by the TAROGE-4 station) for a $10^{18.5}$ eV proton-initiated air shower arriving from a zenith angle of $70°$. Right: the waveforms of the electric fields sampled at points along the arm aligned with the $\overrightarrow{v} \times \overrightarrow{B}$ axis.

doi:10.6342/NTU202500216

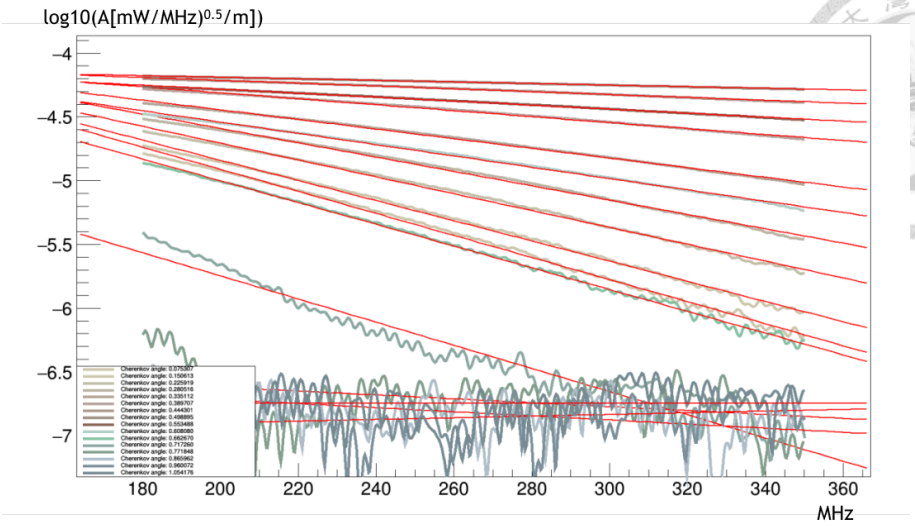

Figure 5.2: Fourier transform of the waveforms shown in Fig. 5.1. The red line represents the best linear fit of the logarithmic amplitude spectrum within the frequency range of 180–350 MHz.

5.1.3 Receiver Response Convolution

The expected voltage waveforms received by the TAROGE-4 digitization and trigger modules were generated by convolving the simulated electric field vectors, $\vec{E}(f)$, obtained from CoREAS, with the frequency-domain responses of the antenna and FEE. This process incorporates the full characteristics of the TAROGE-4 hardware, including the antenna response derived from HFSS modeling, the calibrated response of the FEE, the attenuation and phase shifts introduced by approximately 20 meters of coaxial cables connecting the FEE to the DAQ, and the splitters inside the DAQ.

The convolution was performed in the frequency domain using the convolution theorem, which simplifies the calculation of the received voltage by treating the convolution as a multiplication. The process is mathematically expressed as:

$$V(f) = \vec{E}(f) \cdot \vec{H}_{eff}(f) G_{FEE}(f) = \left[E_\theta(f) H_{eff,\theta}(f) + E_\phi(f) H_{eff,\phi}(f)\right] G_{FEE}(f) \tag{5.1}$$

doi:10.6342/NTU202500216

where: $V(f)$ represents the received voltage in the frequency domain. $\vec{E}(f)$ is the electric field vector simulated by CoREAS, with components $E_\theta(f)$ and $E_\phi(f)$ corresponding to the polar and azimuthal field components, respectively. $\vec{H}_{eff}(f)$ is the vector effective length (VEL) of the antenna, which encapsulates impedance mismatch, directional characteristics, and polarization effects. It is also frequency-dependent, capturing the antenna's sensitivity across different frequencies. $G_{FEE}(f)$ is the end-to-end gain of the system, accounting for the combined response of filters, amplifiers, coaxial cables, and the splitter network.

Each of these quantities is complex, comprising both amplitude and phase information. This ensures that the phase shifts introduced by the hardware components are accurately accounted for, preserving the temporal structure of the received signals. By transforming the convolved results back into the time domain, the simulation produces realistic voltage waveforms as they would be observed at the input of the TAROGE-4 digitization and trigger modules.

This approach enables precise modeling of the detector response, providing a realistic representation of how UHECR-induced radio signals propagate through the TAROGE-4 system. Such detailed modeling is essential for reliable event energy estimation, trigger performance evaluation, and calibration of the overall system response.

5.2 Trigger Simulation

The trigger simulation is a critical component of the detection process, facilitating detailed comparisons with measurements and playing a pivotal role in deriving cosmic ray fluxes. By combining detailed modeling of the trigger system with real-world noise data

doi:10.6342/NTU202500216

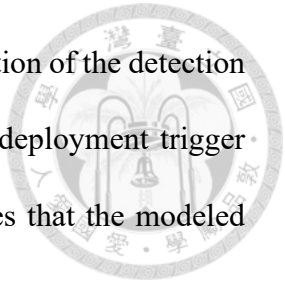

and Monte Carlo simulations, this framework enables accurate evaluation of the detection efficiency and effective area of the station. The integration of pre-deployment trigger efficiency measurements and FPGA logic into the simulation ensures that the modeled system closely mirrors its real-world counterpart.

The subsequent subsections delve into the modeling of band-specific trigger efficiencies, the simulation of the full trigger system, and the verification of these models using a drone-borne pulser system. By incorporating these components, the trigger simulation framework provides a comprehensive tool for assessing and refining the TAROGE-4 trigger system's capabilities under realistic operating conditions.

5.2.1 Band Trigger Efficiency Modeling

The trigger efficiency for each frequency band, as a function of input power and threshold, was meticulously characterized for all eight trigger boards before the deployment of TAROGE-4 as illustrated in Fig. 3.2. These measurements were essential to calibrate the trigger system, ensuring that the thresholds were appropriately tuned for reliable operation under real-world conditions. The efficiency curves, derived from these measurements, serve as critical inputs to the simulation framework, enabling the precise modeling of the trigger system's behavior.

5.2.2 Trigger System Simulation

The received signal at the TAROGE-4 station consists of two primary components: the UHECR event impulse and the noise background. To realistically simulate the input signal environment, the modeled UHECR signals were combined with real minimum-bias

doi:10.6342/NTU202500216

noise data collected from the TAROGE-4 station. This combination was performed in the time domain, preserving the temporal characteristics and variability inherent in the noise and the UHECR signals.

The TAROGE-4 trigger system processes signals from each antenna through an 8-way splitter, dividing the input into eight frequency bands. Each band is filtered using a SAW filter to isolate its frequency range, after which the signal power is detected. To replicate this process, the simulation convolves the input signals with the bandpass filter response, generating the waveforms corresponding to each frequency band. The Hilbert transform is applied to these waveforms to extract their envelopes, allowing for the calculation of the instantaneous power in each frequency band. The band-specific trigger efficiency functions, derived from pre-deployment measurements, were incorporated into the simulation to calculate the probability of triggering for each band given the detected power. A Monte Carlo method using random number generation determines whether a given band triggers, based on its computed probability. This stochastic approach ensures that the simulation accurately reflects the probabilistic nature of the trigger system. The simulation also incorporates the key logic parameters of the TAROGE-4 FPGA-based trigger system, including antenna delay settings, trigger pulse width, and the coincidence criteria required for event detection. These parameters are critical for reproducing the timing and logic of the actual system, allowing for a detailed evaluation of its performance under various operating conditions.

By modeling the complete signal chain and integrating the measured efficiency and FPGA logic, the simulation provides a reliable representation of the TAROGE-4 trigger system. This allows for the evaluation and optimization of detection efficiency for UHECR events, ensuring that the system is effectively tuned to maximize its scientific

doi:10.6342/NTU202500216

output while minimizing false triggers.

5.2.3 Drone Pulser Verification

The drone-borne pulser system was also instrumental in verifying the accuracy of the trigger simulation model for TAROGE-4. By comparing the real trigger efficiency measurements obtained from the drone pulser with the simulated trigger efficiency, the verification process provided critical validation of the trigger simulation framework.

The drone pulser emitted calibrated radio pulses with varying amplitudes and SNR, systematically covering the TAROGE-4 field of view. These signals were processed through the station's 8-band trigger system, and the trigger efficiency was measured as the fraction of emitted pulses that successfully triggered the system. The measured trigger efficiency was then compared with the results predicted by the trigger simulation model. As shown in Fig. 5.3, the real pulser trigger efficiency closely matches the simulated efficiency as a function of SNR. The observed agreement between the two demonstrates that the trigger simulation model accurately captures the behavior of the TAROGE-4 trigger system under realistic operating conditions. Furthermore, the trigger sensitivity was found to be within the expected range of approximately $50\ mV$ to $80\ mV$, confirming that the system's performance aligns with design expectations.

This strong correlation between real data and simulation results validates the accuracy of the trigger simulation model. The model's ability to reproduce real-world performance ensures its reliability for use in further detection simulations, enabling accurate predictions of the trigger system's response to UHECR-induced air showers.

doi:10.6342/NTU202500216

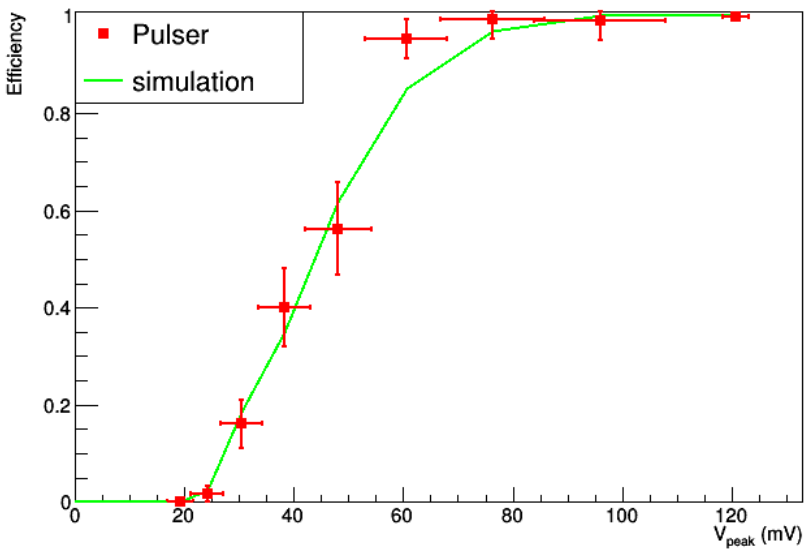

Figure 5.3: Measured trigger efficiency compared to the results predicted by the trigger simulation model. The real pulser trigger efficiency closely matches the simulated efficiency as a function of SNR.

5.3 Monte Carlo Detection Simulation

Monte Carlo detection simulations enable precise mapping of the station's detection efficiency and effective area by integrating modeled UHECR-induced air showers with realistic noise data to replicate the actual signal environment. These simulations systematically evaluate trigger efficiency across a wide range of shower positions, energies, and arrival angles. The detailed assessment of detection efficiency for individual air showers, combined with the calculation of the effective area, provides crucial insights into TAROGE-4's cosmic ray acceptance and allows for the estimation of event rates.

5.3.1 Detection Efficiency for Individual Air Showers

The detection efficiency for individual simulated air showers was meticulously evaluated to determine the effective detection area of the TAROGE-4 station. This analysis

doi:10.6342/NTU202500216

forms the basis for calculating the station's cosmic ray acceptance, expressed as a function of primary energy and arrival angles, $A\Omega(logE, \theta, \phi)$. By convolving the acceptance with an assumed CR flux model, $\Phi(E)$, the expected CR event rate, along with the angular and energy distributions of detected events, can be estimated.

For each simulated air shower, the radio signals were sampled at 120 predefined positions in the star-shaped array, a configuration designed to capture the lateral distribution of the radio emission. To simulate realistic conditions, noise was added to the waveforms using randomly selected minimum-bias noise events from TAROGE-4' s real data. These forced-trigger events were carefully filtered to exclude those contaminated by CW noise, ensuring the added noise represented typical environmental conditions. The combined signal and noise waveforms were processed through a detailed simulation of the TAROGE-4 trigger system. The simulation incorporated the real operational threshold values to maintain consistency with the actual system configuration. For each shower position, the trigger efficiency was calculated as the fraction of simulated events that met the system's trigger criteria. The star-shaped array's outermost ring was used as a boundary, beyond which no triggering was expected. This ensured that the simulation only accounted for regions within the detector's effective field of view. To capture the statistical variability in shower characteristics, including noise effects, an ensemble of $1,200$ simulated events was generated for each shower. This large sample size provided a robust dataset for characterizing the detection efficiency. The resulting detection efficiency data enables precise mapping of TAROGE-4's response to UHECR events across a range of energies and arrival angles.

doi:10.6342/NTU202500216

5.3.2 Effective Area Calculation

The effective detection area for a given shower, $A_{eff}(logE, \cos\theta, \phi)$, was determined by combining the trigger efficiency at sampled positions within the star-shaped array with the simulated geometric area. The antenna station's relative position with respect to the shower axis was randomly sampled within the elliptical region defined by the array. For each sampled position, the trigger efficiency was interpolated from the nearest four points of the star-shaped array. This interpolation ensures smooth spatial variations in trigger efficiency, accurately reflecting the continuous nature of the detector's response across the array geometry.

The average trigger efficiency, $\langle\epsilon\rangle$, was computed across all Monte Carlo simulations (N_{MC}), and is expressed as:

$$\langle\epsilon\rangle = \frac{1}{N_{MC}} \sum_{i=1}^{N_{MC}} \epsilon_i \tag{5.2}$$

where ϵ_i represents the interpolated trigger efficiency at the $i-th$ sampled location. Using the average trigger efficiency, the effective detection area was calculated as:

$$A_{\text{eff}}(\log E, \cos\theta, \phi) = \langle\epsilon\rangle A_{\text{MC}} \cos\theta \tag{5.3}$$

where A_{MC} is the total geometric area covered by the star-shaped array, and $\cos\theta$ accounts for the projection of the incident cosmic ray flux onto the horizontal observation plane.

doi:10.6342/NTU202500216

5.4 Acceptance and Event Distribution

The cosmic ray acceptance is defined as the product of the effective detection area and the solid angle, integrated over all observable directions and energy ranges. This metric quantifies the TAROGE-4 station's sensitivity to UHECR events, providing a basis for estimating event rates and understanding their energy and angular distributions. The acceptance, $A\Omega(\log E, \cos\theta, \phi)$, for a specific energy and arrival direction is expressed as:

$$A\Omega(\log E, \cos\theta, \phi) = A_{\text{eff}}(\log E, \cos\theta, \phi) \cdot \Delta\Omega \tag{5.4}$$

where: $A_{eff}(logE, \cos\theta, \phi)$ is the effective detection area, incorporating the system's trigger efficiency and geometric coverage. $\Delta\Omega = \int_{\theta_1}^{\theta_2}\int_{\phi_1}^{\phi_2} \sin\theta \, d\theta \, d\phi$ represents the solid angle covered by the system for the specified angular range, integrating over the zenith (θ) and azimuth (ϕ) angles.

The dependence of acceptance on energy is illustrated in Fig. 5.4, while its dependence on the zenith angle (θ) is depicted in Fig. 5.5. These visualizations highlight the station's detection capabilities across different cosmic ray energies and arrival angles. In general, the acceptance increases with energy because the strength of the electromagnetic waves emitted by the air showers grows with higher primary energies, enhancing the likelihood of detection. At higher energies above $\sim 2.5\ EeV$, the acceptance also increases with zenith angle. As the zenith angle increases, the distance between the shower maximum and the TAROGE-4 station becomes longer. This geometric effect leads to an expansion of the Cherenkov cone's projected area, which enhances the likelihood of the signal intersecting the detector array and triggering the system. Furthermore, the larger antenna

doi:10.6342/NTU202500216

gain at these angles contributes to improved signal reception, boosting the system's detection efficiency. Conversely, for lower energies, the acceptance decreases at large zenith angles. In these cases, the weaker radio signals produced by showers are insufficient to trigger the detector at greater distances, where signal strength diminishes due to geometric spreading and attenuation. Both proton- and iron-initiated air showers show similar acceptance trends with energy and zenith angle. However, proton showers generally have slightly higher acceptance due to their deeper atmospheric penetration and higher signal intensity at the detector.

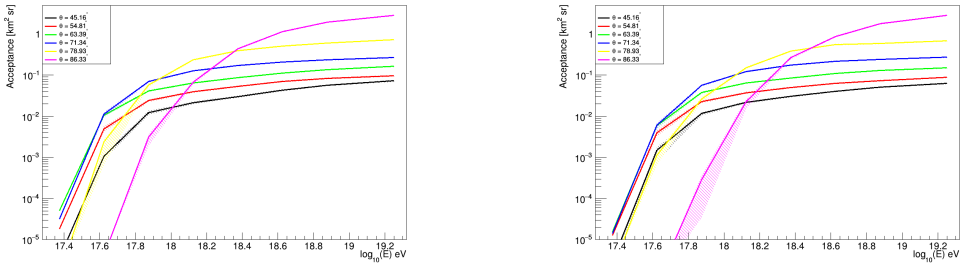

Figure 5.4: The dependence of acceptance on energy for pure proton (left) and iron (right) assumptions is shown. Generally, the acceptance increases with energy, and both assumptions exhibit similar trends in acceptance as a function of energy.

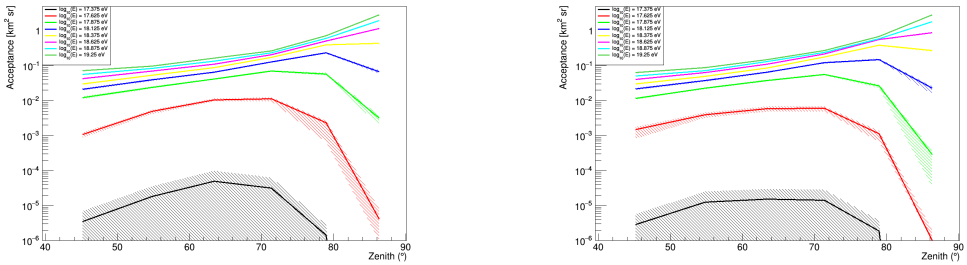

Figure 5.5: The dependence of acceptance on zenith angle for pure proton (left) and iron (right) assumptions is shown. At higher energies above approximately 2.5 EeV, the acceptance increases with zenith angle. Conversely, at lower energies, the acceptance decreases at larger zenith angles. Both assumptions demonstrate similar trends in acceptance as a function of zenith angle and energy.

The expected event rate, R_{total}, is calculated by convolving the cosmic ray flux $\Phi(E)$ with the acceptance and times the analysis efficiency, integrating over the relevant energy

doi:10.6342/NTU202500216

and angular ranges:

$$R_{total} = \int_{E_{\min}}^{E_{\max}} \int_{\Delta\Omega} \eta(\log E, \cos\theta, \phi) A\Omega(\log E, \cos\theta, \phi) \cdot \Phi(E)\, d\Omega\, dE \tag{5.5}$$

where $\Phi(E)$ is the assumed cosmic ray flux model, E_{min} and E_{max} denote the minimum and maximum primary energies considered, $\eta(\log E, \cos\theta, \phi)$ is the analysis efficiency.

The energy and angular distributions of detected events are derived by projecting the total event rate into respective parameter spaces. For the energy distribution, the flux is integrated over all arrival angles with the acceptance and analysis efficiency:

$$R(E) = \int_{\Delta\Omega} \eta(\log E, \cos\theta, \phi) A\Omega(\log E, \cos\theta, \phi) \cdot \Phi(E)\, d\Omega \tag{5.6}$$

For the angular distribution, the flux is integrated over the relevant energy range with the acceptance and analysis efficiency:

$$R(\cos\theta, \phi) = \int_{E_{\min}}^{E_{\max}} \eta(\log E, \cos\theta, \phi) A\Omega(\log E, \cos\theta, \phi) \cdot \Phi(E)\, dE \tag{5.7}$$

The expected number of observed cosmic rays, N_{expt}, can be calculated by multiplying the total expected event rate, R_{total}, by the live time of the TAROGE-4 station, T_{live}:

$$N_{expt} = R_{total} \cdot T_{live} \tag{5.8}$$

The expected cosmic ray event rate distributions as functions of zenith angle, are shown in Fig. 5.6 for proton showers (left) and iron showers (right) across different energy

doi:10.6342/NTU202500216

ranges. These distributions are computed assuming the Auger cosmic ray energy spectrum [130] and a one-year operation live time. This figure displays the distributions under the assumption of 100% analysis efficiency, representing an idealized case for benchmarking. In contrast, Fig. 5.7 incorporate the realistic analysis efficiency of approximately 53% (varying with angles and primary energy), which will be elaborated on in the next chapter.

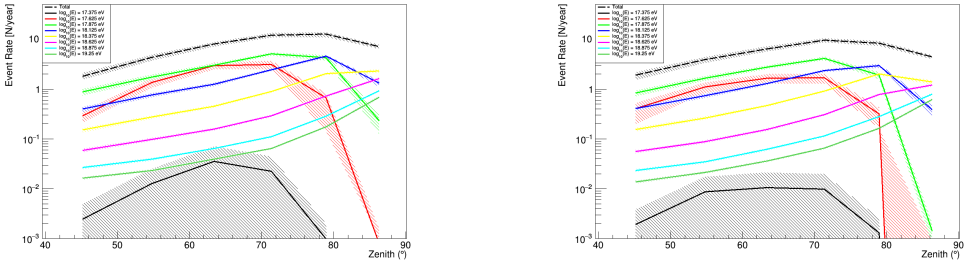

Figure 5.6: The expected cosmic ray event rate distributions as functions of zenith angle for pure proton showers (left) and iron showers (right) across different energy ranges assuming 100% analysis efficiency. These distributions are computed assuming the Auger cosmic ray energy spectrum [130] and a one-year operation live time.

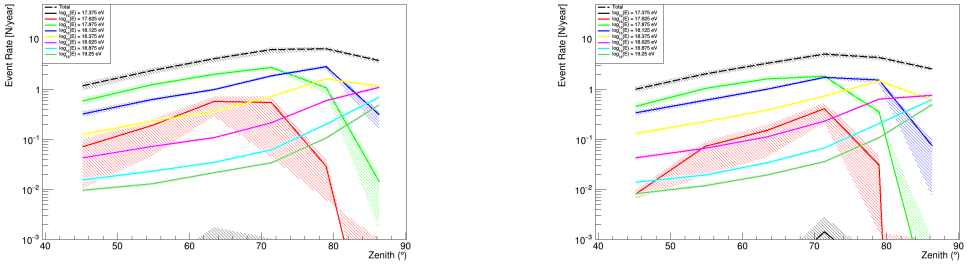

Figure 5.7: The expected cosmic ray event rate distributions as functions of zenith angle for pure proton showers (left) and iron showers (right) across different energy ranges with realistic analysis efficiency. These distributions are computed assuming the Auger cosmic ray energy spectrum [130] and a one-year operation live time.

Similarly, the expected cosmic ray event rate distributions as functions of primary energy are illustrated in Fig. 5.8 for proton showers (left) and iron showers (right) across different zenith angle ranges. These distributions, also based on the Auger cosmic ray energy spectrum and a one-year live time. This figure displays the distributions under the assumption of 100% analysis efficiency, representing an idealized case for benchmarking while Fig. 5.9 incorporate the realistic analysis efficiency of approximately 53%.

doi:10.6342/NTU202500216

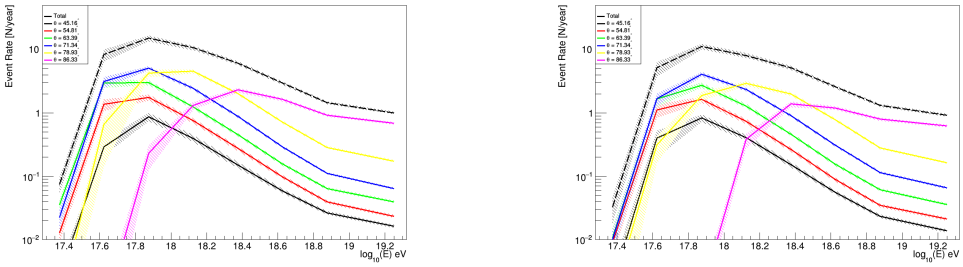

Figure 5.8: The expected cosmic ray event rate distributions as functions of energy for pure proton showers (left) and iron showers (right) across different energy ranges assuming 100% analysis efficiency. These distributions are computed assuming the Auger cosmic ray energy spectrum [130] and a one-year operation live time.

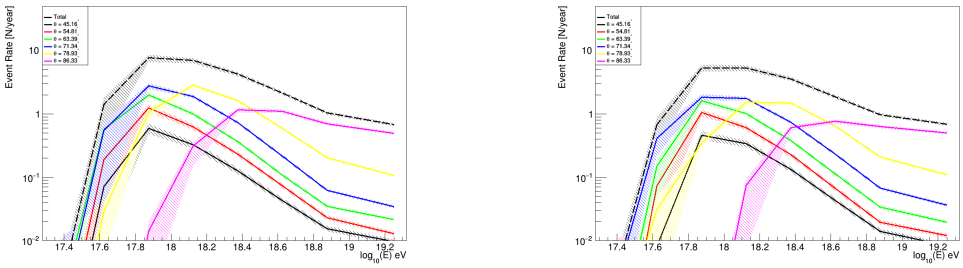

Figure 5.9: The expected cosmic ray event rate distributions as functions of energy for pure proton showers (left) and iron showers (right) across different energy ranges assuming 100% analysis efficiency. These distributions are computed assuming the Auger cosmic ray energy spectrum [130] and a one-year operation live time.

doi:10.6342/NTU202500216

Most of the detectable cosmic ray events originate from inclined zenith angles between $70°$ and $80°$ and and are concentrated around $10^{18}\ eV$. For an idealized case assuming 100% analysis efficiency, the station is expected to detect $45.9\pm^{4.8}_{5.3}$ events per year under a pure proton flux assumption, compared to $34.5\pm^{4.1}_{3.8}$ events per year for a pure iron flux assumption. However, when accounting for the real analysis efficiency of approximately 53%, the expected detection rates decrease to $24.2\pm^{3.3}_{2.5}$ events per year for a pure proton flux and $18.4\pm^{2.2}_{1.9}$ events per year for a pure iron flux. The disparity between proton and iron flux detection rates stems from differences in shower development. Proton-initiated showers tend to penetrate deeper into the atmosphere, producing stronger signals at the detector level, leading to a higher detection rate. In contrast, iron-initiated showers, due to their shallower atmospheric penetration, result in slightly lower detection rates.

5.4.1 Potential Improvement

The TAROGE-4 station has significant potential for upgrades that could dramatically enhance its detection capabilities. One of the most promising advancements lies in the adoption of phased-array trigger systems implemented through cutting-edge RFSoC technology. Phased-array triggers would allow for real-time beamforming and improved signal directionality, significantly increasing the system's sensitivity to EAS signals while minimizing noise interference. Fig. 5.10 shows the conceptual diagram of an RFSoC design for a real-time phased-array trigger. Through this design, more than 100 bins for phased-array triggering can be achieved on the Xilinx ZU28DR RFSoC chip, leading to an expected 2 to 4-fold increase in event rates.

The integration of RFSoC technology into TAROGE-4's trigger system would bring

doi:10.6342/NTU202500216

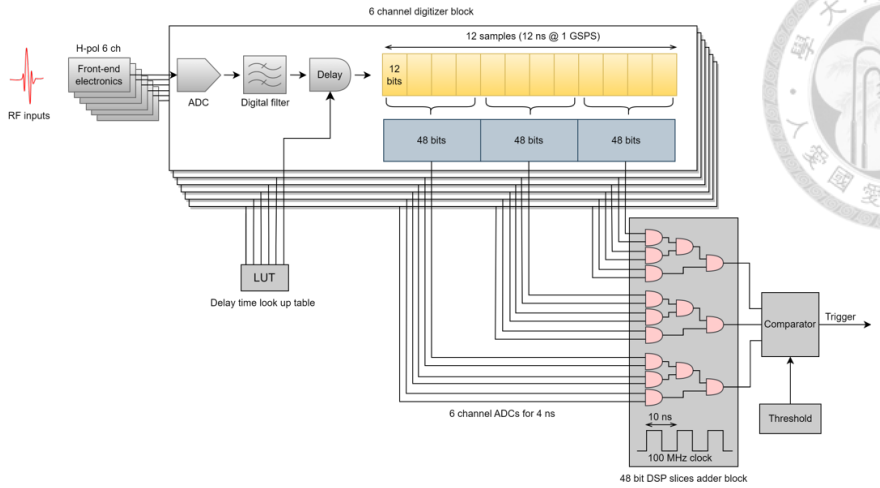

Figure 5.10: Concept diagram of an RFSoC design for real-time phased-array triggering.

several benefits. By dynamically adjusting the detection beam in response to incoming signals, the phased-array trigger would enable the system to pinpoint events with higher accuracy and efficiency. This approach reduces the need for static thresholds and mitigates false positives caused by random noise. Additionally, the advanced processing capabilities of RFSoC allow for real-time signal analysis, further improving the identification of genuine UHECR events. These advancements could transform the station's capability, potentially detecting more than 100 UHECR candidates annually. Such improvements would position TAROGE-4 as a highly efficient and compact detector, capable of making substantial contributions to UHE particle research.

doi:10.6342/NTU202500216

Chapter 6 Cosmic Ray Searching

The analysis of TAROGE-4 data focuses on identifying UHECR-induced air shower events, which serve as both calibration sources and scientific targets. These events enable the characterization of the detector's performance, including event rate, energy, angular, and polarization distributions. Comparisons with simulations described in previous chapters are conducted to verify and refine the system's sensitivity.

Given the low flux of UHE cosmic rays and neutrinos, the majority of recorded events are expected to be noise-triggered, particularly with the low trigger thresholds designed to maximize sensitivity. As a result, an effective noise rejection method with high signal retention is critical for the analysis. TAROGE-4's framework combines template matching with additional flexible methodologies, ensuring that potentially interesting impulsive events are not discarded prematurely.

The analysis starts by applying quality and thermal cuts to filter out impulsive RF noise and isolate viable events. These filtered events are then projected onto the sky and the ocean surface for spatial clustering. Isolated singlets with high cross-correlation to templates are classified as potential signal candidates.

To ensure robust and unbiased results, data from one year is used to establish selection criteria, while the remaining data remains blinded until these criteria are finalized. This

doi:10.6342/NTU202500216

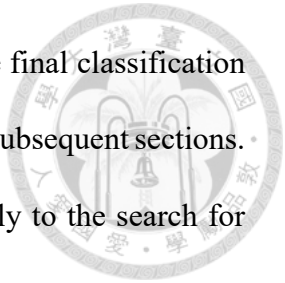

approach minimizes analysis bias and enhances result reliability. The final classification and detailed characteristics of TAROGE-4 events will be addressed in subsequent sections. By employing this methodology, TAROGE-4 contributes significantly to the search for UHECRs and the refinement of techniques for UHE neutrino detection.

6.1 Datasets

The dataset used for cosmic ray searches with the TAROGE-4 station encompasses data collected between September 2019 and June 2024, covering nearly five years of operation. However, due to scheduled maintenance, environmental factors, and other operational interruptions, the effective live time for this dataset amounts to 2.3 years.

During this effective observation period, a total of 548,154,000 events were recorded. These events represent the raw data pool from which cosmic ray candidates are identified after applying selection criteria and noise rejection algorithms. The extended duration of data collection, combined with the significant volume of events, provides a robust basis for identifying UHECR signals and conducting related analyses.

Further data refinement and event selection processes will be detailed in subsequent sections, where methodologies for noise reduction, event classification, and the identification of cosmic ray candidates are described. This dataset offers a valuable opportunity to enhance our understanding of UHECR phenomena and validate the performance of the TAROGE-4 system.

doi:10.6342/NTU202500216

6.2 Selection Criteria

The identification of cosmic ray candidates in TAROGE-4 data employs a multi-step approach to ensure that detected events exhibit characteristics consistent with UHECRs and UHECNs. The following criteria leverage techniques refined through previous experiments, ensuring reliable event selection while maintaining sensitivity to rare signals.

6.2.1 Dynamic Filtering and Cross-correlation

Dynamic filtering and cross-correlation are integral to refining the selection of potential EAS events, enabling the effective suppression of noise while enhancing the fidelity of identified signals. This approach dynamically adapts to varying environmental conditions, filtering out CW noise and isolating impulsive events with high confidence.

Dynamic filtering addresses the challenges posed by time-dependent CW noise, which can vary significantly in both frequency and intensity. While constant CW noise can be mitigated using static notch filters, sporadic CW signals that intermittently occur within the frequency band require a more adaptive approach.

For each event, a frequency is flagged as CW if its power spectrum exceeds that of its neighboring frequencies by more than $10\ dB$. If this condition is triggered, the judgment threshold is reduced from $10\ dB$ to $5\ dB$ for the adjacent frequencies. This adaptive filtering method identifies and excludes time-varying CW components, ensuring that the remaining signal retains its broadband characteristics, which are indicative of EAS events. By combining this method with a constant CW notch filter, dynamic filtering effectively reduces spurious triggers and improves the signal-to-noise ratio. The filtered signals are

doi:10.6342/NTU202500216

then prepared for further analysis, retaining their impulsive broadband nature.

After dynamic filtering, cross-correlation techniques are employed to identify true cosmic ray candidates. EAS signals, being coherent across multiple antennas, exhibit time delays in arrival that correspond to their direction of origin. The cross-correlation value is calculated for each event by comparing the time delays between pairs of antennas. Events with cross-correlation values above a predefined threshold (e.g., 0.7) are classified as reliable candidates. This threshold ensures that only signals with strong coherence, indicative of a single source, are retained, while random fluctuations and noise-induced artifacts are excluded.

6.2.2 Software Trigger

The software trigger serves as a secondary filtering mechanism to refine event selection beyond the hardware trigger. This step leverages the broadband nature of EAS signals to distinguish them from noise. Using fast Fourier transforms (FFT), the power spectrum of each signal is calculated and compared to the dynamically determined background noise level. This noise level is estimated from unbiased forced trigger events collected during the same data run, typically consisting of approximately 250 events recorded over ~ 17 minutes.

To suppress thermal noise, a signal strength-dependent threshold (minimum $4\ dB$) is applied to the power spectrum. At least 60% of the frequency bands must exceed this threshold for either H-pol or V-pol signals. This condition effectively mitigates the impact of CW noise, which typically affects only a limited range of frequency bands. Furthermore, by incorporating a cut based on cross-correlation values, the software trigger is able

doi:10.6342/NTU202500216

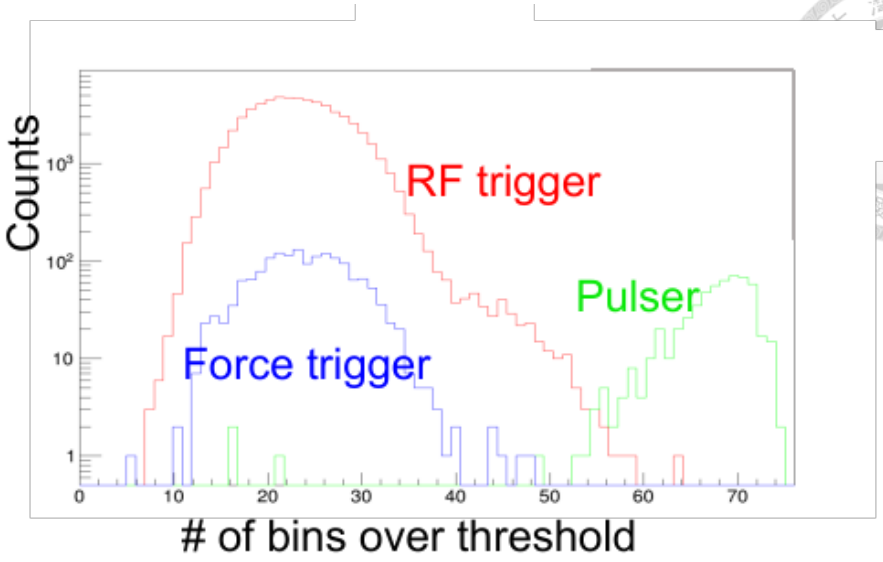

Figure 6.1: The distribution of the number of frequency bins exceeding the software trigger threshold for RF-triggered, forced-triggered, and pulser data.

to enhance its noise rejection capabilities significantly. Fig. 6.1 illustrates the distribution of the number of frequency bins exceeding the software trigger threshold for RF-triggered, forced-triggered, and pulser data (one day of data). This combination of frequency-based thresholds and cross-correlation filtering results in the elimination of approximately 96% of RF-triggered events.

6.2.3 Power Ratio Between Antennas

Impulsive noise originating from beneath the cliff poses a particular challenge. Although the cliff obstructs this noise for all of TAROGE-4's antennas except for the one located near the cliff, diffraction effects still enable all antennas to receive the noise, triggering our system. Furthermore, this diffraction alters the TDOA compared to a direct propagation from its source angles and distorts the waveform. Consequently, this causes a misreconstruction of the event's direction.

This challenge can be addressed by implementing a power ratio cut between the an-

doi:10.6342/NTU202500216

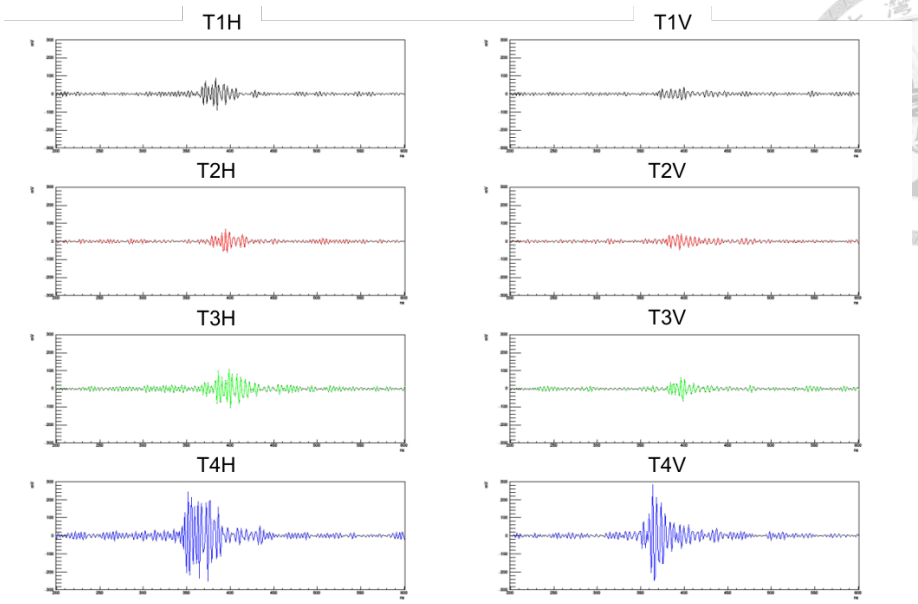

Figure 6.2: Power imbalance between channels. The antenna located near the cliff (bottom panels) primarily receives the direct signal, while the other antennas primarily receive the diffracted signal.

tennas. Given that the antenna located near the cliff primarily receives the direct signal, while the other antennas primarily receive the diffracted signal, this leads to an imbalance in power between channels as shown in Fig. 6.2. The power ratio is defined as the lowest power among all antennas divided by the power of the antenna closest to the cliff. Events with a power ratio below 0.5 are removed, effectively suppressing noise originating from beneath the cliff while retaining true cosmic ray signals.

6.2.4 Reconstruction Reliability

After broadband signals are identified, interferometric mapping is employed to determine the most probable direction of arrival for each event. This technique leverages the coherence of signals detected across multiple antennas, using their time differences of arrival to accurately localize the source.

To ensure the reliability of this reconstruction process, only events with an average

doi:10.6342/NTU202500216

cross-correlation value of 0.7 or higher across all channel pairs are retained. Furthermore, the interferometric map must exhibit a clear hot spot corresponding to the reconstructed direction. A well-defined hot spot ensures that the signal source is localized to a single, coherent region, further reducing the likelihood of misinterpretation caused by noise or signal distortion. By imposing these stringent criteria—requiring both a high average cross-correlation value and a clear hot spot in the interferometric map—the reconstruction process achieves a high level of precision and robustness. These measures effectively filter out low-quality signals, random noise, and artifacts, ensuring the retention of genuine cosmic ray events for subsequent analysis.

6.2.5 Multi-pulses Anthropagenic Noise

The event waveforms recorded over a span of 1200 nanoseconds by the DAQ system are expected to exhibit a single, distinct main pulse characteristic of extensive air shower (EAS) events. However, due to the suburban location of the TAROGE-4 station, waveforms are frequently contaminated by additional small pulses originating from anthropogenic noise as shown in Fig. 6.3. These small pulses often arise from local interference sources and are unrelated to cosmic ray events. A key characteristic of real EAS events is that their source direction is unlikely to coincide with the directions of these contaminating small pulses. To exploit this distinction, a correlation map is generated for the small pulses, capturing their spatial distribution relative to the reconstructed main pulse.

Using this map, a constraint cut is applied based on the correlation value of the small pulses in the direction of the main pulse. If small pulses exhibit significant correlation in the same direction as the main pulse, the event is flagged as noise. This filtering step effectively isolates genuine EAS events by distinguishing them from impulsive noise con-

doi:10.6342/NTU202500216

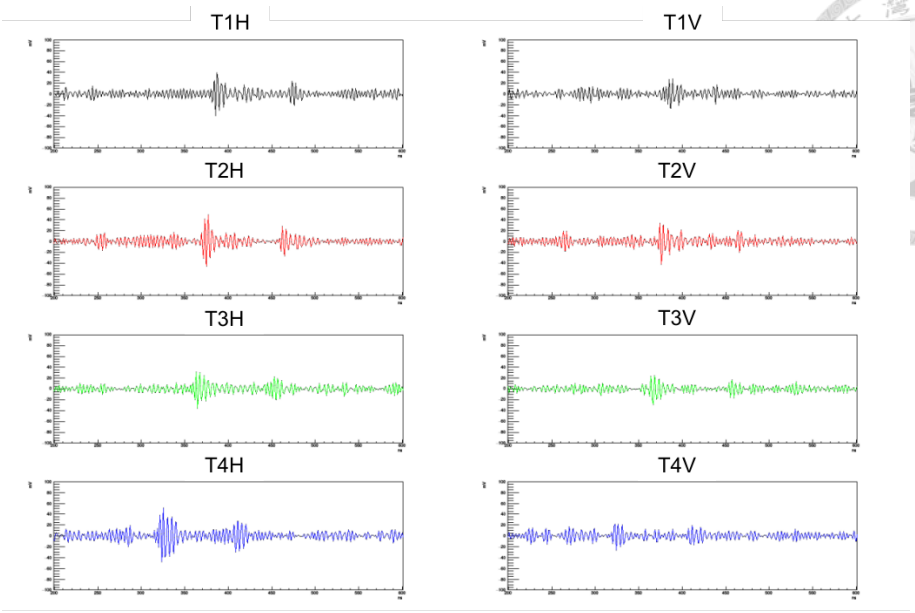

Figure 6.3: Multi-pulses anthropogenic noise.

taminating the waveforms.

6.2.6 Lightning Events

During days with lightning activity, a significant number of events are detected within the FoV of TAROGE-4. These events are attributed to the electromagnetic interference generated by lightning strikes, which can mimic the impulsive nature of ultra-high-energy air shower signals.

To ensure the integrity of the dataset, lightning days are identified and confirmed using open weather data provided by the Central Weather Administration in Taiwan. All events recorded during these periods are subsequently eliminated from the analysis. This precautionary measure effectively removes the contamination caused by lightning activity, preventing false positives in the event selection process.

An angular distribution map of events from a lightning day is shown in Fig. 6.4 as an example. The clustering and abnormal distribution of events on such days highlight the

doi:10.6342/NTU202500216

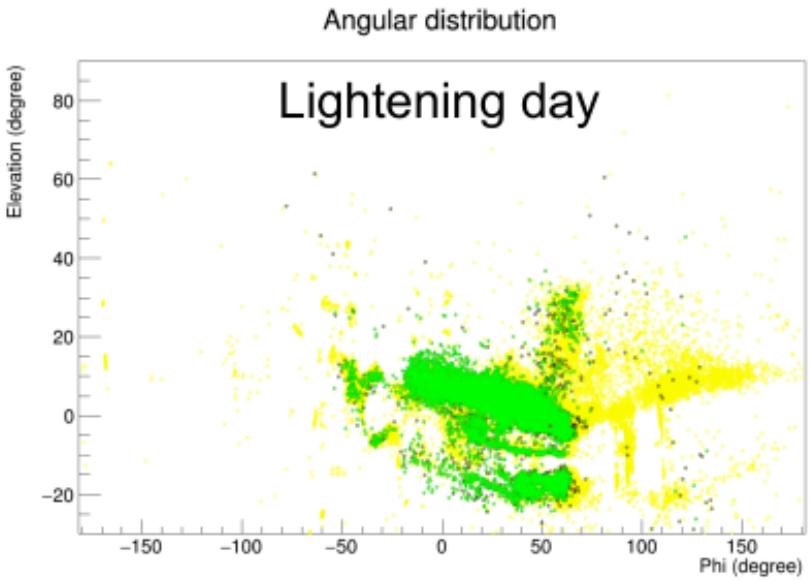

Figure 6.4: An angular distribution map showing impulses recorded over a single day with lightning activity.

necessity of this elimination process. By filtering out lightning-related events, TAROGE-4 maintains a clean dataset for the analysis of ultra-high-energy cosmic ray and neutrino signals.

6.2.7 Temporal and Spatial Cluster

A temporal and spatial cluster map is generated to identify and exclude events associated with persistent noise or interference sources. This step is performed after applying the above-mentioned cuts, but with a lower threshold of 0.6 for the cross-correlation value, as opposed to the 0.7 used in the reconstruction reliability cut. Lowering the threshold increases sensitivity to potential clusters, ensuring that no significant noise sources are overlooked. However, this adjustment also leads to a reduction in analysis efficiency. Figure 6.5 illustrates the inefficiency caused by these selection criteria across various angles within the FoV.

Events are considered part of a cluster if they are spatially coincident within a $\pm 5^{\circ}$

doi:10.6342/NTU202500216

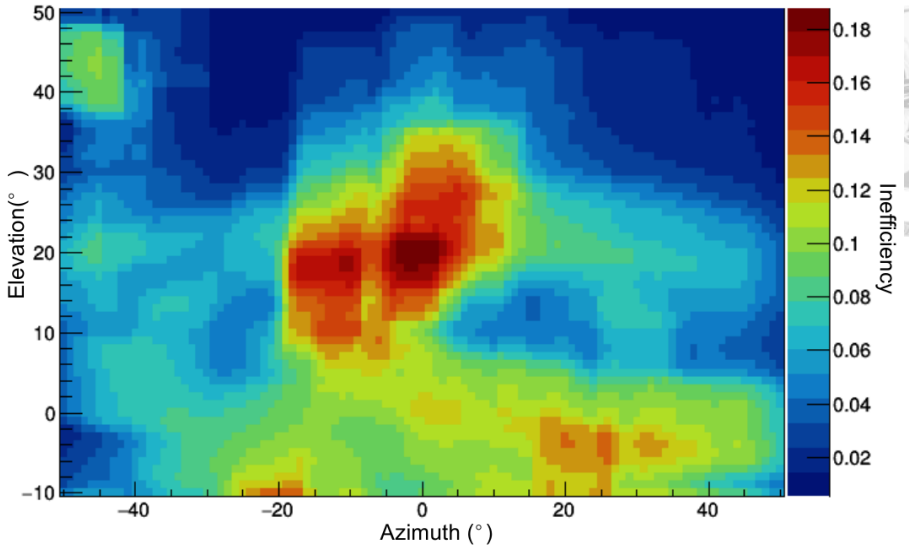

Figure 6.5: Inefficiency caused by temporal and spatial isolation selection criteria across various angles within TAROGE-4 FoV.

margin in both elevation and azimuth and temporally coincident within a $\pm 600\ s$ window. Any events identified as part of such clusters are removed from the dataset.

This cluster-based filtering method enhances the isolation of signals of interest by effectively eliminating events linked to recurring interference or persistent noise sources. By removing clustered noise events, this step ensures the retained data predominantly represents isolated, genuine cosmic ray signals.

6.2.8 Template matching

Template matching is a powerful method for identifying EAS signals in the TAROGE-4 dataset. The templates serve as theoretical benchmarks, representing the expected characteristics of EAS signals as modeled through CoREAS simulations. These simulations are further refined by convolving the outputs with TAROGE-4's system response, effectively mimicking the received EAS signals under real-world detection conditions. The templates incorporate key factors influencing EAS signal behavior, such as atmospheric

doi:10.6342/NTU202500216

interactions, geomagnetic effects, and the antenna response of the TAROGE-4 system. This comprehensive modeling ensures that the templates realistically capture the signal characteristics expected for UHECR events.

To identify potential UHECR candidates, the detected waveforms are compared against the templates using a cross-correlation process. This process evaluates the similarity between the recorded signals and the simulated templates, assigning a cross-correlation score to each event. Events with scores exceeding 0.75 are classified as potential UHECR candidates, ensuring that only signals closely matching the expected profiles are retained.

6.3 Analysis Efficiency

Table 6.1 summarizes the efficiency of each selection criterion applied to the TAROGE-4 dataset and Monte Carlo simulated events as described in 5. The analysis evaluates both the survival rate of RF-triggered events after each selection step and the efficiency of retaining genuine CR signals based on MC simulations.

Table 6.1: Selection Criteria Efficiency for TAROGE-4 Dataset and MC Simulated CR Events

Criteria	**RF-Trig.**	**RF-Trig. Surv. Rate**	**MC Signal Eff.**
Total events	548,154,000	100%	100%
X-cor. & Soft. Trig.	21,758,499	3.97%	73%
Power Ratio	8,402,721	1.53%	73%
Quality	7,072,882	1.29%	69%
Lightning	292,055	0.05%	N/A
Isolation	221	4.03×10^{-7}	62%
Template Matching	57	1.04×10^{-7}	53%

The initial filtering, which includes the cross-correlation and soft trigger criteria, serves as the first significant step in the selection process. This step reduces the total events from 548 million to approximately 21.76 million, retaining 3.97% of the data. This step

doi:10.6342/NTU202500216

achieves a high signal retention efficiency of 73% for MC-simulated CR events, demonstrating its ability to efficiently filter noise while preserving true signals.

The power ratio criterion further reduces the dataset to 8.4 million events, with a survival rate of 1.53%. Importantly, this step maintains the same signal efficiency (73%) as the initial filter, confirming its robustness in eliminating noise originating from beneath the cliff without losing genuine CR events.

The quality cut, which encompasses the reconstruction reliability and multi-pulse anthropogenic noise criteria, significantly refines the dataset by imposing stricter requirements on signal quality. This step reduces the number of events from 8.4 million to approximately 7.07 million, corresponding to a 1.29% survival rate. The MC signal efficiency decreases slightly to 69%, indicating that while the stricter criteria effectively eliminate low-quality signals and anthropogenic noise, they also introduce a minor reduction in the retention of genuine cosmic ray events. This trade-off ensures that the remaining dataset is of higher quality and reliability, enabling more accurate analysis and reconstruction of UHECR signals.

The removal of events associated with lightning activity dramatically reduces the dataset to $292,055$ events, corresponding to a survival rate of just 0.05%. Since this step is aimed at eliminating environmental noise, it does not affect MC signal efficiency.

The isolation criterion, which removes clustered events, reduces the dataset to only 221 events, with a survival rate of $4.03 \cdot 10^{-7}$. Although the signal efficiency decreases to 62%, this step ensures that the remaining events are isolated and free from interference.

The final step, template matching, identifies 57 potential UHECR candidates from the entire dataset. While the survival rate drops to $1.04 \cdot 10^{-7}$, the signal efficiency remains at

doi:10.6342/NTU202500216

53%, indicating that the remaining events closely match the expected profiles of UHECR-induced air showers.

6.4 Results

6.4.1 Background Estimates

Accurately estimating background noise is essential for identifying EAS candidates and minimizing false positives in the TAROGE-4 dataset. The ABCD method is employed to estimate background contamination in the signal-dominated region (Region A) and distinguish it from noise-dominated regions.

The method relies on the assumption that the two observables, V_1 (temporal and spatial isolation) and V_2 (template matching), are statistically uncorrelated for background events. A total of $292,055$ events, remaining after the lightning cut, are used in this analysis. Based on the two observables, the data is partitioned into four regions:

- **Region A (Signal + Background):** High V_1 (more isolated) and high V_2 (more signal-like).
- **Region B (Background):** Low V_1 (less isolated) and high V_2.
- **Region C (Background):** High V_1 and low V_2.
- **Region D (Background):** Low V_1 and low V_2.

The assumption of independence allows the estimation of the background contamination in Region A (N_A^{bkg}) using the formula:

doi:10.6342/NTU202500216

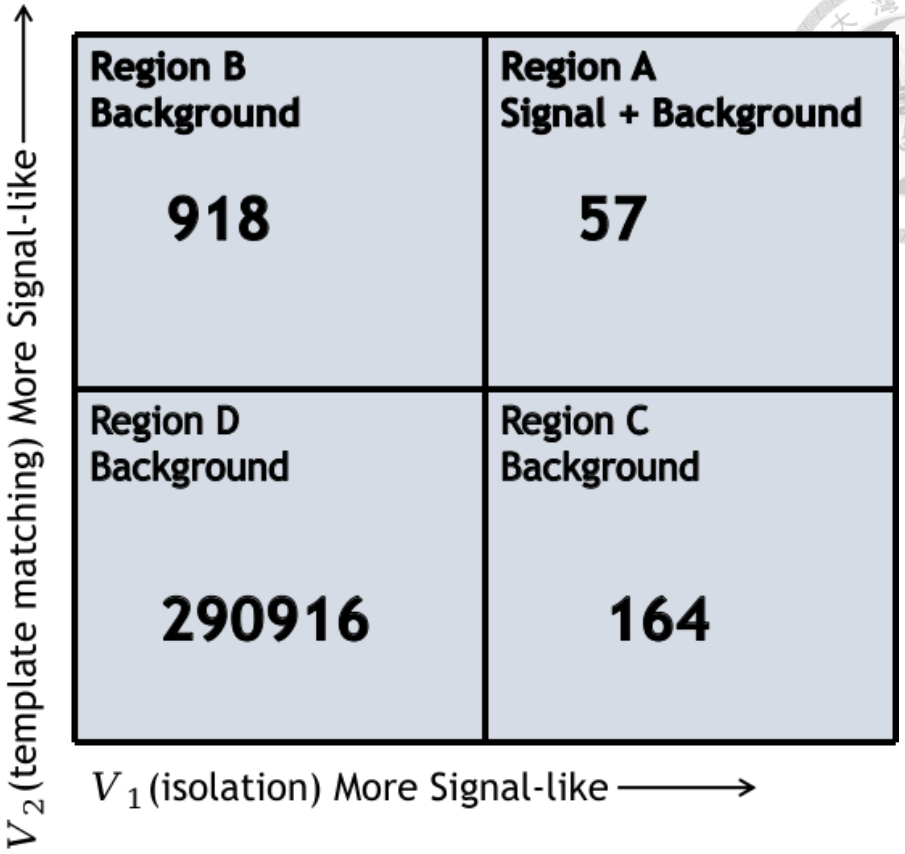

Figure 6.6: ABCD method for background estimation in this CR search analysis.

$$N_A^{\text{bkg}} = \frac{N_B \cdot N_D}{N_C} \tag{6.1}$$

where: N_A^{bkg} is estimated number of background events in Region A and N_B, N_C, N_D are number of events in Regions B, C, and D, respectively as shown in Fig. 6.6. The background contribution to Region A is calculated to be approximately 0.52 events.

The signal yield in Region A is then calculated by subtracting the estimated background from the total number of events in Region A:

$$N_A^{\text{signal}} = N_A^{\text{total}} - N_A^{\text{bkg}} \tag{6.2}$$

This calculation demonstrates that the signal in Region A is dominated by genuine

doi:10.6342/NTU202500216

cosmic ray candidates, with minimal background contamination.

6.4.2 CR Events

The CR candidate events identified after applying all selection criteria represent high-confidence detections of UHECRs. A total of 57 events remain as potential CR candidates. These events exhibit strong cross-correlation with templates, clear isolation from noise, and characteristics consistent with EAS signals.

Among these 57 candidates:

- **52 events** are identified as direct CR candidates.
- **1 event** is identified as an ocean reflection CR candidate.
- **4 events** exhibit both direct and reflected signals.

Fig. 6.7 illustrates an example of a direct CR candidate event 42337_4989. On the left, the deconvolved waveform after the coherent sum of all channels is shown for both E_θ and E_ϕ. On the right, the angular distribution map for all RF-triggered events during the day is presented.

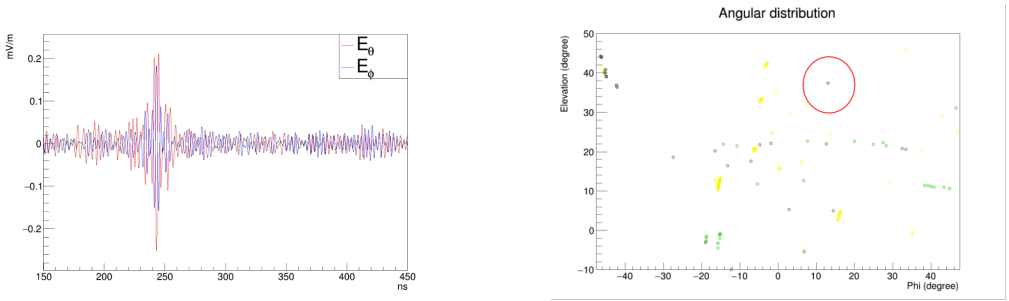

Figure 6.7: Filtered, deconvolved, coherently summed waveforms of direct CR candidate event 00042337_4989 (left). And the corresponding angular distribution map for all RF-triggered events during that day with red circle indicates the CR candidate (right).

In the angular distribution map:

doi:10.6342/NTU202500216

- The **red circle** indicates the CR candidate.
- The **yellow circles** represent events that passed the cross-correlation and soft trigger selection criteria but failed the power ratio cut.
- The **black circles** indicate events that passed the power ratio cut but failed the quality cut.
- The **green circles** are events that passed the quality cut but failed the isolation cut.

The information of the 57 CR candidate events is summarized in Table 6.2. The table includes the following items for each event: event number, reconstructed elevation angle, reconstructed azimuth angle, the average cross-correlation coefficient between channel pairs, the portion of frequency bands passing the threshold in the software trigger selection criteria, the power ratio between the smallest channel and the nearest cliff channel, the cross-correlation coefficient value from template matching, the measured E_ϕ/E_θ ratio, and the expected E_ϕ/E_θ ratio, considering a 10% influence from the Askaryan effect. Detailed waveforms for all CR candidate events are presented in Appendix A and the following chapter.

The final set of CR events will undergo further analysis to determine their energy, angular distributions, and polarization properties, contributing to a deeper understanding of UHECR characteristics and their origins.

Table 6.2: Summary of 57 CR candidates.

Event #	θ (°)	ϕ (°)	X-cor.	ST	PR	TM	M. E_ϕ/E_θ	E. E_ϕ/E_θ
02131_9340	28.7	-12.1	0.89	0.99	0.81	0.92	0.48 ± 0.03	$-0.51\pm^{+0.13}_{-0.36}$
02329_4570	34.4	-42.7	0.82	0.90	0.98	0.89	0.33 ± 0.06	$-0.26\pm^{+0.11}_{-0.19}$
03561_9374	9.3	-59.5	0.85	0.86	0.62	0.89	1.43 ± 0.15	$-1.20\pm^{+0.48}_{-1.39}$

doi:10.6342/NTU202500216

Event #	θ (°)	ϕ (°)	X-cor.	ST	PR	TM	M. E_ϕ/E_θ	E. E_ϕ/E_θ
03831_7180	22.0	-62.5	0.88	0.88	0.73	0.90	0.84 ± 0.07	$-0.76\pm^{+0.18}_{-0.44}$
04085_3887	10.0	-15.1	0.81	0.65	0.80	0.91	0.81 ± 0.14	$-0.68\pm^{+0.15}_{-0.37}$
04441_0902	27.7	-44.5	0.89	1.00	1.00	0.93	0.39 ± 0.01	$-0.42\pm^{+0.19}_{-0.39}$
06868_7207	8.7	-11.8	0.90	0.83	0.75	0.93	0.61 ± 0.07	$-0.68\pm^{+0.14}_{-0.36}$
06916_0628	25.7	-31	0.84	0.77	0.85	0.88	0.33 ± 0.07	$-0.48\pm^{+0.15}_{-0.38}$
07214_2950	31.4	5.6	0.77	0.83	0.76	0.84	0.57 ± 0.09	$-0.63\pm^{+0.14}_{-0.33}$
09653_2472	7.4	-31.6	0.93	0.91	0.83	0.92	0.77 ± 0.04	$-0.76\pm^{+0.17}_{-0.22}$
11351_0109	-0.5	24.2	0.85	0.81	0.78	0.82	0.74 ± 0.14	$-0.76\pm^{+0.15}_{-0.39}$
11897_3658	4.6	-16.69	0.93	0.95	0.79	0.93	0.71 ± 0.07	$-0.73\pm^{+0.15}_{-0.38}$
13379_7040	9.7	-30.7	0.96	0.96	1.00	0.91	0.71 ± 0.06	$-0.73\pm^{+0.17}_{-0.44}$
13837_2723	25.3	-30.1	0.92	0.91	0.71	0.92	0.55 ± 0.05	$-0.59\pm^{+0.14}_{-0.33}$
14052_4962	3.1	-31.1	0.76	0.74	0.68	0.86	0.70 ± 0.21	$-0.82\pm^{+0.17}_{-0.47}$
14745_0254	28.3	-7.6	0.82	0.78	0.64	0.89	0.78 ± 0.10	$-0.59\pm^{+0.14}_{-0.33}$
16319_6029	2.61	-22.56	0.98	0.96	0.78	0.92	0.72 ± 0.03	$-0.76\pm^{+0.16}_{-0.21}$
16489_4481	6.7	20.8	0.95	0.94	0.84	0.89	0.67 ± 0.07	$-0.78\pm^{+0.15}_{-0.18}$
16523_5369	25.9	-31.3	0.96	0.95	1.00	0.92	0.56 ± 0.02	$-0.47\pm^{+0.15}_{-0.38}$
16628_7515	16.6	-52.9	0.87	0.89	1.00	0.89	0.70 ± 0.08	$-0.79\pm^{+0.24}_{-0.34}$
17782_5664	12.4	-1.3	0.84	0.74	1.00	0.91	0.75 ± 0.11	$-0.68\pm^{+0.14}_{-0.16}$
17931_4479	14	-11.5	0.74	0.76	0.65	0.90	0.53 ± 0.10	$-0.65\pm^{+0.14}_{-0.35}$
19019_0666	6.1	-7.6	0.88	0.88	0.75	0.89	0.72 ± 0.09	$-0.68\pm^{+0.14}_{-0.16}$
20487_0996	29	-13.9	0.84	0.73	0.95	0.88	0.49 ± 0.09	$-0.50\pm^{+0.14}_{-0.32}$
21455_1082	7.4	-31.6	0.98	0.98	0.74	0.94	0.75 ± 0.03	$-0.76\pm^{+0.17}_{-0.22}$
27460_6479	13.3	-5.8	0.84	0.83	0.77	0.92	0.81 ± 0.10	$-0.66\pm^{+0.14}_{-0.34}$
27802_2184	24.6	-19	0.92	0.96	1.00	0.90	0.43 ± 0.05	$-0.53\pm^{+0.14}_{-0.34}$
28891_9280	-0.75	1.2	0.87	0.59	0.80	0.89	0.76 ± 0.11	$-0.71\pm^{+0.14}_{-0.35}$
29653_4385	9.6	1.1	0.92	0.85	0.95	0.91	0.69 ± 0.08	$-0.69\pm^{+0.14}_{-0.36}$
31621_7622	2.1	18.9	0.93	0.88	0.78	0.84	0.69 ± 0.11	$-0.75\pm^{+0.16}_{-0.41}$
32085_1672	18.3	-54.7	0.96	0.75	0.70	0.86	0.48 ± 0.08	$-0.76\pm^{+0.18}_{-0.41}$
33702_9219	28.3	-50.2	0.83	0.78	0.70	0.91	0.51 ± 0.08	$-0.41\pm^{+0.14}_{-0.37}$
38208_3709	18.7	11.9	0.78	0.85	0.75	0.84	0.42 ± 0.09	$-0.73\pm^{+0.14}_{-0.36}$

doi:10.6342/NTU202500216

Event #	θ (°)	ϕ (°)	X-cor.	ST	PR	TM	M. E_ϕ/E_θ	E. E_ϕ/E_θ
38955_2812	27.3	-1.9	0.83	0.75	0.80	0.88	0.45 ± 0.05	$-0.59\pm^{+0.14}_{-0.32}$
40661_5357	2.9	-24.86	0.87	0.91	0.85	0.92	0.78 ± 0.09	$-0.75\pm^{+0.16}_{-0.41}$
42337_4989	21.0	-16.3	0.83	0.95	0.78	0.92	0.73 ± 0.09	$-0.58\pm^{+0.14}_{-0.34}$
43272_5426	11.7	-12.4	0.90	0.93	0.83	0.93	0.70 ± 0.05	$-0.66\pm^{+0.14}_{-0.36}$
43347_7075	30.7	-11.2	0.83	0.85	0.88	0.91	0.59 ± 0.10	$-0.50\pm^{+0.13}_{-0.30}$
43598_5124	0.5	-56.65	0.86	0.83	0.93	0.94	1.36 ± 0.10	$-1.41\pm^{+0.51}_{-0.69}$
43631_4175	27.7	-43.0	0.80	0.94	0.85	0.93	0.32 ± 0.02	$-0.42\pm^{+0.18}_{-0.44}$
43654_6513	31.7	13.1	0.83	0.79	0.69	0.89	0.71 ± 0.11	$-0.71\pm^{+0.17}_{-0.39}$
44774_7894	18.3	-43.9	0.75	0.83	0.78	0.83	0.68 ± 0.13	$-0.65\pm^{+0.19}_{-0.53}$
45853_8910	31.6	-23.8	0.78	0.88	0.88	0.93	0.45 ± 0.05	$-0.41\pm^{+0.13}_{-0.32}$
46102_1355	41.6	-32.2	0.83	0.95	0.93	0.91	0.15 ± 0.03	$-0.18\pm^{+0.15}_{-0.35}$
46192_3233	15.4	0.2	0.92	0.88	0.89	0.92	0.62 ± 0.09	$-0.67\pm^{+0.13}_{-0.34}$
46456_6689	41.6	21.8	0.77	0.77	0.88	0.87	0.90 ± 0.12	$-0.79\pm^{+0.15}_{-0.39}$
47656_6597	51.0	7.4	0.81	0.96	0.89	0.88	0.40 ± 0.05	$-0.51\pm^{+0.13}_{-0.31}$
47776_8604	30.6	-12.1	0.79	0.81	0.85	0.88	0.56 ± 0.11	$-0.50\pm^{+0.13}_{-0.28}$
48190_0905	19.3	-45.4	0.88	0.93	0.88	0.93	0.57 ± 0.07	$-0.51\pm^{+0.13}_{-0.31}$
48437_7361	12.0	-1.3	0.78	0.77	0.75	0.88	0.78 ± 0.13	$-0.68\pm^{+0.14}_{-0.34}$
48755_5033	15.7	-49.9	0.83	0.88	0.93	0.87	1.04 ± 0.07	$-0.77\pm^{+0.23}_{-0.44}$
49241_1211	17.7	-29.2	0.87	0.85	0.95	0.93	0.76 ± 0.08	$-0.61\pm^{+0.16}_{-0.40}$
49740_1802	27.0	-7.9	0.86	0.92	0.90	0.92	0.56 ± 0.07	$-0.56\pm^{+0.13}_{-0.32}$
51491_4209	11.0	-37.6	0.87	0.89	0.77	0.93	0.81 ± 0.06	$-0.75\pm^{+0.18}_{-0.50}$
53148_4421	21.6	12.8	0.83	0.80	0.79	0.88	0.73 ± 0.14	$-0.73\pm^{+0.14}_{-0.36}$
53794_5444	9.3	-10.9	0.85	0.83	0.79	0.94	0.59 ± 0.09	$-0.68\pm^{+0.14}_{-0.36}$
54618_8614	9.7	-24.7	0.89	0.95	0.95	0.94	0.67 ± 0.04	$-0.70\pm^{+0.16}_{-0.40}$

6.4.3 Zenithal Distributions

A total of 57 CR candidates were initially identified through the analysis pipeline. In order to compare with detection simulation, one reflected event and one below-horizontal

doi:10.6342/NTU202500216

event were excluded from this zenithal distributions analysis. For events exhibiting double pulses, only the main pulse was considered to ensure consistency in the dataset. These adjustments resulted in a final set of 55 CR candidates with zenith angles between 39° and 90°, which were included in the final analysis.

The expected cosmic ray event distributions for the TAROGE-4 station were modeled as functions of zenith angle across different energy ranges, assuming the Auger CR energy spectrum[130]. These modeled distributions account for the detection efficiency and environmental factors specific to the TAROGE-4 system. As illustrated in Fig. 6.8, the observed zenith angle distributions of UHECR events, depicted by markers with error bars, are compared with the expected distributions derived from simulations based on the Auger cosmic ray spectrum. The red curve represents the expected distribution under the pure proton assumption, while the black curve corresponds to the pure iron assumption. Additional details regarding the detection simulation can be found in Section5.

The strong agreement between the observed and simulated zenith-angle distributions underscores the effectiveness of TAROGE-4's detection system in capturing UHECR events. This consistency validates the robustness of the analysis and reconstruction methodologies applied to the dataset, affirming TAROGE-4's capability to accurately detect and characterize UHECR events.

doi:10.6342/NTU202500216

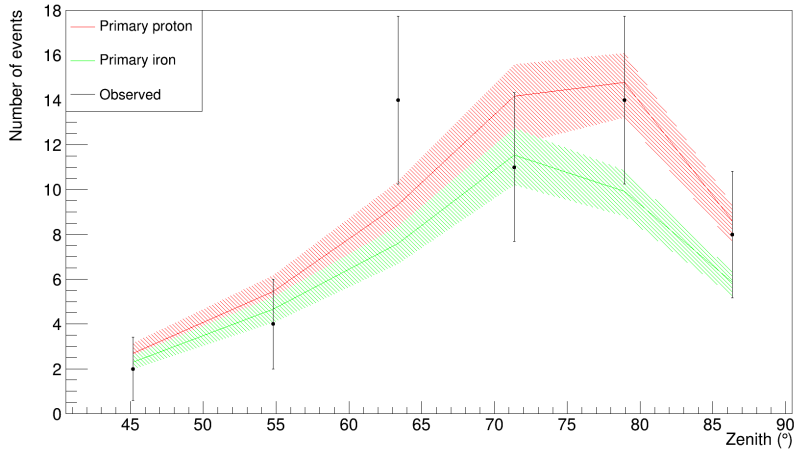

Figure 6.8: Observed zenith angle distributions of UHECR events, depicted by markers with error bars, are compared with the expected distributions derived from simulations based on the Auger cosmic ray spectrum. The red curve represents the expected distribution under the pure proton assumption, while the black curve corresponds to the pure iron assumption.

doi:10.6342/NTU202500216

Chapter 7 Characteristics of TAROGE-4 UHECR Events

To further verify the EAS origin of the 57 identified TAROGE-4 CR candidates, additional analyses were conducted beyond the angular distribution described in Section 6.4.3. These analyses examined key event properties, including polarization, polarity, spectral features, implied primary energies, and flux.

The polarization and polarity of the detected signals are particularly significant in event classification. Polarization provides information about the orientation of the electric field vector of the radio signal, which is directly related to the geomagnetic field's influence on the EAS. Polarity, on the other hand, offers clues about the directional relationship between the primary particle and the shower development.

The following sections will delve into the detailed analysis of these characteristics, demonstrating how they collectively validate the classification of TAROGE-4 UHECR events and enhance the understanding of their origins and properties.

doi:10.6342/NTU202500216

7.1 Ocean Reflected Event

For direct CR events, the RF signals should arrive from directions above the Earth's horizon ($\theta \sim -0.85°$), while reflected CR events typically arrive from below the horizon due to specular reflection off the ocean surface. A key characteristic of ocean-reflected events is the inversion of waveform polarity, caused by the reflection flipping the sign of the electric field.

Event 28891_9280 (Fig. 7.1) has been identified as an ocean-reflected CR event based on its reconstructed direction of $(\theta, \phi) = (-0.75°, 20°)$ and the observation of inverted polarity (phase inversion of both E_θ and E_ϕ waveforms). Although the reconstructed zenith angle of $-0.75°$ lies slightly above the Earth's horizon, this falls within the reconstruction error of approximately $0.8°$ at this angle. The observed polarity inversion in the waveform further confirms its reflection origin, as this is a unique signature of ocean-reflected events.

To confirm this classification, the electric field components (E_θ and E_ϕ) were analyzed and corrected using reflection coefficients derived from the Fresnel equations[93]. The reflection coefficients for parallel R_p and perpendicular R_s polarizations are given as:

$$R_p = \frac{n^2 \sin(\theta) - \sqrt{n^2 - \cos^2(\theta)}}{n^2 \sin(\theta) + \sqrt{n^2 - \cos^2(\theta)}}, \tag{7.1}$$

$$R_s = \frac{\sin(\theta) - \sqrt{n^2 - \cos^2(\theta)}}{\sin(\theta) + \sqrt{n^2 - \cos^2(\theta)}}, \tag{7.2}$$

where $n = \frac{n_{transmitted}}{n_{incident}}$ is the relative refractive index. For seawater, the complex

doi:10.6342/NTU202500216

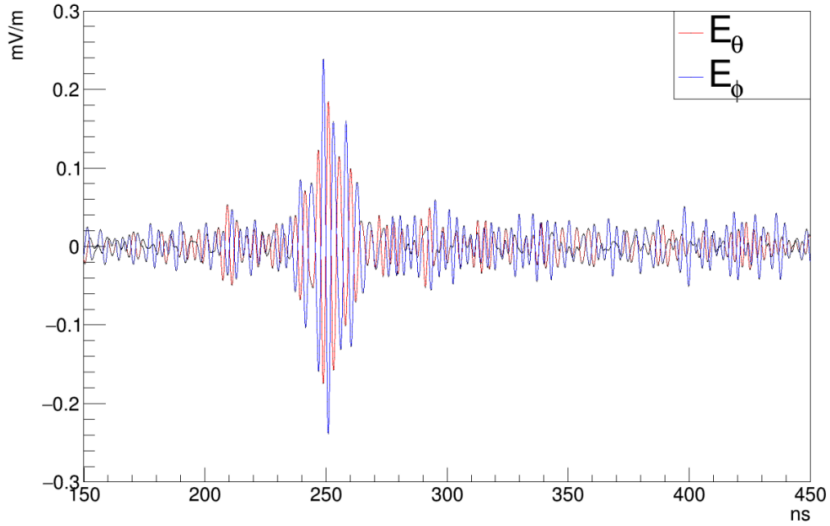

Figure 7.1: Ocean-reflected events, in contrast to other direct cosmic ray (CR) candidates, exhibit a distinct phase inversion in both E_θ and E_ϕ waveforms. This phase inversion arises from the reflection of radio signals off the ocean surface, which alters the signal's polarity due to the boundary conditions at the air-water interface.

refractive index $n_{transmitted}$ is calculated as:

$$n_{transmitted} = \sqrt{\frac{\epsilon}{\epsilon_0} - i\frac{\sigma}{\epsilon_0 \omega}}, \tag{7.3}$$

and $\frac{\epsilon}{\epsilon_0} = 81$ is the relative dielectric constant of seawater, $\sigma = 5\Omega^{-1}m^{-1}$ is the conductivity of seawater, and $\omega = 2\pi f$ is the angular frequency of the electromagnetic wave[123].

The Fresnel equations account for the angle of incidence and the refractive properties of seawater, which introduce both real and imaginary components to the refractive index. The real part determines the wave's phase velocity, while the imaginary part represents energy absorption in seawater. For this event, the reflection was assumed to be specular, meaning the angle of incidence equals the angle of reflection. Amplitude reflection coefficient versus grazing angle is shown in left of Fig. 7.2 while phase change versus grazing angle is in the right.

doi:10.6342/NTU202500216

After the correction, the corrected electric field components, E_θ and E_ϕ, confirmed the inversion of polarity. Furthermore, the expected ratio $\frac{E_\phi}{E_\theta}$ was restored from 1.25 to 0.5, which is consistent with the expected value of 0.5 ± 0.3.

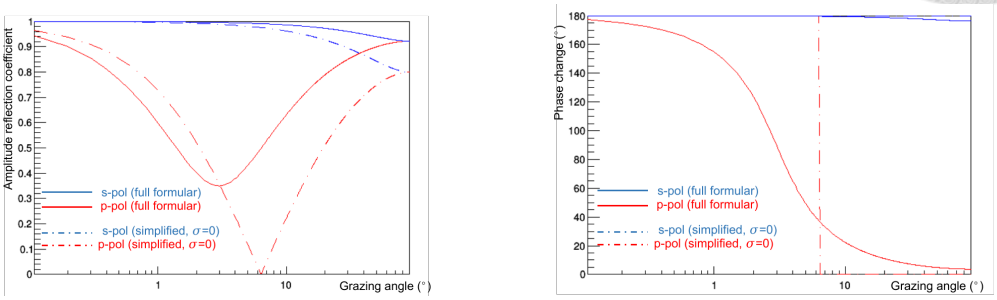

Figure 7.2: The magnitude (left) and phase (right) of the reflection coefficient as a function of the grazing angle for ocean reflection. The solid lines represent the more realistic case that accounts for the conductivity of seawater, while the dashed lines depict the simplified case where conductivity is not considered.

7.2 Double Pulses Events

Four double pulse events have been observed (11897_3658，16319_6029，40661_5357, 43598_5124), where the second pulse in each event has been identified as the ocean reflection of the first pulse. For the reflected pulses, the electric field component E_ϕ is larger than E_θ. This is attributed to the larger reflection coefficient for E_ϕ compared to E_θ, and possibly to the effects of ocean surface roughness, which impacts E_θ more significantly. Fig. 7.3, Fig. 7.4, Fig. 7.5 and Fig. 7.6 illustrate the deconvoluted coherent sum waveforms for these four events. On the left-hand side, the coherent sum is shown based on channel delays derived from the reconstruction direction of the main pulses, while on the right-hand side, the coherent sum corresponds to channel delays derived from the reconstruction direction of the second pulses. The time delays between the main pulses and the second pulses align well with the reconstructed angles of both pulses and the geometry of TAROGE-4.

doi:10.6342/NTU202500216

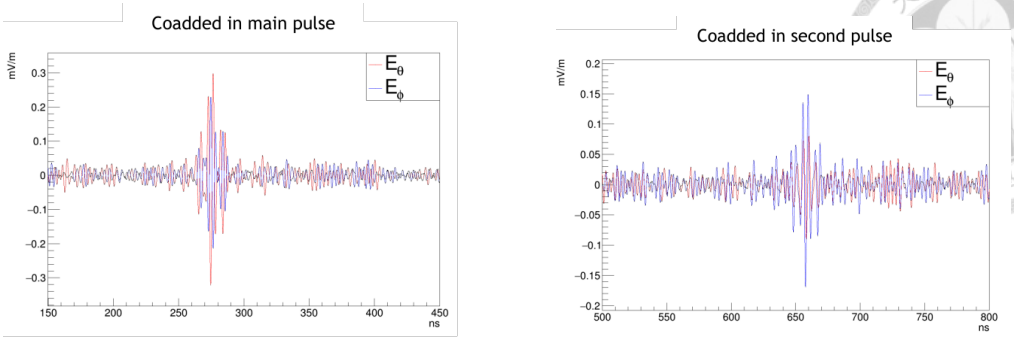

Figure 7.3: Double pulse CR candidate event 11897_3658. Similar to Fig. 7.4

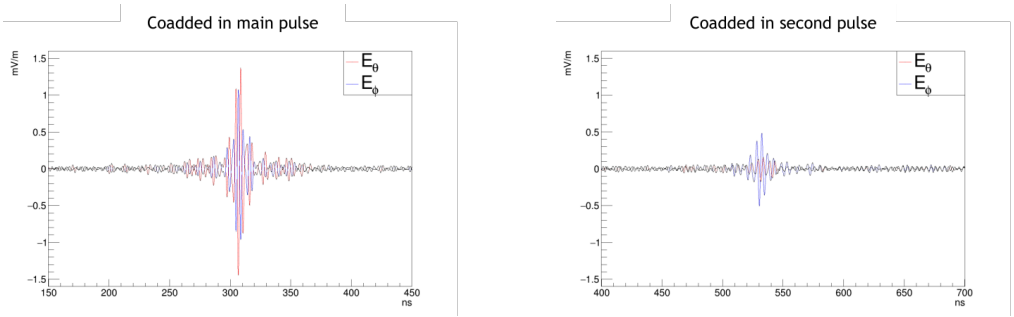

Figure 7.4: Double pulse CR candidate event 16319_6029. Left: Coherent sum based on channel delays from the main pulse reconstruction direction. Right: Coherent sum based on channel delays from the second pulse reconstruction direction.

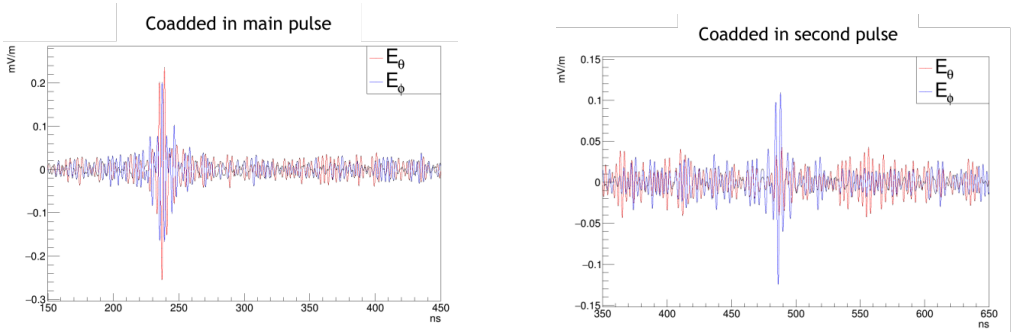

Figure 7.5: Double pulse CR candidate event 40661_5357. Similar to Fig. 7.4

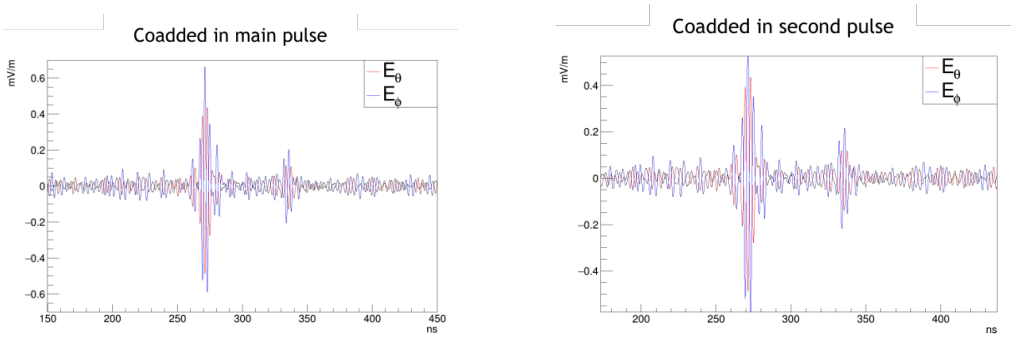

Figure 7.6: Double pulse CR candidate event 43598_5124. Similar to Fig. 7.4

doi:10.6342/NTU202500216

7.2.1 Shower Maximum Estimation

To further analyze these events, a χ^2 fitting method was implemented to determine the X_{max} location of the air showers, assuming that the radio emission originates from point sources located at $X_{\max}$[71]. The fitting takes into account the delays between channels for the main pulses, the second pulses, and the delays between the two pulses. The fitting formula is as follows:

$$\chi^2 = \sum_{i=0}^{6} \frac{\left(\Delta t^{\text{expt.}}_{DH,i}(\theta,\phi,R) - \Delta t^{\text{meas.}}_{DH,i}\right)^2}{\sigma^2_{DH,i}} + \sum_{i=0}^{6} \frac{\left(\Delta t^{\text{expt.}}_{DV,i}(\theta,\phi,R) - \Delta t^{\text{meas.}}_{DV,i}\right)^2}{\sigma^2_{DV,i}} + \sum_{i=0}^{6} \frac{\left(\Delta t^{\text{expt.}}_{RH,i}(\theta,\phi,R,h) - \Delta t^{\text{meas.}}_{RH,i}\right)^2}{\sigma^2_{RH,i}} + \sum_{i=0}^{4} \frac{\left(\Delta t^{\text{expt.}}_{DRH,i}(\theta,\phi,R,h) - \Delta t^{\text{meas.}}_{DRH,i}\right)^2}{\sigma^2_{DRH,i}} \tag{7.4}$$

Here, $\Delta t^{expt.}_{DH,i}$ represents the expected time delay between antennas for the direct H-polarized signal, $\Delta t^{expt.}_{DV,i}$ is the expected time delay for the direct V-polarized signal, $\Delta t^{expt.}_{RH,i}$ is the expected time delay for the reflected H-polarized signal, and $\Delta t^{expt.}_{DRH,i}$ represents the expected time delay between the direct and reflected H-polarized signals. The parameters θ, ϕ, R, and h represent the elevation angle, azimuth angle, distance from the signal source to TAROGE-4, and the altitude of TAROGE-4, respectively.

The fitting results are presented in Fig. 7.7, where the y-axis shows the distance from the X_{max} location to TAROGE-4, and the x-axis represents the elevation angle. If the second pulses were not reflections of the main pulses, the reduced χ^2 value would be significantly larger than 1, rather than close to 1 as observed. However, due to uncertainties in the elevation angles θ, the possible distance from X_{max} to TAROGE-4 ranges from approximately $50\ km$ to over $500\ km$. Comparisons with CoREAS simulations suggest that the expected distances for these four events should range between $200\ km$ and $400\ km$.

doi:10.6342/NTU202500216

Despite the large uncertainties, the fitting results are consistent with these expectations.

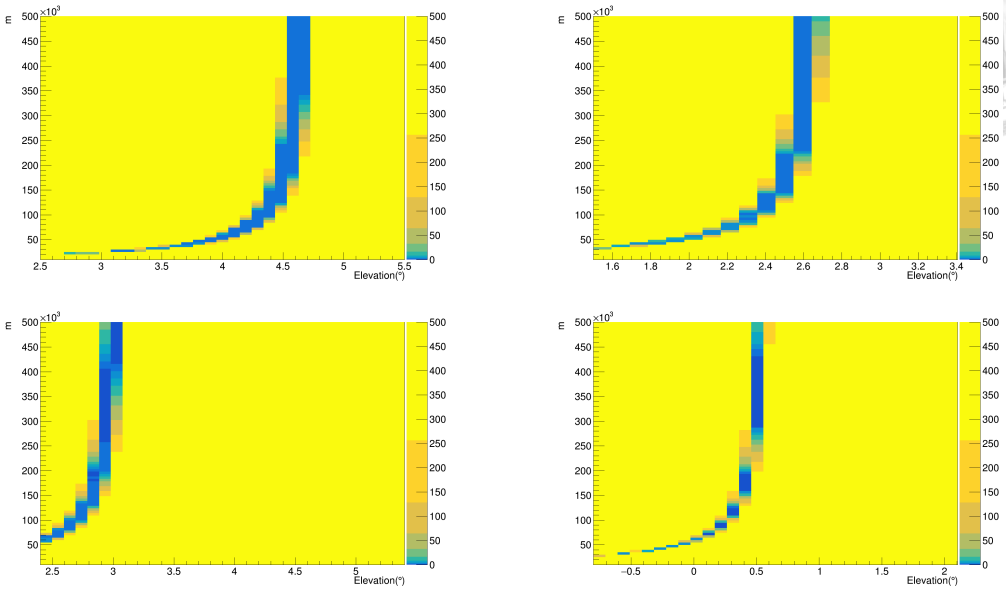

Figure 7.7: χ^2 fitting of the double pulse events: 11897_3658，16319_6029，40661_5357, 43598_5124, shown in order from left to right and top to bottom.

7.3 Polarization Measurement

The polarization of an event in TAROGE-4 is defined as the ratio of H-pol to V-pol signal amplitudes. This ratio provides a measure of the signal's polarization angle, which is a key parameter in identifying the origin and nature of the detected radio signal. The signal amplitude for each polarization is derived from the integrated power of the coherently-summed waveforms within a specified signal time window. The calculation of power is performed after deconvolution of the receiver response.

The signal window was selected to be 60 ns around the waveform's amplitude peak to ensure optimal signal capture. The power $V^2_{\mathrm{rms},s}$ of the signal in this window is calculated as:

$$V^2_{\mathrm{rms},s} = \frac{1}{N_s} \sum_{n=p-L_1}^{p+L_2} w[n]^2, \tag{7.5}$$

doi:10.6342/NTU202500216

where L_1 and L_2 are the number of samples corresponding to the start and end of the signal window, p is the sample index of the amplitude peak, and $w[n]$ is the waveform value at sample n. The noise power $V^2_{\text{rms},n}$ is estimated using the last $400\,\text{ns}$ of the waveform, where the signal is assumed to have diminished:

$$V^2_{\text{rms},n} = \frac{1}{N_n} \sum_{n=N-N_n}^{N-1} w[n]^2, \tag{7.6}$$

where N_n is the number of noise samples, and N is the total number of samples in the waveform. For some events with impulsive noise contamination, the noise window is manually adjusted to avoid bias.

The H-pol to V-pol amplitude ratio, or the tangent of the polarization angle, is calculated as:

$$\tan\epsilon = \frac{E_\phi}{E_\theta} \approx \frac{\sqrt{V^2_{\text{rms},s,H} - V^2_{\text{rms},n,H}}}{\sqrt{V^2_{\text{rms},s,V} - V^2_{\text{rms},n,V}}}. \tag{7.7}$$

This calculation does not include systematic uncertainty in the antenna gain, as it is well-calibrated in TAROGE-4. Statistical uncertainty due to noise fluctuations within the finite signal window is estimated as $\hat{V}_{n,\text{rms}}/\sqrt{2(N_s-1)}$, where $\hat{V}_{n,\text{rms}}$ is the measured noise RMS voltage. The uncertainty of the polarization measurement is computed solely from statistical fluctuations. In TAROGE-4, the secondary contribution from Askaryan radiation is non-negligible and accounts for 10% to 20% of the total signal, depending on the incident angles[15].

Polarization measurements for 57 candidate events were compared to theoretical expectations. The dominant geomagnetic emission determines the expected polarization direction, aligned with $\vec{v} \times \vec{B}$, with corrections applied for ocean-reflected events based

doi:10.6342/NTU202500216

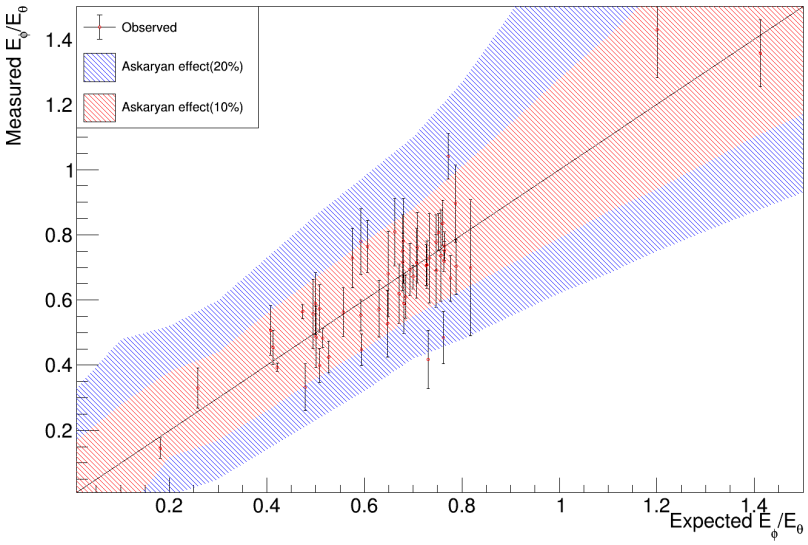

Figure 7.8: proton

on the reflection coefficients calculated using the Fresnel equations as described in the previous section. The measured and expected polarization values show good agreement, as depicted in Fig. 7.8. This agreement further supports the identification of the events as originating from geomagnetic emission with a secondary contribution from Askaryan radiation.

7.4 Energy Estimation

For a compact and standalone antenna array like TAROGE-4, with antenna spacing of less than 30 meters, the primary energy of a detected cosmic ray event is estimated based on the information encoded in the signal sampled at a single spot of the radio footprint on the ground. This approach contrasts with large-scale arrays such as LOFAR and AERA, which broadly sample the radio footprint and fit its profile to derive energy and depth of the shower maximum[81, 129]. EAS signals typically exhibit maximum power below 100 MHz and a progressively decreasing spectrum at higher frequencies. The slope of

doi:10.6342/NTU202500216

this spectrum, along with the frequency of peak power, depends on the distance between the observer and the Cherenkov cone. At the Cherenkov cone, coherence across all frequencies results in the flattest spectral slope. This cone's position relative to the shower axis is influenced by the geometry of the air shower, particularly the height of the shower maximum. The total power in the signal also depends on the distance to the shower axis; however, at a fixed distance from the Cherenkov cone, the signal amplitude scales linearly with the shower energy on average. By leveraging this relationship, TAROGE-4 applies a methodology adapted from ANITA, ARIANNA, and TAROGE-M [25, 113, 135], fitting the electric field amplitude spectrum $A(f)$ to an exponential form or its equivalent linear representation in logarithmic scale.

$$A(f) = A_{200} e^{\gamma(f - 200\,\mathrm{MHz})}, \tag{7.8}$$

$$\log_{10} A(f) = \log_{10} A_{200} + \gamma(f - 200\,\mathrm{MHz}), \tag{7.9}$$

where γ is the spectral slope (typically negative), and $\log_{10} A_{200}$ is the amplitude intercept at $200\ MHz$, chosen to match TAROGE-4' s bandwidth. The frequency range for spectrum fitting in TAROGE-4 is 180–350 MHz, excluding frequency bands filtered out by the constant CW filtering and dynamic filtering algorithm.

The radio emission of air showers is most coherent in directions corresponding to the Cherenkov ring, defined by the Cherenkov angle $\psi_c$from the shower axis. At these angles, the radiation from different parts of the shower arrives almost simultaneously, resulting in a flatter spectrum with a higher slope γ and amplitude intercept $\log_{10} A_{200}$. Observing further off-Cherenkov angles $\psi - \psi_c$ leads to a decline in coherence, resulting in a steeper spectrum with lower slope and intercept. This behavior allows the primary energy and

doi:10.6342/NTU202500216

the off-Cherenkov angle of the observer to be decoupled and measured using the spectral parameters.

7.4.1 Energy Parametrization Techniques

To estimate the energy of each cosmic ray event, proton- and iron-induced air showers were simulated at reconstructed directions $(\tilde{\theta}, \tilde{\phi})$. Showers were simulated for primary energies spanning $\log E = 17.5$ to $\log E = 19.5$ in increments of 0.25.

At the Cherenkov angle ψ_c, the amplitude intercept $\log_{10} A_{200,c}$ was found to be proportional to the primary energy of the shower:

$$\log_{10} A_{200,c} = p_0 + p_1 \log_{10} E, \tag{7.10}$$

where p_0 and p_1 are fitting parameters. This relationship was verified to be linear ($p_1 \approx 1$) within a 10% error margin for all shower directions. The slope γ near the Cherenkov cone encodes information about the coherence conditions and contributes to refining the energy estimation.

The spectral intercept and slope $(\log_{10} A_{200}, \gamma)$ also exhibited a linear relationship near the Cherenkov angle:

$$\log_{10} A_{200} = \log_{10} A_{200,c} + m(\gamma - \gamma_c), \tag{7.11}$$

where γ_c is the spectral slope at the Cherenkov angle, and m is the slope parameter. These relationships form the foundation of TAROGE-4's energy parameterization, with simulations providing the calibration for interpreting measured spectra.

doi:10.6342/NTU202500216

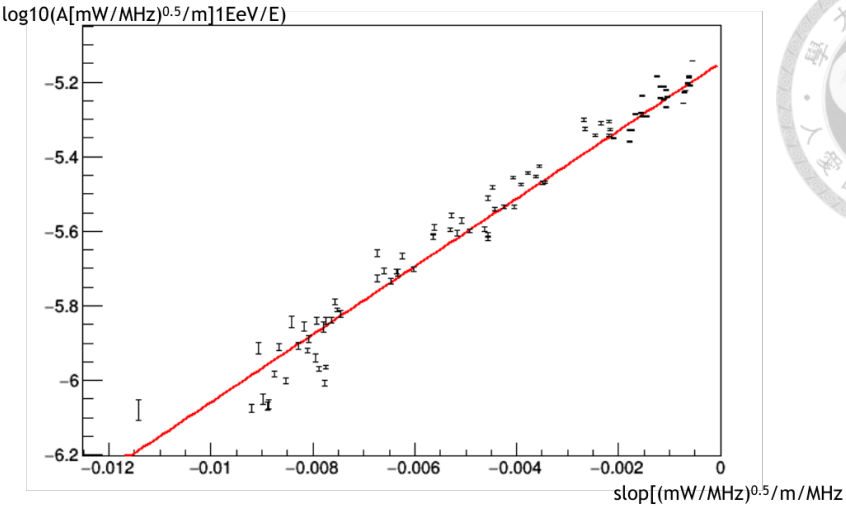

Figure 7.9: Distribution of spectral slope versus energy-normalized intercept (to $1\ EeV$) for simulated proton showers coming from the same direction. The red line show the global linear fit.

Fig.7.9 shows the distribution and linear fit of spectral slope versus energy-normalized intercept (to $1\ EeV$) for simulated proton showers coming from the same direction as an example. For more detailed of this parametrization techniques, please refer to [134].

7.4.2 Fitting CR Events Spectrum

For the 57 identified CR candidate events, the filtered and deconvolved $E_\theta$and E_ϕ coherent summed waveforms were Fourier-transformed to amplitude spectra. The resulting amplitude spectra of the incoming electric field were obtained by squaring the $E_\theta$and E_ϕ spectra, summing them, and then taking the square root. Among these candidates, one event was identified as an ocean-reflected event. For this event, the $E_\theta$and E_ϕ components were corrected using ocean reflection coefficients calculated from the Fresnel equations. The spectrum was averaged over $\sim 17\ MHz$ bins, with the RMS value in each bin added in quadrature to estimate statistical uncertainties.

Building on the simulation results, TAROGE-4 estimates the primary energy of cos-

doi:10.6342/NTU202500216

mic rays using the following relation:

$$\log_{10} E = \frac{\log_{10} A_{200} - p_0 - m(\gamma - \gamma_c)}{p_1}. \tag{7.12}$$

This method combines the spectral slope and amplitude intercept to decouple energy from other shower properties. The uncertainties in $\log_{10} A_{200}$, γ, and simulation parameters p_0, p_1, m, γ_c were propagated to compute the total energy uncertainty. Contributions from antenna response, signal polarization, and thermal noise were incorporated into the uncertainty analysis. The fitting parameters, slope and intercept, of all 57 CR candidates are shown in Table 7.1;

Table 7.1: Fitting parameters and estimated energies of CR candidates.

Event #	Slope	Intercept	Est. E (proton)	Est. E (iron)
02131_9340	-0.000903 ± 0.000802	-4.69 ± 0.37	18.10 ± 0.29	18.13 ± 0.27
02329_4570	-0.001277 ± 0.001746	-5.03 ± 0.81	17.91 ± 0.57	17.99 ± 0.60
03561_9374	-0.002288 ± 0.001383	-4.88 ± 0.62	18.49 ± 0.38	18.52 ± 0.38
03831_7180	-0.001339 ± 0.001094	-4.84 ± 0.50	18.37 ± 0.35	18.35 ± 0.30
04085_3887	0.0003787 ± 0.001821	-5.32 ± 0.86	17.72 ± 0.55	17.74 ± 0.54
04441_0902	-0.002229 ± 0.000212	-4.25 ± 0.09	18.92 ± 0.09	18.92 ± 0.09
06868_7207	-0.000583 ± 0.000780	-5.11 ± 0.35	17.99 ± 0.22	18.08 ± 0.22
06916_0628	-0.000571 ± 0.001998	-5.23 ± 0.93	17.58 ± 0.64	17.64 ± 0.63
07214_2950	-0.001318 ± 0.001931	-5.03 ± 0.88	17.76 ± 0.65	17.82 ± 0.66
09653_2472	-0.001836 ± 0.000562	-4.83 ± 0.24	18.48 ± 0.15	18.57 ± 0.15
11351_0109	-0.001588 ± 0.002217	-4.86 ± 1.04	18.91 ± 0.83	19.14 ± 0.60
11897_3658	-0.000420 ± 0.001360	-5.15 ± 0.64	18.23 ± 0.41	18.34 ± 0.43
13379_7040	-0.000805 ± 0.001123	-5.04 ± 0.52	18.09 ± 0.33	18.15 ± 0.34
13837_2723	-0.001679 ± 0.001198	-4.93 ± 0.55	18.06 ± 0.37	18.08 ± 0.37
14052_4962	0.0007198 ± 0.001002	-5.27 ± 0.47	18.25 ± 0.33	18.30 ± 0.32
14745_0254	-0.001051 ± 0.001960	-5.09 ± 0.90	17.70 ± 0.63	17.74 ± 0.61
16319_6029	-0.002566 ± 0.000715	-4.49 ± 0.33	19.32 ± 0.27	19.39 ± 0.22

doi:10.6342/NTU202500216

Event #	Slope	Intercept	Est. E (proton)	Est. E (iron)
16489_4481	-0.002430 ± 0.001348	-4.80 ± 0.62	18.62 ± 0.39	18.68 ± 0.38
16523_5369	-0.004254 ± 0.000609	-4.55 ± 0.27	19.01 ± 0.20	18.87 ± 0.20
16628_7515	-0.000904 ± 0.001523	-5.10 ± 0.70	17.97 ± 0.44	18.00 ± 0.43
17782_5664	-0.000358 ± 0.001866	-5.18 ± 0.87	17.77 ± 0.55	17.82 ± 0.53
17931_4479	-0.000009 ± 0.001690	-5.35 ± 0.79	17.71 ± 0.60	17.58 ± 0.50
19019_0666	-0.001123 ± 0.001653	-5.13 ± 0.77	18.20 ± 0.48	18.27 ± 0.48
20487_0996	-0.000134 ± 0.001383	-5.29 ± 0.62	17.35 ± 0.45	17.41 ± 0.44
21455_1082	-0.001011 ± 0.000482	-4.65 ± 0.22	18.59 ± 0.14	18.67 ± 0.15
27460_6479	-0.001938 ± 0.001796	-5.12 ± 0.83	17.95 ± 0.51	18.02 ± 0.51
27802_2184	-0.000532 ± 0.001480	-5.09 ± 0.68	17.68 ± 0.46	17.73 ± 0.45
28891_9280	-0.002746 ± 0.001673	-5.02 ± 0.78	19.09 ± 0.62	18.98 ± 0.44
29653_4385	-0.001782 ± 0.001265	-5.01 ± 0.59	18.16 ± 0.36	18.26 ± 0.36
31621_7622	-0.001732 ± 0.000721	-4.96 ± 0.32	18.86 ± 0.25	18.95 ± 0.24
32085_1672	-0.000411 ± 0.000771	-5.07 ± 0.35	17.94 ± 0.23	17.98 ± 0.23
33702_9219	-0.001596 ± 0.001538	-5.06 ± 0.70	18.09 ± 0.52	18.08 ± 0.49
38208_3709	0.0002840 ± 0.000931	-5.12 ± 0.43	17.64 ± 0.28	17.68 ± 0.28
38955_2812	-0.001966 ± 0.001491	-4.83 ± 0.70	18.19 ± 0.52	18.14 ± 0.48
40661_5357	-0.001939 ± 0.002656	-5.19 ± 1.19	18.54 ± 0.76	18.61 ± 0.76
42337_4989	-0.000195 ± 0.001133	-5.28 ± 0.52	17.50 ± 0.34	17.55 ± 0.33
43272_5426	-0.001916 ± 0.001265	-4.95 ± 0.58	18.17 ± 0.36	18.24 ± 0.36
43347_7075	-0.001333 ± 0.001910	-5.14 ± 0.89	17.77 ± 0.66	17.63 ± 0.57
43598_5124	-0.001323 ± 0.001461	-4.87 ± 0.69	19.19 ± 0.61	19.18 ± 0.63
43631_4175	-0.002031 ± 0.000973	-4.74 ± 0.45	18.29 ± 0.33	18.24 ± 0.30
43654_6513	-0.001329 ± 0.000913	-4.95 ± 0.41	17.85 ± 0.33	17.89 ± 0.31
44774_7894	-0.001922 ± 0.002103	-5.07 ± 0.99	18.09 ± 0.64	18.06 ± 0.61
45853_8910	-0.001518 ± 0.001310	-5.01 ± 0.61	17.97 ± 0.48	17.95 ± 0.46
46102_1355	-0.000880 ± 0.001437	-5.02 ± 0.65	17.70 ± 0.38	17.77 ± 0.40
46192_3233	-0.001378 ± 0.001724	-5.16 ± 0.80	18.15 ± 0.65	17.86 ± 0.50
46456_6689	-0.000031 ± 0.002026	-4.80 ± 0.93	17.71 ± 0.57	17.71 ± 0.58
47656_6597	-0.001515 ± 0.001887	-4.72 ± 0.87	18.21 ± 0.80	17.90 ± 0.54

doi:10.6342/NTU202500216

Event #	Slope	Intercept	Est. E (proton)	Est. E (iron)
47776_8604	-0.002447 ± 0.003662	-5.08 ± 1.71	18.03 ± 1.22	17.87 ± 1.12
48190_0905	-0.000919 ± 0.001454	-5.13 ± 0.68	17.91 ± 0.46	17.90 ± 0.44
48437_7361	-0.001479 ± 0.001909	-5.21 ± 0.89	17.85 ± 0.56	17.93 ± 0.55
48755_5033	-0.003154 ± 0.000941	-4.64 ± 0.43	19.21 ± 0.52	18.66 ± 0.27
49241_1211	-0.001173 ± 0.001542	-5.10 ± 0.71	18.36 ± 0.68	17.91 ± 0.45
49740_1802	-0.001087 ± 0.001153	-5.08 ± 0.51	17.77 ± 0.37	17.86 ± 0.32
51491_4209	-0.000919 ± 0.000602	-5.00 ± 0.27	18.10 ± 0.17	18.15 ± 0.18
53148_4421	0.0009162 ± 0.001047	-5.20 ± 0.49	17.49 ± 0.33	17.54 ± 0.32
53794_5444	-0.001060 ± 0.001025	-5.24 ± 0.46	17.89 ± 0.29	17.97 ± 0.29
54618_8614	-0.001238 ± 0.000588	-4.94 ± 0.26	18.22 ± 0.17	18.27 ± 0.17

7.4.3 Observed Energy Distribution

The primary energies of the 57 CR candidate events were estimated using Eq. 7.12, with the logarithmic energy values ($log\ E$) summarized in Table 7.1. Overall, the estimated energy uncertainties, $\Delta(\log E)$, are approximately 0.44 for the pure proton assumption and 0.41 for the pure iron assumption. These uncertainties are likely slightly overestimated, as the Monte Carlo simulation dataset indicates a lower uncertainty of $\Delta(\log E) \approx 0.25$, as shown in Fig. 7.10.

To facilitate a meaningful comparison with detection simulations, specific adjustments were made to the dataset. One reflected event and one below-horizontal event were excluded from the zenith angle distribution analysis. Additionally, for events exhibiting double pulses, only the main pulse was included to maintain uniformity. These adjustments yielded a refined set of 55 CR candidates with zenith angles ranging from $30°$ to $90°$.

doi:10.6342/NTU202500216

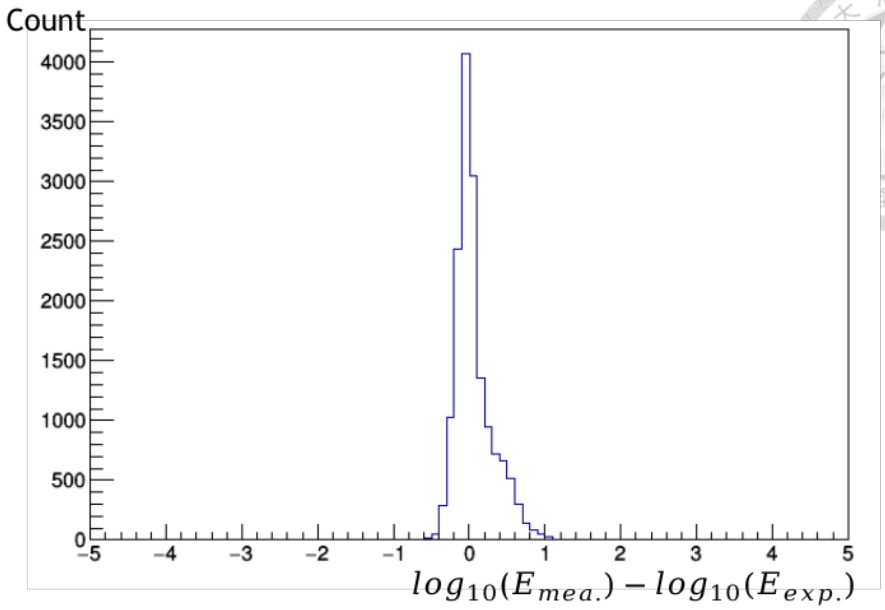

Figure 7.10: Energy resolution for MC simulated events, showing an uncertainty of $\Delta(\log E) \approx 0.25$.

Fig. 7.11 shows the resulting energy distribution alongside detection simulations. The left panel represents the results under the pure proton assumption, while the right panel assumes pure iron composition. In both cases, the observed energy distributions align well with the simulations, indicating consistency between the observed events and theoretical models for cosmic ray detection.

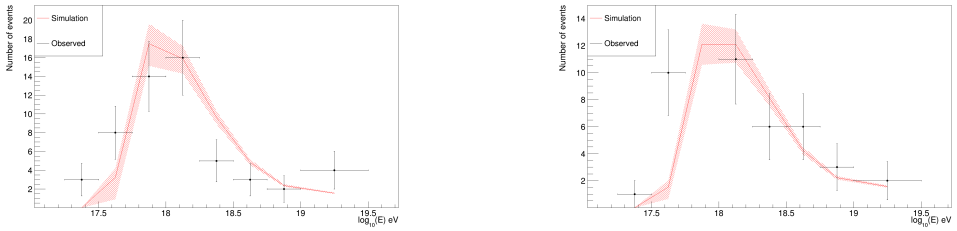

Figure 7.11: The energy distribution alongside detection simulations. The left panel represents the results under the pure proton assumption, while the right panel assumes pure iron composition. In both cases, the observed energy distributions align well with the simulations, indicating consistency between the observed events and theoretical models for cosmic ray detection.

doi:10.6342/NTU202500216

7.5 Flux Measurement

The cosmic ray flux for TAROGE-4 is calculated based on $N_{CR} = 55 \pm 7.4$ detected events (statistical error only), excluding one ocean-reflected event and one below-horizontal event to ensure consistency in the dataset. These detections were recorded over a total livetime of $T_{live} = 2.3\ years$, after excluding periods affected by lightning activity and temporal clustering. Simulations provided the livetime-weighted average cosmic ray acceptance (Fig. 5.4, Fig. 5.5) and analysis efficiency, $\eta(E)$, which were critical for deriving the flux.

The differential cosmic ray flux is defined as the number of particles per unit energy, per unit solid angle, passing through a unit area perpendicular to the direction, per unit time:

$$\Phi(E) = \frac{dN}{dt dA d\Omega dE} = \frac{dN}{dt dA d\Omega \cdot E \ln 10\, d(\log_{10} E)}, \tag{7.13}$$

where the second form arises from the relation $d\log_{10} E = \frac{dE}{E \ln 10}$. This formulation allows the acceptance area, evaluated in logarithmic energy bins through simulations, to be directly incorporated into the flux calculation.

To estimate the flux at the mean energy, a model-dependent approach is employed, assuming the cosmic ray spectrum follows a piece-wise power law inside each energy bin:

$$\Phi(E) = \Phi(\langle E \rangle) \left(\frac{E}{\langle E \rangle} \right)^{\alpha}, \tag{7.14}$$

where α represents the spectral index, changing with energy, obtained from the Auger cosmic ray spectrum. This approach transforms the infinitesimal parameters in the differ-

doi:10.6342/NTU202500216

ential flux equation into finite terms while considering the energy dependence of cosmic ray acceptance over the energy interval $\log E = 17.25$ to 19.5. The flux at the mean energy is computed as:

$$\Phi(\langle E \rangle) \approx \frac{N_{\mathrm{CR}}/\eta(\langle E \rangle)}{T_{\mathrm{live}} \cdot \int \langle E \rangle^{-\alpha} \langle A\Omega \rangle(E) \cdot E^{\alpha}\, dE}. \tag{7.15}$$

Here, $\eta(\langle E \rangle)$ varies for each energy bin, and the energy dependence of the acceptance is integrated to provide a realistic estimate of the flux.

The resulting cosmic ray flux values are consistent with the energy spectra reported by other experiments, including the Auger Observatory, and match results from radio-based experiments like ANITA, ARIANNA, and TAROGE-M, which employed similar methods. Fig. 7.12 presents a comparison of the flux estimation results, with the left panel showing estimates under the assumption of pure proton composition and the right panel under pure iron composition. In both cases, the observed flux aligns well with predictions, demonstrating the robustness of the TAROGE-4 flux measurements and confirming its reliability in detecting and analyzing UHECRs.

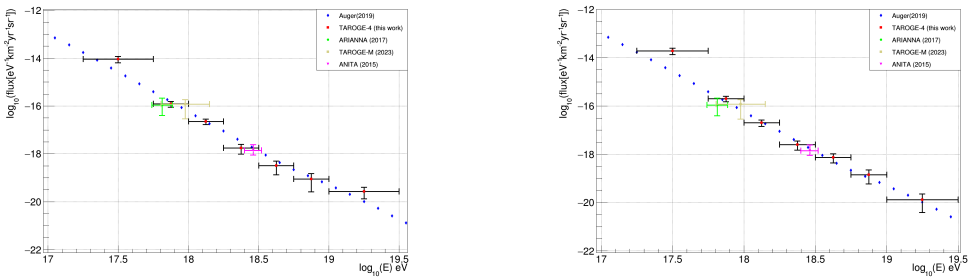

Figure 7.12: Comparison of the flux estimation results, with the left panel showing estimates under the assumption of pure proton composition and the right panel under pure iron composition.

doi:10.6342/NTU202500216

Chapter 8 Conclusion and Discussion

The detection of UHE particles is critical for advancing our understanding of fundamental physics and exploring phenomena beyond the Standard Model. These particles provide unique insights into high-energy astrophysical processes and offer opportunities to probe new physics at extreme energy scales.

The deployment of radio antenna arrays on high mountains, such as TAROGE-4, has proven to be an effective method for detecting UHE particles, particularly those arriving from near-horizontal directions. This approach takes advantage of the altitude and geometry of the mountain environment, allowing precise detection of EAS induced by UHECRs and UHECNs. TAROGE-4 has demonstrated remarkable sensitivity to EAS impulses, even in the challenging noise environment of suburban areas, and achieves sub-degree angular resolution, enabling high-precision event localization and robust noise rejection.

Despite its successes, TAROGE-4 faced challenges in achieving its full potential. The station's duty cycle was below expectations due to adverse weather conditions and insufficient maintenance. These issues, compounded by limited power resources such as batteries and photovoltaic (PV) panels, significantly reduced the station's operational time. Additionally, the analysis efficiency of approximately 53% left room for improvement, limiting the ability to maximize the station's detection capability.

doi:10.6342/NTU202500216

If the duty cycle could be increased to near 100%, this would dramatically enhance TAROGE-4's performance. Achieving this level of operation would require more frequent maintenance and the installation of additional batteries and PV panels to ensure continuous power availability, even under unfavorable weather conditions. Moreover, improving the analysis efficiency to over 80% (potentially through the application of advanced techniques such as machine learning) would allow for more effective noise rejection and event classification.

Looking further ahead, the adoption of cutting-edge technologies like phased-array triggers implemented via RFSoC would enable TAROGE-4 to achieve significantly higher detection rates. With these technological advancements, TAROGE-4 could achieve detection rates exceeding 100 UHECR candidates annually, representing a significant leap from its current capabilities. Such improvements would not only enhance the station's scientific output but also establish TAROGE-4 as one of the most efficient and compact detectors for UHE particle research. The ability to operate with high sensitivity and reliability in a small-scale setup would make TAROGE-4 an attractive model for future observatories, offering a scalable and cost-effective solution for expanding global UHE particle detection networks.

During its current operational period, TAROGE-4 successfully detected a total of 57 UHECR candidate events, including:

- **52 direct CR candidates**,
- **1 ocean reflection CR candidate**, and
- **4 candidates with both direct and reflected signals**.

doi:10.6342/NTU202500216

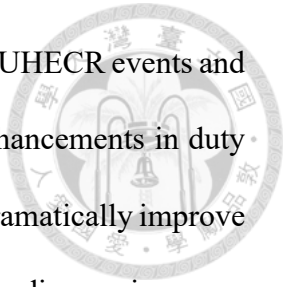

These results highlight TAROGE-4's effectiveness in identifying UHECR events and validating its classification pipeline. However, with the proposed enhancements in duty cycle, analysis efficiency, and trigger technology, TAROGE-4 could dramatically improve its detection capacity, unlocking new opportunities for groundbreaking discoveries.

In conclusion, while TAROGE-4 has already demonstrated its capability as a UHE particle detector, its potential for future improvement is immense. By addressing current limitations and incorporating advanced technologies, TAROGE-4 can become a key player in detecting tau neutrinos, exploring anomalous events like those observed by ANITA, and pushing the boundaries of high-energy astrophysics. This evolution would not only amplify the station's scientific contributions but also reinforce the promise of high-mountain radio arrays as pivotal tools in the quest to understand the high-energy universe.

doi:10.6342/NTU202500216

doi:10.6342/NTU202500216

References

[1] The Standard Model — home.cern. https://home.cern/science/physics/standard-model. [Accessed 01-01-2025].

[2] A. Aab, P. Abreu, M. Aglietta, M. Ahlers, E.-J. Ahn, I. Albuquerque, I. Allekotte, J. Allen, P. Allison, A. Almela, et al. Probing the radio emission from air showers with polarization measurements. Physical Review D, 89(5):052002, 2014.

[3] G. Aad, T. Abajyan, B. Abbott, J. Abdallah, S. A. Khalek, A. A. Abdelalim, R. Aben, B. Abi, M. Abolins, O. AbouZeid, et al. Observation of a new particle in the search for the standard model higgs boson with the atlas detector at the lhc. Physics Letters B, 716(1):1–29, 2012.

[4] M. Aartsen, M. Ackermann, J. Adams, J. Aguilar, M. Ahlers, M. Ahrens, C. Alispach, K. Andeen, T. Anderson, I. Ansseau, et al. A search for icecube events in the direction of anita neutrino candidates. The Astrophysical Journal, 892(1):53, 2020.

[5] M. G. Aartsen, M. Ackermann, J. Adams, J. Aguilar, M. Ahlers, M. Ahrens, D. Altmann, T. Anderson, G. Anton, C. Arguelles, et al. Icecube-gen2: a vision for the future of neutrino astronomy in antarctica. arXiv preprint arXiv:1412.5106, 2014.

[6] Q. Abarr, P. Allison, J. A. Yebra, J. Alvarez-Muñiz, J. Beatty, D. Besson, P. Chen,

doi:10.6342/NTU202500216

Y. Chen, C. Xie, J. Clem, et al. The payload for ultrahigh energy observations (pueo): a white paper. Journal of Instrumentation, 16(08):P08035, 2021.

[7] R. Abbasi, Y. Abe, T. Abu-Zayyad, M. Allen, Y. Arai, R. Arimura, E. Barcikowski, J. Belz, D. Bergman, S. Blake, et al. The energy spectrum of cosmic rays measured by the telescope array using 10 years of fluorescence detector data. Astroparticle Physics, 151:102864, 2023.

[8] M. Ackermann, M. Bustamante, L. Lu, N. Otte, M. H. Reno, S. Wissel, S. K. Agarwalla, J. Alvarez-Muñiz, R. A. Batista, C. A. Argüelles, et al. High-energy and ultra-high-energy neutrinos: A snowmass white paper. Journal of high energy astrophysics, 36:55–110, 2022.

[9] A. Addazi, J. Alvarez-Muniz, R. A. Batista, G. Amelino-Camelia, V. Antonelli, M. Arzano, M. Asorey, J.-L. Atteia, S. Bahamonde, F. Bajardi, et al. Quantum gravity phenomenology at the dawn of the multi-messenger era—a review. Progress in Particle and Nuclear Physics, 125:103948, 2022.

[10] N. Agafonova, A. Alexandrov, A. Anokhina, S. Aoki, A. Ariga, T. Ariga, A. Bertolin, C. Bozza, R. Brugnera, A. Buonaura, et al. Opera tau neutrino charged current interactions. Scientific data, 8(1):218, 2021.

[11] M. Ahlers and F. Halzen. Opening a new window onto the universe with icecube. Progress in Particle and Nuclear Physics, 102:73–88, 2018.

[12] P. Allison, J. Auffenberg, R. Bard, J. Beatty, D. Besson, S. Böser, C. Chen, P. Chen, A. Connolly, J. Davies, et al. Design and initial performance of the askaryan radio array prototype eev neutrino detector at the south pole. Astroparticle physics, 35(7):457–477, 2012.

doi:10.6342/NTU202500216

[13] R. Aloisio et al. Ultra high energy cosmic rays propagation and spectrum. In AIP CONFERENCE PROCEEDINGS, 2011.

[14] J. Alvarez-Muniz, R. Alves Batista, A. Balagopal V, J. Bolmont, M. Bustamante, W. Carvalho Jr, D. Charrier, I. Cognard, V. Decoene, P. B. Denton, et al. The giant radio array for neutrino detection (grand): science and design. Science China Physics, Mechanics & Astronomy, 63(1):219501, 2020.

[15] J. Alvarez-Muñiz, W. R. Carvalho Jr, H. Schoorlemmer, and E. Zas. Radio pulses from ultra-high energy atmospheric showers as the superposition of askaryan and geomagnetic mechanisms. Astroparticle Physics, 59:29–38, 2014.

[16] J. Alvarez-Muniz, E. Marqués, R. A. Vázquez, and E. Zas. Coherent radio pulses from showers in different media: A unified parametrization. Physical Review D—Particles, Fields, Gravitation, and Cosmology, 74(2):023007, 2006.

[17] L. A. Anchordoqui. Ultra-high-energy cosmic rays. Physics Reports, 801:1–93, 2019.

[18] L. A. Anchordoqui, V. Barger, J. G. Learned, D. Marfatia, and T. J. Weiler. Up-going anita events as evidence of the cpt symmetric universe. arXiv preprint arXiv:1803.11554, 2018.

[19] L. A. Anchordoqui, J. L. Feng, and H. Goldberg. Particle physics on ice: Constraints on neutrino interactions far above the weak scale. Physical review letters, 96(2):021101, 2006.

[20] A. M. Ankowski, A. Ashkenazi, S. Bacca, J. Barrow, M. Betancourt, A. Bodek, M. Christy, L. Doria, S. Dytman, A. Friedland, et al. Electron scattering and neu-

doi:10.6342/NTU202500216

trino physics. Journal of Physics G: Nuclear and Particle Physics, 50(12):120501, 2023.

[21] A. Arámburo-García, K. Bondarenko, A. Boyarsky, D. Nelson, A. Pillepich, and A. Sokolenko. Ultrahigh energy cosmic ray deflection by the intergalactic magnetic field. Physical Review D, 104(8):083017, 2021.

[22] G. Askaryan. Cerenkov radiation and transition radiation from electromagnetic waves. Sov. Phys. JETP, 15(5):943, 1962.

[23] M. S. Athar, A. Fatima, and S. Singh. Neutrinos and their interactions with matter. Progress in Particle and Nuclear Physics, 129:104019, 2023.

[24] W. Axford, E. Leer, and G. Skadron. The acceleration of cosmic rays by shock waves. In International cosmic ray conference, volume 11. Springer, 1977.

[25] S. Barwick, D. Besson, A. Burgman, E. Chiem, A. Hallgren, J. Hanson, S. Klein, S. Kleinfelder, A. Nelles, C. Persichilli, et al. Radio detection of air showers with the arianna experiment on the ross ice shelf. Astroparticle Physics, 90:50–68, 2017.

[26] R. A. Batista, R. M. De Almeida, B. Lago, and K. Kotera. Cosmogenic photon and neutrino fluxes in the auger era. Journal of Cosmology and Astroparticle Physics, 2019(01):002, 2019.

[27] J. F. Beacom, N. F. Bell, D. Hooper, S. Pakvasa, and T. J. Weiler. Measuring flavor ratios of high-energy astrophysical neutrinos. Physical Review D, 68(9):093005, 2003.

[28] J. Becker. High-energy neutrinos in the context of multimessenger physics, phys. rept., 458, 173. arXiv preprint arXiv:0710.1557, 2008.

doi:10.6342/NTU202500216

[29] A. Bell. Cosmic ray acceleration. Astroparticle Physics, 43:56–70, 2013.

[30] D. Biehl, D. Boncioli, C. Lunardini, and W. Winter. Tidally disrupted stars as a possible origin of both cosmic rays and neutrinos at the highest energies. Scientific reports, 8(1):10828, 2018.

[31] S. Bilenky. Neutrino in standard model and beyond. Physics of Particles and Nuclei, 46:475–496, 2015.

[32] M. Blennow, E. Fernandez-Martinez, J. Lopez-Pavon, and J. Menendez. Neutrinoless double beta decay in seesaw models. Journal of High Energy Physics, 2010(7):1–31, 2010.

[33] A. Burrows and J. M. Lattimer. Neutrinos from sn 1987a. Astrophysical Journal, Part 2-Letters to the Editor (ISSN 0004-637X), vol. 318, July 15, 1987, p. L63-L68., 318:L63–L68, 1987.

[34] P. Cao. A search for astrophysical ultra high energy neutrinos with the ANITA-IV experiment. PhD thesis, University of Delaware, 2018.

[35] A. Castellina. Astroparticle and particle physics at ultra-high energy: Results from the pierre auger observatory. SciPost Physics Proceedings, (13):034, 2023.

[36] S. Chatrchyan, V. Khachatryan, A. M. Sirunyan, A. Tumasyan, W. Adam, E. Aguilo, T. Bergauer, M. Dragicevic, J. Erö, C. Fabjan, et al. Observation of a new boson at a mass of 125 gev with the cms experiment at the lhc. Physics Letters B, 716(1):30–61, 2012.

[37] B. Chauhan and S. Mohanty. Leptoquark solution for both the flavor and anita anomalies. Physical Review D, 99(9):095018, 2019.

doi:10.6342/NTU202500216

[38] P. Chen, T. Tajima, and Y. Takahashi. Plasma wakefield acceleration for ultrahigh-energy cosmic rays. Physical Review Letters, 89(16):161101, 2002.

[39] Y. Chen. Simulation and design of new trigger system for the taroge project. Master's thesis, National Taiwan University, Jan 2017.

[40] Y. Chen, T. Collaboration, et al. Taroge experiment and reconstruction technique for near-horizon impulsive radio signals induced by ultra-high energy cosmic rays. In 37th International Cosmic Ray Conference, page 263, 2022.

[41] A. Coleman, J. Eser, E. Mayotte, F. Sarazin, F. G. Schröder, D. Soldin, T. Venters, R. Aloisio, J. Alvarez-Muñiz, R. A. Batista, et al. Ultra high energy cosmic rays the intersection of the cosmic and energy frontiers. Astroparticle physics, 149:102819, 2023.

[42] H. Collaboration and C. Adloff. Measurement of neutral and charged current cross sections in electron-proton collisions at high. The European Physical Journal C-Particles and Fields, 19(2):269–288, 2001.

[43] I. Collaboration, M. Aartsen, M. Ackermann, J. Adams, J. A. Aguilar, M. Ahlers, M. Ahrens, I. Al Samarai, D. Altmann, K. Andeen, et al. Neutrino emission from the direction of the blazar txs 0506+ 056 prior to the icecube-170922a alert. Science, 361(6398):147–151, 2018.

[44] I. Collaboration, MAGIC, AGILE, ASAS-SN, HAWC, HESS, INTEGRAL, Kanata, Kiso, Kapteyn, et al. Multimessenger observations of a flaring blazar coincident with high-energy neutrino icecube-170922a. Science, 361(6398):eaat1378, 2018.

doi:10.6342/NTU202500216

[45] P. A. Collaboration et al. The pierre auger cosmic ray observatory. Nuclear Instruments and Methods in Physics Research Section A: Accelerators, Spectrometers, Detectors and Associated Equipment, 798:172–213, 2015.

[46] T. A. Collaboration*†, R. Abbasi, M. Allen, R. Arimura, J. Belz, D. Bergman, S. Blake, B. Shin, I. Buckland, B. Cheon, et al. An extremely energetic cosmic ray observed by a surface detector array. Science, 382(6673):903–907, 2023.

[47] A. Condorelli, J. Biteau, and R. Adam. Impact of galaxy clusters on the propagation of ultrahigh-energy cosmic rays. The Astrophysical Journal, 957(2):80, 2023.

[48] P. Cristofari, P. Blasi, and D. Caprioli. Microphysics of diffusive shock acceleration: impact on the spectrum of accelerated particles. The Astrophysical Journal, 930(1):28, 2022.

[49] A. Crivellin and B. Mellado. Anomalies in particle physics and their implications for physics beyond the standard model. Nature Reviews Physics, 6(5):294–309, 2024.

[50] B. Dasgupta and J. Kopp. Sterile neutrinos. Physics Reports, 928:1–63, 2021.

[51] K. D. de Vries and S. Prohira. Coherent transition radiation from the geomagnetically induced current in cosmic-ray air showers: Implications for the anomalous events observed by anita. Physical review letters, 123(9):091102, 2019.

[52] G. Di Sciascio. Measurement of energy spectrum and elemental composition of pev cosmic rays: Open problems and prospects. Applied Sciences, 12(2):705, 2022.

[53] K. R. Dienes, E. Dudas, and T. Gherghetta. Light neutrinos without heavy mass

doi:10.6342/NTU202500216

scales: A higher-dimensional seesaw mechanism. Nuclear Physics B, 557(1-2):25–59, 1999.

[54] S. Dodelson and L. M. Widrow. Sterile neutrinos as dark matter. Physical Review Letters, 72(1):17, 1994.

[55] M. Drewes. The phenomenology of right handed neutrinos. International Journal of Modern Physics E, 22(08):1330019, 2013.

[56] R. Engel, D. Heck, and T. Pierog. Extensive air showers and hadronic interactions at high energy. Annual review of nuclear and particle science, 61(1):467–489, 2011.

[57] I. Esteban, S. Pandey, V. Brdar, and J. F. Beacom. Probing secret interactions of astrophysical neutrinos in the high-statistics era. Physical Review D, 104(12):123014, 2021.

[58] K. Fang. Ultra-high-energy cosmic rays: Scientific motivation. Large Area Networked Detectors for Particle Astrophysics, pages 1–31, 2023.

[59] G. R. Farrar and A. Gruzinov. Giant agn flares and cosmic ray bursts. The Astrophysical Journal, 693(1):329, 2009.

[60] D. F. Fiorillo. High-energy and ultra-high-energy neutrino astrophysics. Universe, 10(3):149, 2024.

[61] G. L. Fogli, E. Lisi, and D. Montanino. Comprehensive analysis of solar, atmospheric, accelerator, and reactor neutrino experiments in a hierarchical three-generation scheme. Physical Review D, 49(7):3626, 1994.

[62] J. A. Formaggio and G. P. Zeller. From ev to eev: Neutrino cross sections across energy scales. Reviews of Modern Physics, 84(3):1307–1341, 2012.

doi:10.6342/NTU202500216

[63] D. B. Fox, S. Sigurdsson, S. Shandera, P. Mészáros, K. Murase, M. Mostafá, and S. Coutu. The anita anomalous events as signatures of a beyond standard model particle, and supporting observations from icecube. arXiv preprint arXiv:1809.09615, 2018.

[64] T. K. Gaisser, R. Engel, and E. Resconi. Cosmic rays and particle physics. Cambridge University Press, 2016.

[65] R. Gandhi, C. Quigg, M. H. Reno, and I. Sarcevic. Neutrino interactions at ultrahigh energies. Physical Review D, 58(9):093009, 1998.

[66] D. Góra. Particle physics in cosmic rays. International Journal of Modern Physics A, 36(34n35):2141010, 2021.

[67] D. Gora and P. A. Collaboration. The pierre auger observatory: review of latest results and perspectives. Universe, 4(11):128, 2018.

[68] P. Gorham, A. Ludwig, C. Deaconu, P. Cao, P. Allison, O. Banerjee, L. Batten, D. Bhattacharya, J. Beatty, K. Belov, et al. Unusual near-horizon cosmic-ray-like events observed by anita-iv. Physical review letters, 126(7):071103, 2021.

[69] P. Gorham, J. Nam, A. Romero-Wolf, S. Hoover, P. Allison, O. Banerjee, J. Beatty, K. Belov, D. Z. Besson, W. Binns, et al. Characteristics of four upward-pointing cosmic-ray-like events observed with anita. Physical Review Letters, 117(7):071101, 2016.

[70] P. Gorham, B. Rotter, P. Allison, O. Banerjee, L. Batten, J. Beatty, K. Bechtol, K. Belov, D. Besson, W. Binns, et al. Observation of an unusual upward-going cosmic-ray-like event in the third flight of anita. Physical review letters, 121(16):161102, 2018.

doi:10.6342/NTU202500216

[71] P. E. Greenwood and M. S. Nikulin. A guide to chi-squared testing, volume 280. John Wiley & Sons, 1996.

[72] K. Greisen. End to the cosmic-ray spectrum? Physical Review Letters, 16(17):748, 1966.

[73] D. Griffiths. Introduction to elementary particles. John Wiley & Sons, 2020.

[74] W. F. Hanlon. Cosmic ray spectrum.

[75] D. Heck, J. Knapp, J. Capdevielle, G. Schatz, T. Thouw, et al. Corsika: A monte carlo code to simulate extensive air showers. 1998.

[76] E. Helder, J. Vink, A. Bykov, Y. Ohira, J. Raymond, and R. Terrier. Observational signatures of particle acceleration in supernova remnants. Space Science Reviews, 173:369–431, 2012.

[77] L. Heurtier, Y. Mambrini, and M. Pierre. Dark matter interpretation of the anita anomalous events. Physical Review D, 99(9):095014, 2019.

[78] P. W. Higgs. Broken symmetries and the masses of gauge bosons. Physical review letters, 13(16):508, 1964.

[79] A. M. Hillas. The origin of ultra-high-energy cosmic rays. IN: Annual review of astronomy and astrophysics. Volume 22. Palo Alto, CA, Annual Reviews, Inc., 1984, p. 425-444., 22:425–444, 1984.

[80] G.-y. Huang. Sterile neutrinos as a possible explanation for the upward air shower events at anita. Physical Review D, 98(4):043019, 2018.

[81] T. Huege. Radio detection of cosmic rays with the auger engineering radio array. In EPJ Web of Conferences, volume 210, page 05011. EDP Sciences, 2019.

doi:10.6342/NTU202500216

[82] T. Huege and D. Besson. Radio-wave detection of ultra-high-energy neutrinos and cosmic rays. Progress of Theoretical and Experimental Physics, 2017(12):12A106, 2017.

[83] T. Huege, M. Ludwig, and C. W. James. Simulating radio emission from air showers with coreas. In AIP Conference Proceedings, volume 1535, pages 128–132. American Institute of Physics, 2013.

[84] A. Ismail, R. Mammen Abraham, and F. Kling. Neutral current neutrino interactions at faser ν. Physical Review D, 103(5):056014, 2021.

[85] J. V. Jelley. Cerenkov radiation and its applications. British Journal of Applied Physics, 6(7):227, 1955.

[86] B. Kayser. Neutrino mass, mixing, and oscillation. In Flavor Physics For The Millennium: TASI 2000, pages 625–650. World Scientific, 2001.

[87] M. Koshiba. Observational neutrino astrophysics. Physics Reports, 220(5-6):229–381, 1992.

[88] K. Kotera and A. V. Olinto. The astrophysics of ultrahigh-energy cosmic rays. Annual Review of Astronomy and Astrophysics, 49(1):119–153, 2011.

[89] A. Letessier-Selvon and T. Stanev. Ultrahigh energy cosmic rays. Reviews of modern physics, 83(3):907–942, 2011.

[90] A. Lichtenberg, M. Lieberman, and R. Cohen. Fermi acceleration revisited. Physica D: Nonlinear Phenomena, 1(3):291–305, 1980.

[91] M. Livan and R. Wigmans. Calorimetry for collider physics, an introduction. Springer, 2019.

doi:10.6342/NTU202500216

[92] M. S. Longair. High energy astrophysics. Cambridge university press, 2011.

[93] A. I. Lvovsky. Fresnel equations. Encyclopedia of Optical Engineering, 27:1–6, 2013.

[94] J. Madsen. Ultra-high energy neutrinos. arXiv preprint arXiv:1901.02528, 2019.

[95] D. Marfatia, D. McKay, and T. Weiler. New physics with ultra-high-energy neutrinos. Physics Letters B, 748:113–116, 2015.

[96] G. C. McLaughlin and R. Surman. Supernova neutrinos: The accretion disk scenario. Physical Review D—Particles, Fields, Gravitation, and Cosmology, 75(2):023005, 2007.

[97] R. N. Mohapatra and A. Y. Smirnov. Neutrino mass and new physics. Annu. Rev. Nucl. Part. Sci., 56(1):569–628, 2006.

[98] S. Mollerach and E. Roulet. Progress in high-energy cosmic ray physics. Progress in Particle and Nuclear Physics, 98:85–118, 2018.

[99] D. Morgan. Surface acoustic wave filters: With applications to electronic communications and signal processing. Academic Press, 2010.

[100] M. Nagano and A. A. Watson. Observations and implications of the ultrahigh-energy cosmic rays. Reviews of Modern Physics, 72(3):689, 2000.

[101] J. Nam, C.-C. Chen, C.-H. Chen, C.-W. Chen, P. Chen, Y.-C. Chen, S.-Y. Hsu, J.-J. Huang, M.-H. Huang, T.-C. Liu, et al. Design and implementation of the taroge experiment. International Journal of Modern Physics D, 25(13):1645013, 2016.

doi:10.6342/NTU202500216

[102] J. Nam, C. Kuo, B. Shin, P. Chen, Y. Chen, S. Hsu, J. Huang, and M. HA. Drone-borne calibration pulser for radio observatories detecting ultra-high-energy cosmic rays and neutrinos. 2023.

[103] R. Nichol, A. Collaboration, et al. Radio detection of high-energy particles with the anita experiment. Nuclear Instruments and Methods in Physics Research Section A: Accelerators, Spectrometers, Detectors and Associated Equipment, 626:S30–S35, 2011.

[104] M. H. Olsen. Pcb design tutorial with eagle. Orsted-DTU, Automation, Technical University of Denmark, pages 1–15, 2004.

[105] W. Pauli. On the earlier and more recent history of the neutrino. In Neutrino physics. 1991.

[106] K. V. Ptitsyna and S. V. Troitsky. Physical conditions in potential accelerators of ultra-high-energy cosmic rays: updated hillas plot and radiation-loss constraints. Physics-Uspekhi, 53(7):691, 2010.

[107] A. Raghav and Z. Shaikh. Cosmic ray acceleration via magnetic reconnection of magnetic islands/flux-ropes. arXiv preprint arXiv:1610.09628, 2016.

[108] M. V. Rao and B. V. Sreekantan. Extensive air showers. World scientific, 1998.

[109] F. Reines and C. L. COWANjun. The neutrino. Nature, 178(4531):446–449, 1956.

[110] M. H. Reno. High-energy to ultrahigh-energy neutrino interactions. Annual Review of Nuclear and Particle Science, 73(1):181–204, 2023.

[111] L. F. Roberts, J. Lippuner, M. D. Duez, J. A. Faber, F. Foucart, J. C. Lombardi, S. Ning, C. D. Ott, and M. Ponce. The influence of neutrinos on r-process nucle-

doi:10.6342/NTU202500216

osynthesis in the ejecta of black hole–neutron star mergers. Monthly Notices of the Royal Astronomical Society, 464(4):3907–3919, 2016.

[112] E. Roulet and F. Vissani. Neutrinos in Physics and Astrophysics. World Scientific, 2022.

[113] H. Schoorlemmer, K. Belov, A. Romero-Wolf, D. García-Fernández, V. Bugaev, S. Wissel, P. Allison, J. Alvarez-Muñiz, S. Barwick, J. Beatty, et al. Energy and flux measurements of ultra-high energy cosmic rays observed during the first anita flight. Astroparticle Physics, 77:32–43, 2016.

[114] F. G. Schröder. Radio detection of cosmic-ray air showers and high-energy neutrinos. Progress in Particle and Nuclear Physics, 93:1–68, 2017.

[115] L. Schumacher. Search for correlations of high-energy neutrinos and ultrahigh-energy cosmic rays. In EPJ Web of Conferences, volume 207, page 02010. EDP Sciences, 2019.

[116] I. M. Shoemaker, A. Kusenko, P. K. Munneke, A. Romero-Wolf, D. M. Schroeder, and M. J. Siegert. Reflections on the anomalous anita events: the antarctic subsurface as a possible explanation. Annals of Glaciology, 61(81):92–98, 2020.

[117] D. Smith, D. Besson, C. Deaconu, S. Prohira, P. Allison, L. Batten, J. Beatty, W. Binns, V. Bugaev, P. Cao, et al. Experimental tests of sub-surface reflectors as an explanation for the anita anomalous events. Journal of Cosmology and Astroparticle Physics, 2021(04):016, 2021.

[118] S. Sotirov. General constraints on sources of high-energy cosmic rays from interaction losses. Physical Review D, 107(12):123018, 2023.

doi:10.6342/NTU202500216

[119] D. Southall, C. Deaconu, V. Decoene, E. Oberla, A. Zeolla, J. Alvarez-Muñiz, A. Cummings, Z. Curtis-Ginsberg, A. Hendrick, K. Hughes, et al. Design and initial performance of the prototype for the beacon instrument for detection of ultrahigh energy particles. Nuclear Instruments and Methods in Physics Research Section A: Accelerators, Spectrometers, Detectors and Associated Equipment, 1048:167889, 2023.

[120] M. Spurio, Spurio, and Bellantone. Probes of Multimessenger Astrophysics. Springer, 2018.

[121] B. Strutt. A Search for Ultra-High Energy Neutrinos and Cosmic Rays with ANITA-3. PhD thesis, UCL (University College London), 2017.

[122] A. D. Supanitsky. Determination of the cosmic-ray chemical composition: Open issues and prospects. Galaxies, 10(3):75, 2022.

[123] Ø. A. Tengesdal. Measurement of seawater refractive index and salinity by means of optical refraction. Master's thesis, The University of Bergen, 2012.

[124] D. Thomas and P. Moorby. The Verilog® hardware description language. Springer Science & Business Media, 2008.

[125] M. Thomson. Modern particle physics. Cambridge University Press, 2013.

[126] V. B. Valera, M. Bustamante, and C. Glaser. The ultra-high-energy neutrino-nucleon cross section: measurement forecasts for an era of cosmic eev-neutrino discovery. Journal of High Energy Physics, 2022(6):1–72, 2022.

[127] V. B. Valera, M. Bustamante, and C. Glaser. Comprehensive measurement forecasts

doi:10.6342/NTU202500216

of the eev neutrino-nucleon cross section with cosmic neutrinos at icecube-gen2. arXiv e-prints, pages arXiv–2307, 2023.

[128] V. B. Valera, M. Bustamante, and C. Glaser. Near-future discovery of the diffuse flux of ultrahigh-energy cosmic neutrinos. Physical Review D, 107(4):043019, 2023.

[129] M. P. van Haarlem, M. W. Wise, A. Gunst, G. Heald, J. P. McKean, J. W. Hessels, A. G. de Bruyn, R. Nijboer, J. Swinbank, R. Fallows, et al. Lofar: The low-frequency array. Astronomy & astrophysics, 556:A2, 2013.

[130] V. Verzi, P. A. Collaboration, et al. Measurement of the energy spectrum of ultra-high energy cosmic rays using the pierre auger observatory. In 36th International Cosmic Ray Conference, volume 358, page 450. SISSA Medialab, 2021.

[131] A. Vieregg, Q. Abarr, P. Allison, J. Ammerman Yebra, J. Alvarez-Muñiz, J. Beatty, D. Besson, P. Chen, Y. Chen, X. Cheng, et al. Discovering the highest energy neutrinos with the payload for ultrahigh energy observations (pueo). In Proceedings of Science, volume 395. Proceedings of Science, 2022.

[132] E. Vitagliano, I. Tamborra, and G. Raffelt. Grand unified neutrino spectrum at earth: Sources and spectral components. Reviews of Modern Physics, 92(4):045006, 2020.

[133] J. Wang. Unified model beyond grand unification. Physical Review D, 103(10):105024, 2021.

[134] S.-H. Wang. Radio Detection of Ultra-high Energy Cosmic Rays and Earth-skimming Tau Neutrinos with TAROGE Antenna Arrays on High Mountains. PhD thesis, National Taiwan University, Jan 2023.

doi:10.6342/NTU202500216

[135] S.-H. Wang, J. Nam, P. Chen, Y. Chen, T. Choi, Y.-b. Ham, S.-Y. Hsu, J.-J. Huang, M.-H. A. Huang, G. Jee, et al. Taroge-m: radio antenna array on antarctic high mountain for detecting near-horizontal ultra-high energy air showers. Journal of Cosmology and Astroparticle Physics, 2022(11):022, 2022.

[136] A. Watson. Extensive air showers and ultra high energy cosmic rays. Lectures given at a Summer School in Mexico, 87, 2002.

[137] E. Waxman. Cosmological gamma-ray bursts and the highest energy cosmic rays. Physical Review Letters, 75(3):386, 1995.

[138] T. Wibig and A. W. Wolfendale. Universal cosmic rays energy spectrum and the mass composition at the'ankle'and above. arXiv preprint arXiv:1706.05872, 2017.

[139] W. Winter. Sources of high-energy astrophysical neutrinos. arXiv preprint arXiv:2402.19314, 2024.

[140] S. Wissel, A. Romero-Wolf, H. Schoorlemmer, W. R. Carvalho Jr, J. Alvarez-Muñiz, E. Zas, A. Cummings, C. Deaconu, K. Hughes, A. Ludwig, et al. Prospects for high-elevation radio detection of> 100 pev tau neutrinos. Journal of Cosmology and Astroparticle Physics, 2020(11):065, 2020.

doi:10.6342/NTU202500216

doi:10.6342/NTU202500216

Appendix A — Waveforms of CR candidates

Here shows the waveforms of 52 CR candidates, excluding one ocean-reflected event and four double-pulse events discussed in Chapter 7.

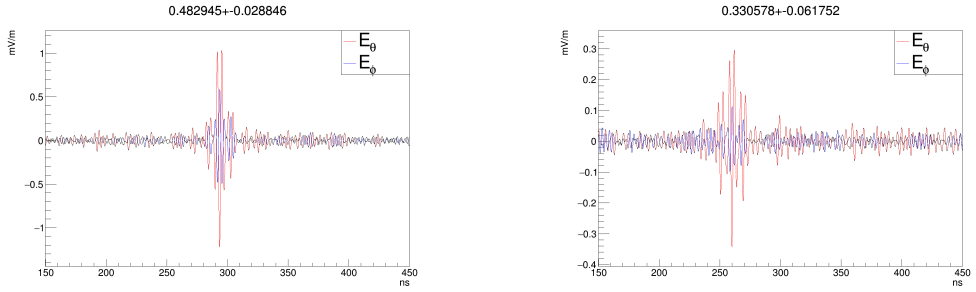

Figure A.1: Waveforms of 52 CR candidates, excluding one ocean-reflected event and four double-pulse events.

doi:10.6342/NTU202500216

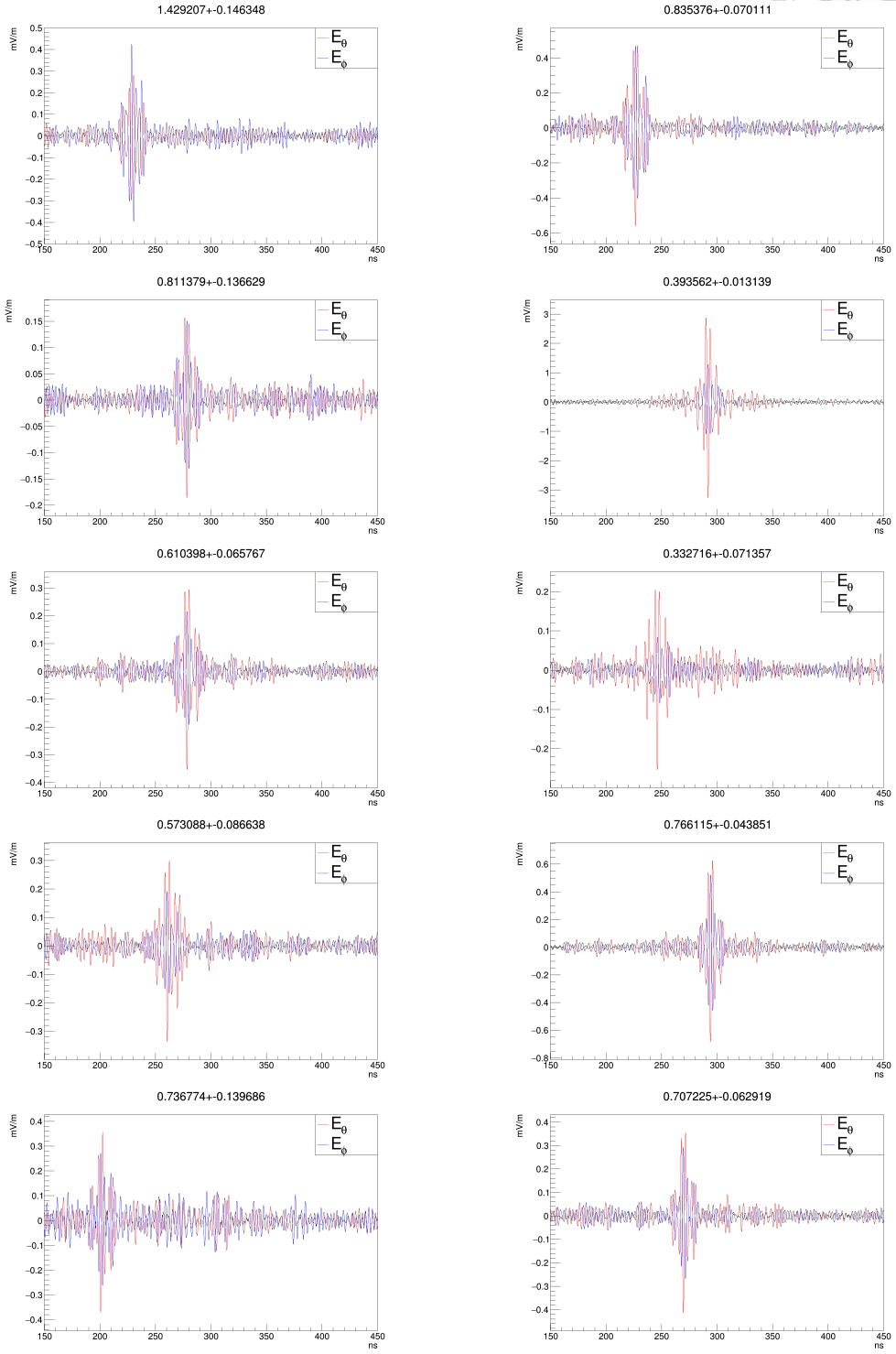

Figure A.2: Waveforms of 52 CR candidates (continue), excluding one ocean-reflected event and four double-pulse events.

doi:10.6342/NTU202500216

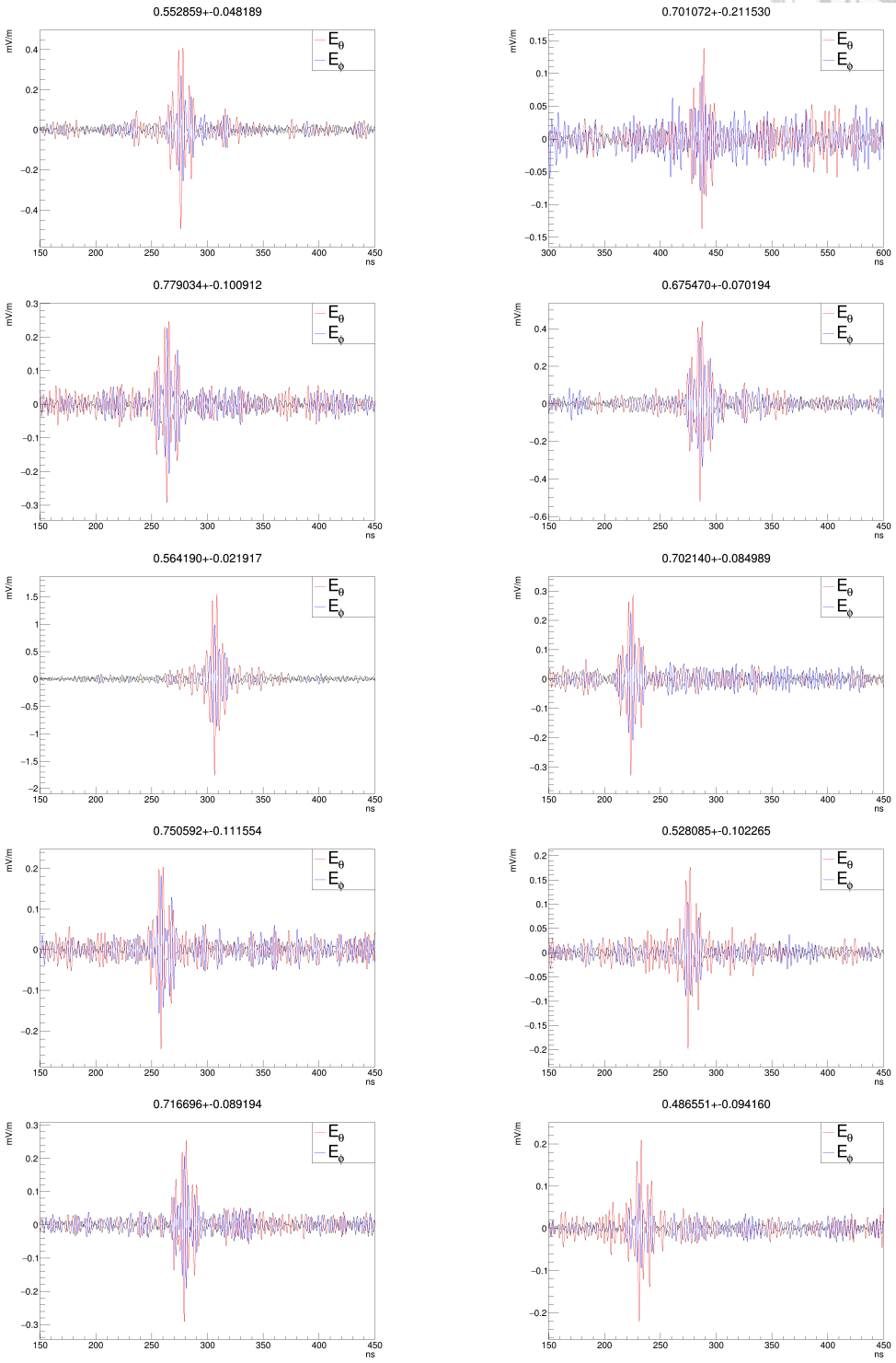

Figure A.3: Waveforms of 52 CR candidates (continue), excluding one ocean-reflected event and four double-pulse events.

doi:10.6342/NTU202500216

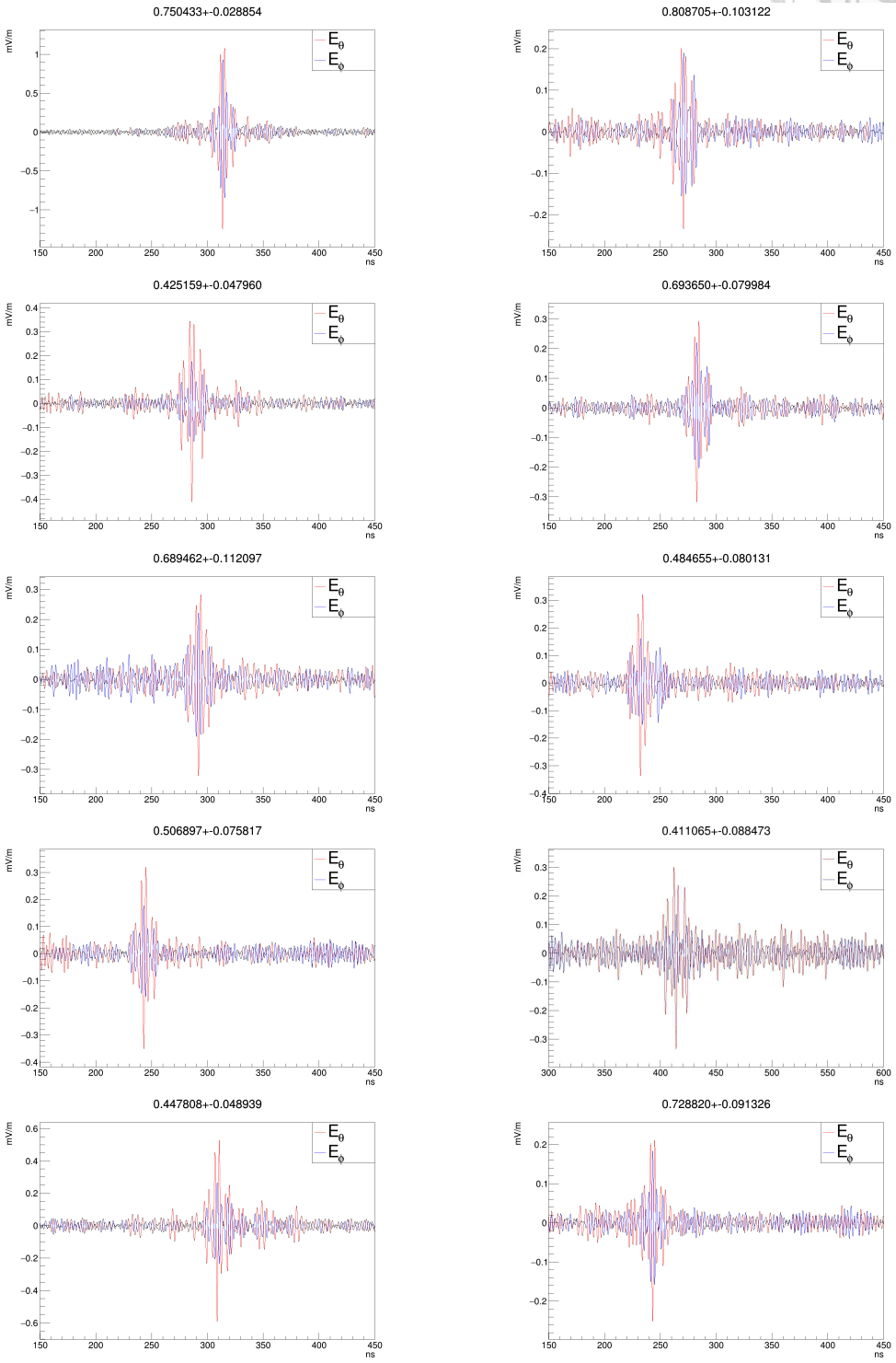

Figure A.4: Waveforms of 52 CR candidates (continue), excluding one ocean-reflected event and four double-pulse events.

doi:10.6342/NTU202500216

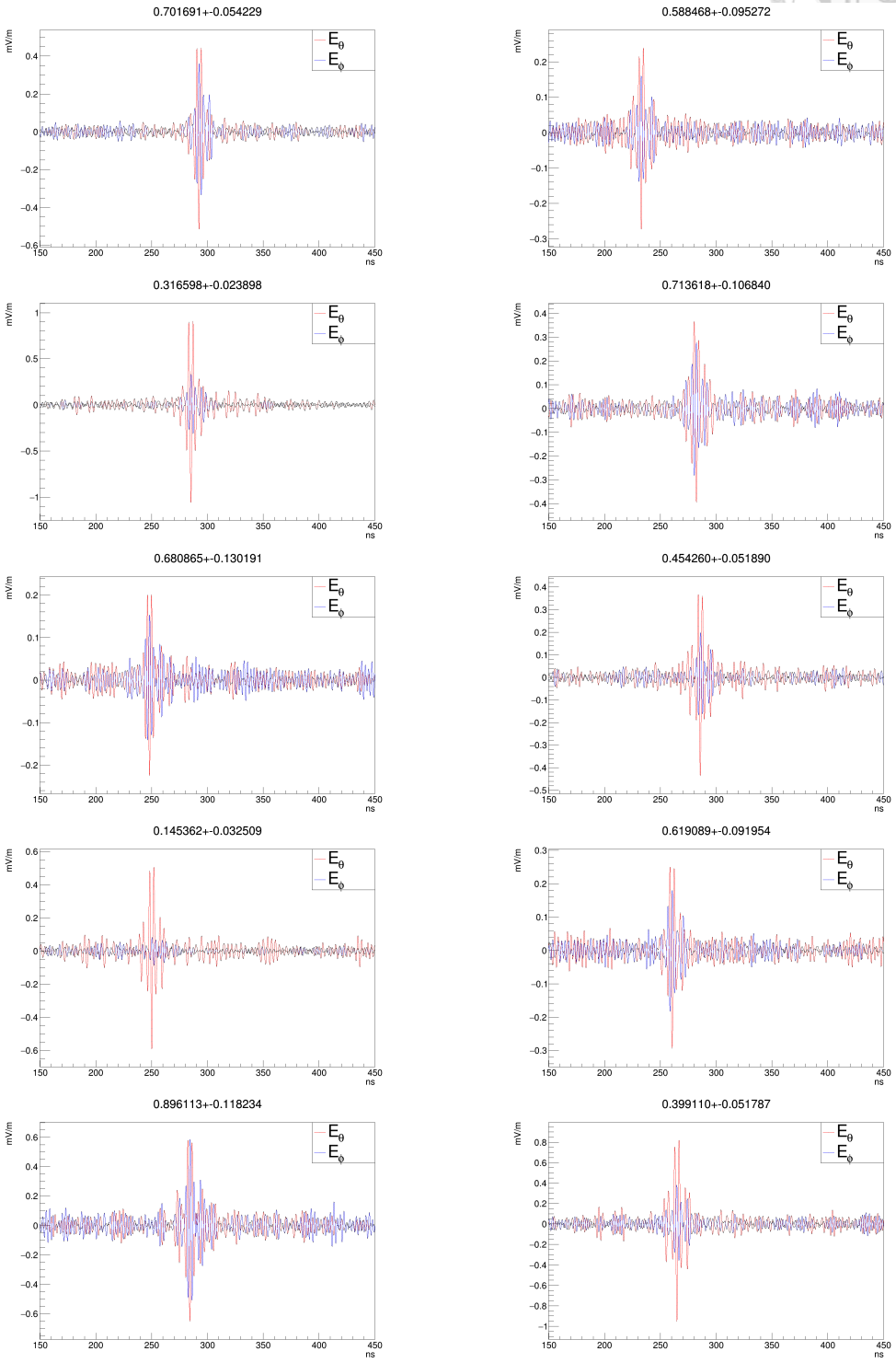

Figure A.5: Waveforms of 52 CR candidates (continue), excluding one ocean-reflected event and four double-pulse events.

doi:10.6342/NTU202500216

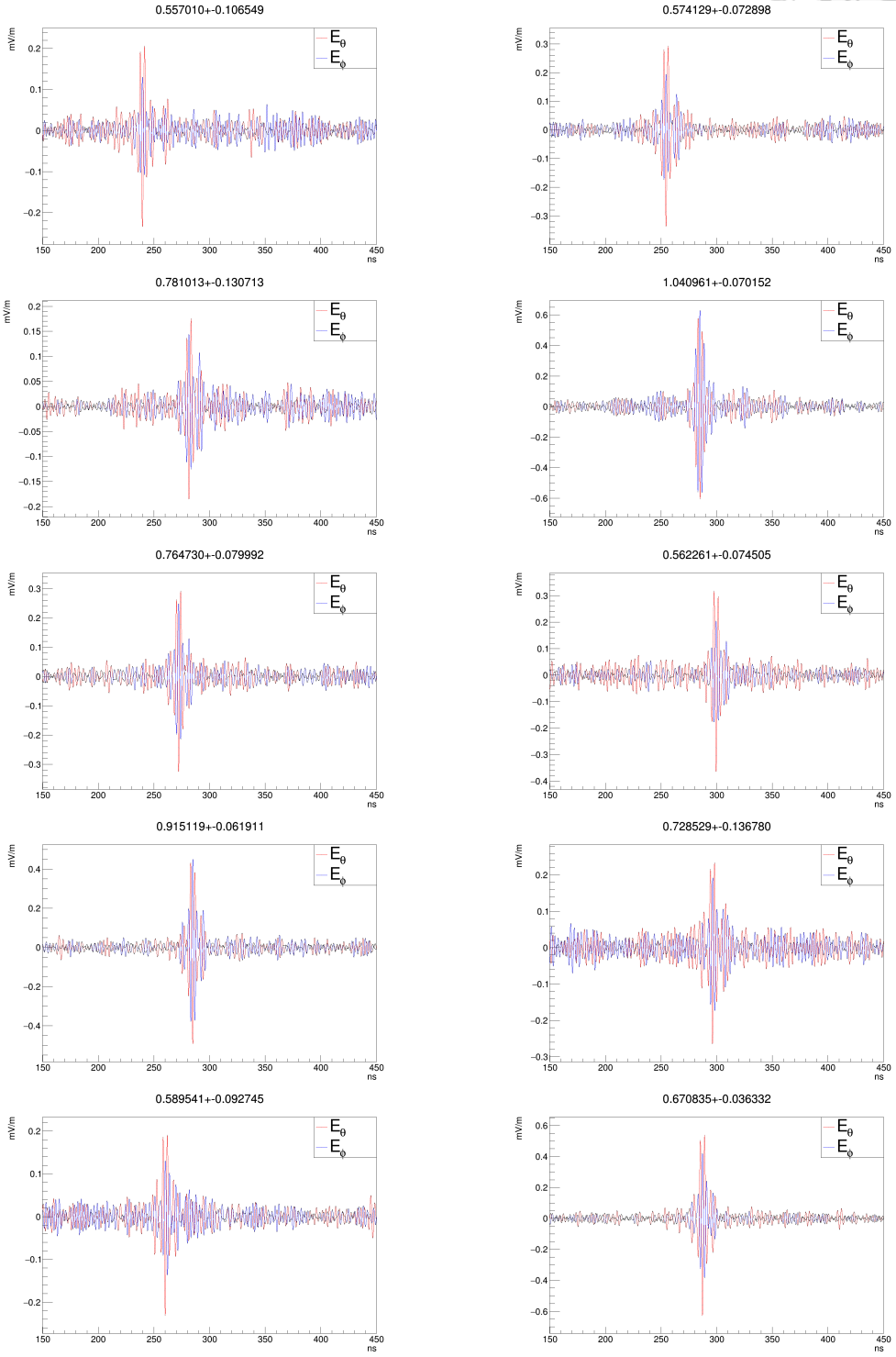

Figure A.6: Waveforms of 52 CR candidates (continue), excluding one ocean-reflected event and four double-pulse events.

doi:10.6342/NTU202500216